DESIGN AND ANALYSIS OF COMPACT CPW-FED MULTIBAND ANTENNAS INCORPORATING UWB APPLICATIONS

A THESIS

submitted by

SAIRA JOSEPH

for the award of the degree

of

DOCTOR OF PHILOSOPHY

COCHIN UNIVERSITY OF
SCIENCE AND TECHNOLOGY

DIVISION OF ELECTRONICS ENGINEERING

SCHOOL OF ENGINEERING

COCHIN UNIVERSITY OF SCIENCE AND TECHNOLOGY, KOCHI

NOVEMBER 2016

THESIS CERTIFICATE

This is to certify that the thesis entitled **DESIGN AND ANALYSIS OF COMPACT CPW-FED MULTIBAND ANTENNAS INCORPORATING UWB APPLICATIONS** submitted by Saira Joseph to the Cochin University of Science and Technology, Kochi for the award of the degree of Doctor of Philosophy is a bonafide record of research work carried out by her under my supervision and guidance at the Division of Electronics Engineering, School of Engineering, Cochin University of Science and Technology. The contents of this thesis, in full or in part, have not been submitted to any other University or Institute for the award of any other degree.

I further declare that the modifications suggested by the audience during the pre-synopsis of Saira Joseph   have been incorporated in the thesis.

Kochi-682 022
Date:
                                                                    Dr. Binu Paul
                                                                    (Research Advisor)
                                                                    Associate Professor
                                                                    Division of Electronics Engineering
                                                                    School of Engineering
                                                                    Cochin University of Science and Technology

DECLARATION

I hereby declare that the work presented in the thesis entitled **DESIGN AND ANALYSIS OF COMPACT CPW-FED MULTIBAND ANTENNAS INCORPORATING UWB APPLICATIONS** is based on the original research work carried out by me under the supervision and guidance of Dr. Binu Paul, Associate Professor, for the award of the degree of Doctor of Philosophy with Cochin University of Science and Technology. I further declare that the contents of this thesis in full or in parts have not been submitted to any other University or Institute for the award of any degree or diploma.

Kochi- 682 022   Saira Joseph
Date: Division of Electronics Engineering

ACKNOWLEDGEMENT

ABSTRACT

KEYWORDS: Multiband antenna; UWB antenna; Fractal; Slotted monopole; Spiral monopole.

Over the past decade, there is a great demand for permission to transmit large bandwidth concurrent with existing narrowband signals. In 2002, the federal communications commission (FCC) decided to permit use of ultrawideband (UWB) systems. UWB systems are unique in their large instantaneous bandwidth and potential for low-cost digital design that enables a single system to operate in different modes as a communication device, radar etc. UWB systems aim at covering the frequency band of 3.1-10.6 GHz defined by the FCC. The addition of more and more features in each new generation communication system demands universal antennas suitable for operation in multiple bands. In this regard, designing a multiband antenna which also covers the UWB range without deteriorating the UWB performance is of great interest. Also, a significant issue in communication systems is to miniaturize the antenna size while providing good performance over the operation bands.

The thesis presents three different designs of CPW-fed multiband antennas. The first design uses a fractal concept to achieve multiband operation. In the second and third designs, a slotted circular monopole and a spiral monopole are used respectively for multiband operation with UWB applications. For both these cases, variations from the basic antenna geometry are also proposed in which the frequency of operation is lowered without increase in overall antenna size. Design guidelines are developed for all antennas to facilitate design on substrates of different permittivity and thickness. The antennas are analyzed in both frequency and time domain for complete characterization.

TABLE OF CONTENTS

CHAPTER 3   CPW-FED FRACTAL MULTIBAND ANTENNA

CHAPTER 4   CPW-FED SLOTTED MULTIBAND ANTENNAS

CHAPTER 5   CPW-FED SPIRAL MULTIBAND ANTENNAS

CHAPTER 6   CONCLUSION AND FUTURE WORK

APPENDIX-A   COMPACT CPW-FED UWB ANTENNA WITH DUAL NOTCH BANDS

APPENDIX-B FREQUENCY AND TIME DOMAIN CHARACTERIZATION OF CPW-FED DUAL-BAND SPIRAL ANTENNA WITH UWB APPLICATION

REFERENCES

LIST OF PUBLICATIONS

CURRICULUM VITAE

LIST OF TABLES

LIST OF FIGURES

xiv

xvii

ABBREVIATIONS

ACS	Asymmetric Coplanar Strip
AUT	Antenna Under Test
AWGN	Additive White Gaussian Noise
CLL	Capacitive Loaded Loop
CMOS	Complementary Metal Oxide Semiconductor
CPS	Coplanar Strip
CPW	Coplanar Waveguide
CREMA	Centre for Research in Electromagnetics and Antennas
CSRR	Complementary Split Ring Resonator
CSV	Comma Separated Variable
CW	Continuous Wave
DCS	Digital Cellular System
EIRP	Effective Isotropically Radiated Power
FCC	Federal Communications Commission
FEM	Finite Element Method
FF	Fidelity Factor
FR4	Fire Resistant Grade 4
FWHM	Full Width Half Maxima
GPS	Global Positioning System
GSM	Global System for Mobile
GUI	Graphical User Interface
HFSS	High Frequency Structure Simulator
IFFT	Inverse Fast Fourier Transform
IMT	International Mobile Telecommunications
LTI	Linear Time Invariant
MB-OFDM	Multi Band Orthogonal Frequency Division Multiplexing
MIMO	Multiple Input Multiple Output
MMIC	Monolithic Microwave Integrated Circuit
PC	Personal Computer

PCB	Printed Circuit Board
PCS	Personal Communications Service
PEC	Perfect Electric Conductor
PIFA	Planar Inverted-F Antenna
PNA	Programmable Network Analyzer
PSD	Power Spectral Density
PTMA	Planar Triangular Monopole Antenna
RF	Radio Frequency
SAR	Specific Absorption Rate
SMA	Sub Miniature version A
SNR	Signal to Noise Ratio
TEM	Transverse Electromagnetic
THSS	Time Hopping Spread Spectrum
UHF	Ultra High Frequency
UWB	Ultrawideband
UMTS	Universal Mobile Telecommunication System
UV	Ultra Violet
VSWR	Voltage Standing Wave Ratio
WCDMA	Wireless Code Division Multiple Access
Wi-Fi	Wireless Fidelity
WiMAX	Worldwide Interoperability for Microwave Access
WLAN	Wireless Local Area Network
WMTS	Wireless Medical Telemetry Service
WPAN	Wireless Personal Area Network

NOTATIONS

English Symbols

$A(\omega)$	Magnitude response
B	Channel bandwidth
c	Free space velocity of electromagnetic waves
C	Channel capacity
f_1	First resonant frequency
f_2	Second resonant frequency
f_L	Lower frequency limit of UWB band
F	Fractal scaling factor
G	Absolute gain
G_{ref}	Gain of standard horn antenna
h	Thickness of substrate
$H(\omega)$	Transfer function
L	Length of spectrum
P_{osd}	Radiated power spectral density
P_t	Transmitted power
P_r	Received power
R	Distance between transmitter and receiver stations
r	Far field distance
S/N or SNR	Signal to noise ratio
S_{11}/ S_{22}	Reflection coefficient scattering parameter
S_{12}/ S_{21}	Transmission coefficient scattering parameter
$S_{11\text{-}FS}$	Reflection coefficient of antenna in free space
$S_{11\text{-}WC}$	Reflection coefficient of antenna with closed metallic chamber
$s_o(f)$	Spectrum of output pulse
$s_i(t)$	Input pulse to antenna
$s_o(t)$	Output pulse from antenna
W_f	Width of CPW feed line
Z_c	Characteristic impedance of antenna
Z_o	Free space characteristic impedance

xxiii

Greek Symbols

ϵ_r	Relative permittivity or dielectric constant of substrate
ϵ_{reff}	Effective permittivity of substrate
η	Antenna efficiency
Γ	Reflection coefficient
λ	Free space wavelength
λ_c	Guide wavelength corresponding to center frequency of the UWB band
λ_g	Guide wavelength
λ_{g1}	Guide wavelength at first resonance
λ_{g2}	Guide wavelength at second resonance
λ_n	Guide wavelength at notched frequency
Φ	Azimuth angle
σ	Pulse parameter
$\tan \delta$	Loss tangent of substrate
θ	Elevation angle
$\theta(\omega)$	Phase response
τ	Group delay

Chapter 1

INTRODUCTION

The desire for mobility and communication is deeply ingrained in human nature and in any wireless communication system the antenna is a critical component. An antenna is used to either transmit or receive electromagnetic waves. It serves as a transducer for converting guided waves into free-space waves in the transmitting mode or vice versa in the receiving mode. All antennas operate on the same basic principles of electromagnetic theory formulated by James Clerk Maxwell. With the advent of the information era, numerous advanced communication technologies have arisen during the past two decades which have greatly influenced and benefited every field of our society. The addition of more and more features in each new generation communication system demands universal antennas suitable for operation in multiple bands. In addition to multiband operation, it is necessary that the antenna is small, light weight, low profile and can be easily integrated with other microwave components. In order to accomplish this, the antenna can be fabricated onto a printed circuit board (PCB) and embedded into the casing of devices.

1.1 MULTIBAND AND BROADBAND ANTENNAS

In many applications such as global system for mobile (GSM) 900/1800 and wireless local area network (WLAN) 2.4/5.2GHz, operation in two or more discrete bands with an arbitrary separation between the bands is desired. Dual-band antennas are good candidates for these applications as two separate modes can be excited with two different current paths. Several designs using uni-planar structures with slots or

additional strips have been reported in which the various dimensions of the slots or strips create the individual bands. Dual-band antennas can also be implemented by combining a monopole antenna and a slot antenna to generate respective frequency bands. To meet the growing requirements of modern communication systems triple-band antennas have overtaken dual-band antennas gradually. Double-layered triple-band antenna designs using the above mentioned methods (e.g., employing multi-strip radiators or slots to increase operation bands) have been proposed, however the fabrication process is complicated. Furthermore, multiple slots can be used for developing quad-band antennas.

While multiband antennas can offer integration of multiple services, it would be extremely difficult to accurately achieve the frequency requirements of all future communication systems. Alternately, a single antenna that covers a wide range of frequencies with same polarization would be an ideal candidate not only for present multi-band applications but also for future communication systems. This has led to the development of broadband antennas which usually require structures that do not emphasize abrupt changes in the physical dimensions involved but instead have smooth boundaries. Such a physical structure tends to produce patterns and input impedances that changes smoothly with frequencies.

1.2 ULTRAWIDEBAND (UWB) TECHNOLOGY

In the past few years, wireless personal area network (WPAN) have been attracting considerable interest and is undergoing rapid development worldwide. A WPAN is a network for interconnecting devices around an individual person's workspace in which

the connections are wireless. The maximum available data rate, or capacity, for the ideal band-limited additive white Gaussian noise (AWGN) channel is given by Shannon's theorem

$$C = B \times log_2\left(1 + \frac{S}{N}\right) \tag{1.1}$$

Where C is the channel capacity, B is the bandwidth and S/N is the signal to noise ratio (SNR). Equation (1.1) illustrates that the transmission data rate can be raised by enlarging the bandwidth or amplifying the transmission power. Nevertheless, the signal power cannot be easily increased as many portable devices are powered by battery and the potential interference with other radio systems should also be suppressed. Therefore, a huge frequency bandwidth will be the solution to realize a high data rate.

Range of operation of such systems are determined by the Friis formula,

$$R \propto \sqrt{\frac{P_t}{P_r}} \tag{1.2}$$

where R is the distance between transmitter and receiver, P_t the transmitter power and P_r the receiver power. Equations (1.1) and (1.2) together suggest that it is more efficient to achieve higher capacity by increasing bandwidth instead of power, while it is equally difficult to achieve a longer range.

UWB technology has received considerable attention ever since the federal communications commission (FCC) authorized the unlicensed use of the frequency spectrum ranging from 3.1 GHz to 10.6 GHz in 2002 (FCC, 2012). This technology

3

opens new doors for wireless communication systems in commercial and military domains.

In a UWB system, the spectrum occupies more than 20 % of the center frequency or a minimum of 500 MHz. Most narrowband systems occupy less than 10 % of the center frequency bandwidth, and are transmitted at far greater power levels. The FCC restricts the power for UWB systems to –41.3 dBm/MHz (75 nanowatts/ MHz), (Porcino, 2003) which puts them in the category of unintentional radiators, such as TVs and computer monitors. Such power restriction allows UWB systems to reside below the noise floor of a typical narrowband receiver and enables UWB signals to coexist with current radio services with minimal or no interference as illustrated in Fig. 1.1.
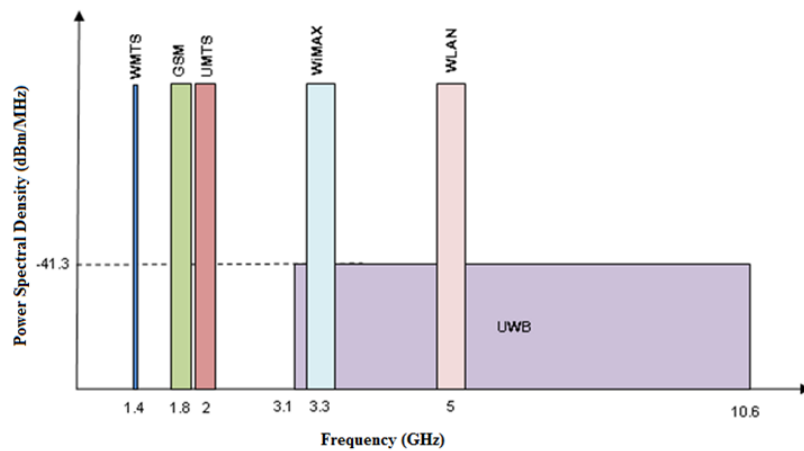
Fig. 1.1   Coexistence of UWB with narrowband and wideband signals in the RF spectrum

Traditional narrowband communications systems modulate continuous waveform (CW) radio frequency signals with a specific carrier frequency to transmit and receive

4

information. A continuous waveform has well-defined signal energy in a narrow frequency band that makes it very vulnerable to detection and interception.

 UWB systems use carrier-less, short-duration pulses with a very low duty cycle for transmission and reception of the information. Low duty cycle offers a very low average transmission power (in the order of microwatts), which directly translates to longer battery life for handheld equipment. The equivalence of a narrow pulse in the time domain to a signal of very wide bandwidth in the frequency domain and vice versa is illustrated in Fig. 1.2.
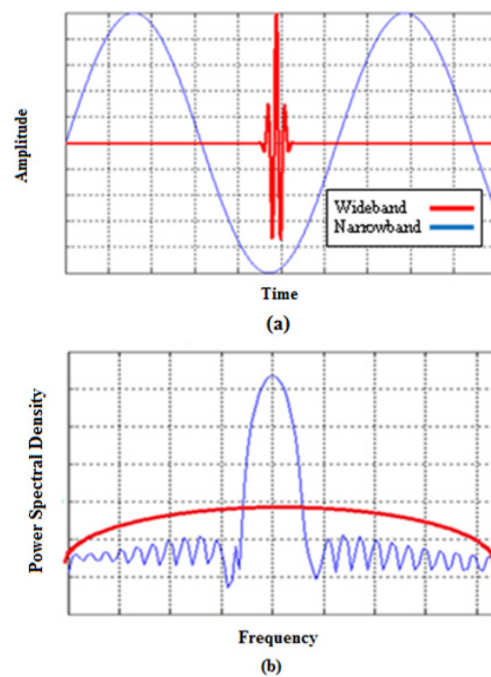
Fig. 1.2   Representation of narrowband and wideband signals in (a)
time domain and (b) frequency domain

There are two general ways to use the available UWB spectrum. The original approach involves the use of very short-duration baseband pulses that occupy bandwidth of

several gigahertz. This is known as single band UWB system and impulse radio falls in this category. The pulse width is very narrow, typically in nanoseconds. The high instantaneous power during the brief interval of the pulse helps to overcome interference to UWB systems, but increases the possibility of interference from UWB to narrow band systems. Since UWB can be any technique that generates signals occupying at least 500 MHz of bandwidth within the spectrum mask placed by FCC, the UWB systems can also be classified as multiband based. This is a recent approach, where the available band is divided into several sub bands. Such a scheme is the multi-band orthogonal frequency division multiplexing (MB-OFDM) UWB system in which the UWB range is divided into 14 subintervals each with a bandwidth of 528 MHz as depicted in Fig. 1.3.
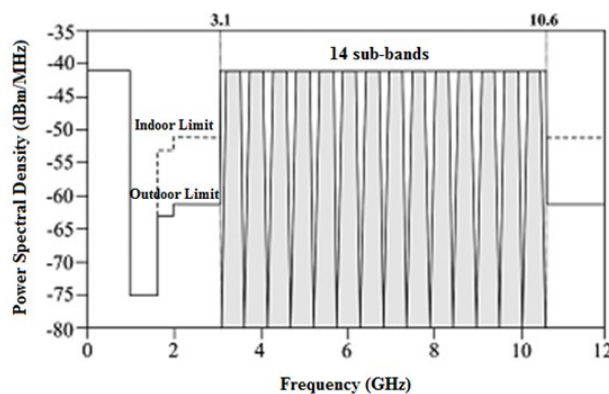
Fig. 1.3   Multi band scheme of UWB systems

UWB technology is a derivative of the time hopping spread spectrum (THSS) technique, a multiple access technology particularly suited for the transmission of extremely narrow pulses. It has been standardized in IEEE 802.15.3a as a technology for WPANs and offers many advantages as listed in Table 1.1.

6

Table 1.1   Advantages and benefits of UWB communications

Advantage	Benefit
Large channel capacity	High bandwidth can support real-time high definition video streaming.
Ability to work with low SNRs	Offers high performance in noisy environments.
Low transmit power	Provides high degree of security with low probability of interception.
Simple transceiver architecture	Enables ultra-low power, smaller form factor and better mean time between failures, all at a reduced cost.

A major step in the development of UWB technology for wireless communications is the antenna. However, there are more challenges and difficulties in designing a UWB antenna than its narrow band counterparts. Unlike the antennas used for narrowband systems, the antenna in a UWB system should have wider bandwidth and smaller dimensions than is conventionally possible. It should be capable of handling high speed pulse trains and this makes its design difficult.

1.3 PRINTED UWB ANTENNAS

Theoretically, frequency-independent antennas, which have a constant performance at all frequencies, can be used for broadband design (Balanis, 1982). Typical designs are the self-complementary log periodic structures such as planar log-periodic slot antennas, bidirectional log-periodic antennas, log-periodic dipole arrays, two/four-arm log spiral antennas and conical log-spiral antennas. However, for the log-periodic antennas, frequency-dependent changes in their phase centers severely distort the waveforms of radiated pulses. Biconical antennas are the earliest antennas constructed

for UWB wireless communication system by Sir Oliver Lodge in 1897 (Schantz, 2003) as shown in Fig. 1.4 (a).

Transmitter Receiver

Tapered
feed

Transmission Line

(a)   (b)
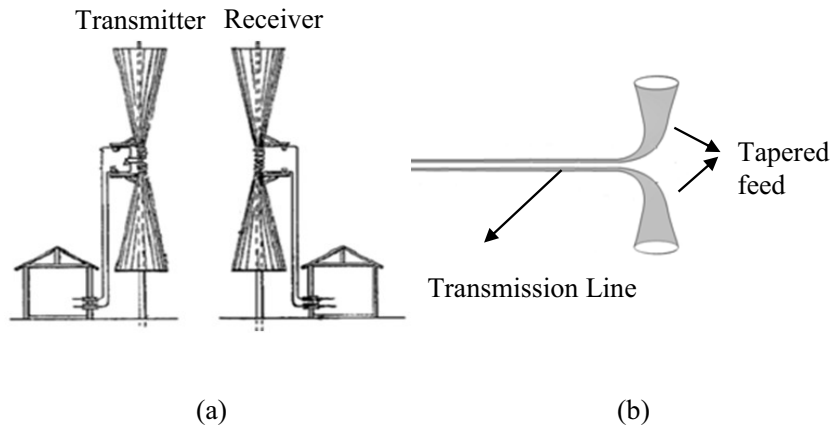
Fig. 1.4   (a) Biconical antenna by Lodge (b) Biconical antenna with
tapered feed by Carter

It can be regarded as a uniformly tapered transmission line excited by transverse electromagnetic (TEM) mode so as to possess wideband input impedance properties. Thicker biconical antennas are more suitable for wide band applications. This is because a 'fatter' structure will lead to a broader bandwidth since the current area and hence the radiation resistance is increased. After that, several types of UWB antennas were developed in the following years and a significant improvement was introduced by P. S. Carter in 1939 by incorporating a tapered feed with Lodge's biconical cone design as shown in Fig. 1.4 (b). This was one of the key steps towards the design of broadband antennas. These antennas featured relatively stable phase centers with broad well-matched bandwidths due to the excitation of TEM modes. Following that, many diverse variations of biconical antennas such as finite biconical antennas, discone antennas and single-cone with resistive loadings were formed and optimized for broad

impedance bandwidths. However, the antennas mentioned above are seldom used in portable devices due to their bulky size or directional radiation.

Alternatively, planar dipoles have been proposed because of their broad bandwidths and small size (Zhong *et al*., 2008). The earliest planar dipole may be the Brown-Woodward bowtie antenna, which is a simple and planar version of a conical antenna. Similarly, one of the poles can be replaced with an electrically large conducting plate acting as a ground plane to form a monopole antenna as shown in Fig. 1.5.

.
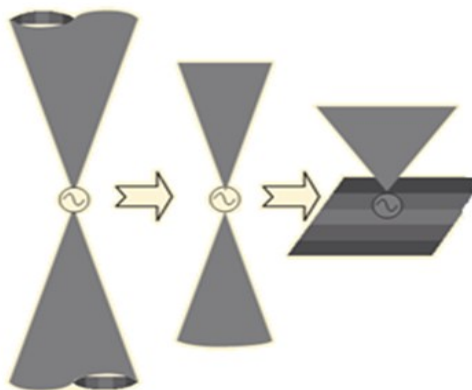
Fig. 1.5   Evolution of the planar monopole antenna

They can be excited by a vertically hoisted coaxial cable. The radiators of the planar monopole antennas can be of any shape for broad operating bandwidth.

A monopole antenna usually consists of a vertical cylindrical wire mounted over the ground plane. Bandwidth increases with increase in diameter of the monopole (Chen and Luk, 2009). A planar monopole antenna can be equated to a cylindrical monopole

9

antenna with large effective diameter and they can have different geometries as shown in Fig. 1.6.
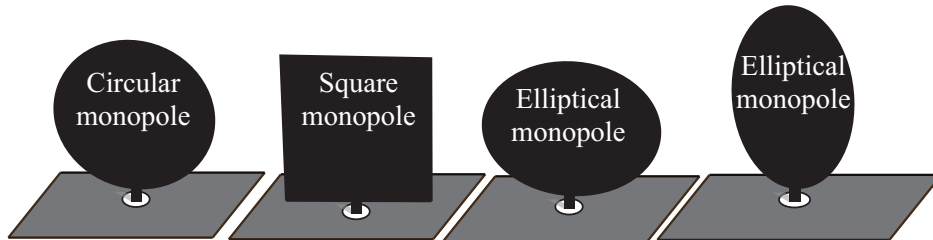
Fig. 1.6   Various configurations of planar monopole antennas

The concept behind the operation of broadband radiators in most cases is in having 'a smooth physical structure'. Such antennas usually require structures that do not have abrupt changes in the physical dimensions involved but instead have smooth boundaries since they tend to produce patterns and input impedances that change smoothly with frequencies.

A bandwidth comparison of several planar monopoles with various geometries, such as circular, elliptical, rectangular, and trapezoidal monopoles was carried out in Bataller *et al*. (2006) and Agrawall *et al*. (1998). The results show that the circular and elliptical monopoles exhibit much wider bandwidth performance than those of others, and both can obtain an impedance bandwidth ratio greater than 10:1. A circular monopole antenna yields a broader impedance bandwidth as compared to a rectangular monopole antenna with similar dimensions because the circular planar monopole is more gradually bent away from the ground plane.

To integrate the antenna into other radio frequency (RF) circuits, the antennas can be readily printed onto a printed circuit board (PCB). In this form, the antenna can be embedded into the casing of devices. To date, printed monopoles with various radiator shapes have been proposed and investigated as shown in Fig. 1.7. They are typically designed for applications in mobile systems (such as 900/1800 MHz bands), WLANs (such as 2.4/5.2/5.8 GHz bands) and UWB (3.1-10.6 GHz band) communications.
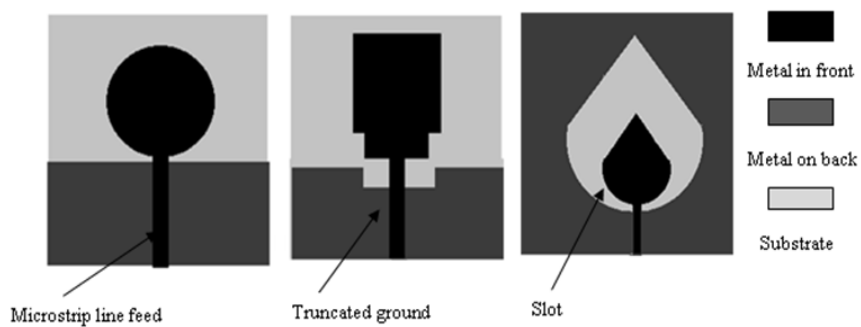
Fig. 1.7   Various configurations of printed monopole antennas

A review of some of the proposed multiband antennas incorporating UWB applications is presented here.

A study on microstrip fed circular monopole antenna is carried out by Liang *et al*. (2005a). It is shown that frequency domain characteristics are determined by ground plane dimensions and the diameter of the disc. The current is mainly distributed along the edge of the disc, which indicates that the first resonant frequency depends on the disc dimension. The antenna's suitability for UWB applications is also proved by carrying out a time domain analysis using a first order Gaussian pulse.

A rectangular monopole is proposed by Choi *et al*. (2004) for UWB applications. Impedance matching is achieved by introducing steps at the bottom of the patch, a slot in the patch and a partial ground plane. The antenna has compact dimensions of 15×14.5 mm^2 and is printed on a substrate of thickness 1.6 mm and relative permittivity 4.4. The measured group delay variation is found to be less than 0.5 ns.

A square patch for UWB operation is presented by Azim *et al*. (2010). A slot is introduced in the ground plane to achieve an impedance bandwidth of 2.95-15.44 GHz. The antenna is fabricated on a substrate of permittivity 4.6 and has an overall size of 14.5×14.5 mm^2. Vector current distributions on the antenna show that four characteristic current modes exist over the bandwidth from 3 to 16 GHz.

Lin *et al*. (2005) presented a paper on a printed planar triangular monopole antenna by using a fire resistant grade 4 (FR-4) printed circuit board substrate. The measured voltage standing wave ratio (VSWR) is less than 3 in the range 4-10 GHz. In the UWB communication frequency range, the measured phase distribution of the input impedance is quite linear and the H-plane patterns are almost omni-directional.

Rambabu *et al*. (2006) have presented a microstrip line fed printed antenna for UWB by using a stepped-patch in combination with multiple resonating elements. The antenna is fabricated on a substrate of permittivity 4.4 and thickness 1.58 mm with overall dimensions of 48×31 mm^2. The antenna exhibits voltage standing wave ratio less than 2 for over 150 % bandwidth from 6-42.8 GHz with gain greater than 1 dBi.

A planar triangular monopole with ridged ground plane is introduced by Lin and Chuang (2008) for impedance matching between 3 and 10 GHz. Triangular-ridged and trapezoid-ridged ground planes are compared and both techniques show increase in impedance bandwidth of the triangular monopole. With the ridged ground plane, a bandwidth improvement from approximately 40 % (for monopole without ridged ground plane) to about 4:1 ultrawideband operating frequency range (3 to 12 GHz) has been demonstrated.

Chen *et al*. (2007) proposed a compact planar antenna in which a notch is introduced in the radiator to reduce ground plane effects. The overall antenna size is 25×25 mm^2 and impedance matching is obtained from 2.9-11.6 GHz. The ground plane effect on impedance performance is greatly reduced by cutting the notch from the radiator because the electric currents on the ground plane are significantly suppressed at the lower edge operating frequencies.

A microstrip line fed antenna for Bluetooth and UWB fabricated on FR-4 substrate with size 42×46 mm^2 is presented by Yildirim *et al*. (2009). The antenna exhibits a dual-band operation covering 2.4-2.484 GHz and 3.1-10.6 GHz frequency bands with an average group delay of 0.2 ns in the UWB range. To minimize the mutual interaction between the two resonances, a strategy based on placing the Bluetooth element in a low-UWB-mode current point is adopted.

A fork-shaped monopole for Bluetooth and UWB operation is developed by Mishra *et al*. (2011). The structure is fabricated on a low-cost FR-4 substrate having dimensions

of 50×24 mm^2. Band notching at WLAN frequency is also achieved by using a pair of L-shaped slots and a pair of symmetrical step slots in the ground plane.

Reddy *et al*. (2013) used two co-planar semicircular dual band-notched monopole antennas to realize a diversity antenna. Dual band notch function is introduced by using two sets of spirals that are capacitance coupled with the feed line of the antenna. The diversity performance of the proposed antenna is analyzed through envelope correlation coefficient, channel capacity loss and antenna radiation pattern.

A microstrip line-fed printed monopole for Bluetooth and UWB operation is proposed by Xiong and Gao (2012). By etching a slot on the current route and placing two symmetrical split rectangular ring resonators to couple with microstrip feed line, band notch is realized at WLAN and worldwide interoperability for microwave access (WiMAX) frequencies. The omni-directional radiation patterns are very stable across the Bluetooth and UWB band and the group delay is less than 1 ns in the working band.

A planar dual-band antenna for Bluetooth and ultrawideband is presented by Shaker *et al*. (2011) with multiple band notches. Notches are introduced for WiMAX, WLAN and C-band frequencies. Two different types of slots, a U-shaped slot and an H-shaped slot etched on the radiating patch plus a U-shaped slot in the ground plane, are used to obtain two and three notched bands respectively.

A compact asymmetric coplanar strip-fed UWB monopole antenna with Bluetooth band is proposed by Liu *et al*. (2014). A staircase shaped patch is used for UWB operation while a snake shaped slot inserted in the patch is used to realize the Bluetooth

band. The antenna has a compact size of 32.1×10 mm^2 and has nearly omni-directional radiation characteristics.

Bod *et al*. (2012) proposed an octagonal-shaped slot fed by a beveled and stepped rectangular patch for covering the UWB band. By attaching three inverted U-shaped strips at the upper part of the slot in the ground, additional triple linear polarized bands are realized. The antenna is suitable for global positioning system (GPS), part of GSM and Bluetooth.

A diamond-shaped quad-band antenna for global positioning system (GPS), GSM, WLAN and UWB applications is presented by Foudazi *et al*. (2012). The diamond-shaped patch covers UWB range and multiband operation is achieved by introducing resonant strips using center feed method within the patch without disturbing UWB operation. The antenna has a compact size of 16×22 mm^2 on a substrate of permittivity 4.4.

From the literature review carried out on printed UWB antennas it is seen that while it is necessary that the antenna covers the frequency band 3.1-10.6 GHz, time domain characterization is also important. Particularly, the group delay variation should be minimal. Also, focus has shifted to incorporating UWB application with lower frequency bands in multiband antennas.

1.4 CPW-FEED

Planar antennas with coplanar waveguide (CPW) feed have received much attention recently due to their ease of integration with monolithic microwave integrated circuits

15

(MMICs). More importantly, it can provide extremely broad frequency response (100 GHz or more) since connecting to CPW does not entail any parasitic discontinuities in the ground plane. The CPW was proposed by C. P. Wen in 1969, and the transmission-line structure of this sort is realized by imprinting metal on a single side of a dielectric substrate as shown in Fig. 1.8.
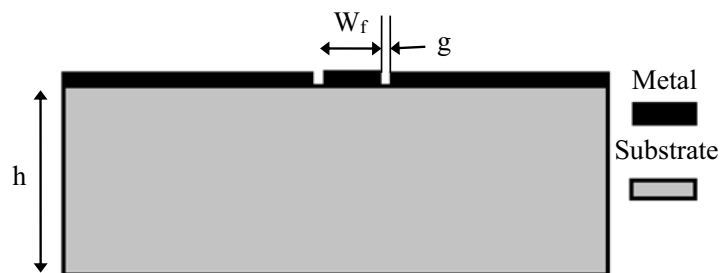
Fig. 1.8   Side view of CPW-feed layout

The metallic layer comprises three metallic sections (center conductor strip and two ground planes). The two ground planes are located on either side of the center strip with a narrow gap. CPWs can be classified into three categories. In a conventional CPW, the ground planes are of semi-infinite extent on either side. However, in a practical circuit the ground planes are made of finite extent. The conductor-backed CPW has an additional ground plane at the bottom surface of the substrate. This lower ground plane provides mechanical support to the substrate and acts as a heat sink for circuits with active devices. Another variation is the micro-machined CPW which is of two types, namely, the micro-shield line (Weller *et al*., 1995) and the CPW suspended by a silicon dioxide membrane above a micro-machined groove (Milanovic *et al*., 1997).

16

The characteristic impedance and effective dielectric constant of coplanar waveguide are determined by the dimensions of the center strip, gap width, the thickness and permittivity of the dielectric substrate. This structure supports a quasi-TEM mode. In the ideal case, the thickness of the dielectric is infinite; in practice, it is thick enough so that EM fields die out before they get out of the substrate. The advantage of coplanar waveguide is that active devices can be mounted on top of the circuit, like on microstrip. More importantly, it can provide extremely high frequency response since connecting to CPW does not entail any parasitic discontinuities in the ground plane. Nowadays monopole antennas with CPW feed are more popular for narrow band and wideband applications due to their attractive features such as low radiation loss, less dispersion, wide bandwidth, uni-planar structure and easy integration with active devices without via holes. A few of the widely used CPW-fed monopole antennas are shown in Fig. 1.9. A review on some of the work carried out on CPW-fed multiband and UWB antennas is presented here.
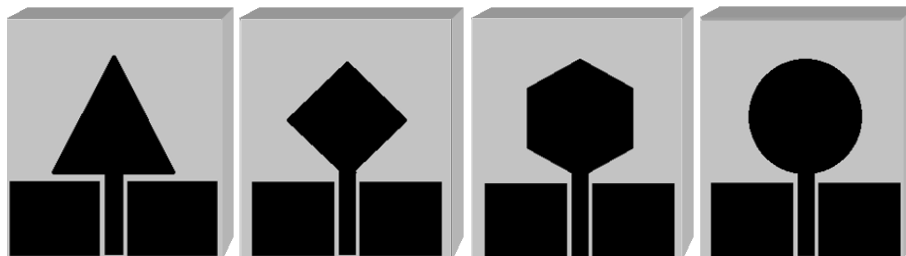
Fig. 1.9   Various configurations of printed CPW-fed narrow band
and wideband antennas

Jacob *et al*. (2010) presented a CPW fed monopole slot antenna for UWB wireless communication. Impedance matching is achieved by inserting slits in the surrounding ground plane and introducing bevels in the ground plane near the feeding point.

17

A CPW-fed pentagon antenna for UWB applications is proposed by Touhami *et al*. (2014). Two techniques are adopted to achieve ultrawideband performance. The first technique is to remove a small fan angle on both sides of the ground plane. In the second technique, the corners of the monopole are beveled to obtain the pentagon shaped monopole. The antenna has an overall size of 22×19 mm^2 on a substrate of permittivity 4.3 and thickness 1.6 mm with operating bandwidth 4.46-21.14 GHz.

Liang *et al*. (2005a) presented a paper on CPW-fed circular disc monopole antenna for UWB applications. A detailed study on effect of ground plane dimensions on antenna reflection characteristics is also carried out. The studies show that a circular disc monopole printed on a dielectric substrate and fed by a 50 Ω CPW can yield UWB characteristics with satisfactory radiation patterns.

Lam and Bornemann (2007) presented a CPW-fed UWB antenna in which stepped transitions are introduced in both the center conductor and ground plane for good impedance matching. The antenna has a size 30×40 mm^2 on a substrate of relative permittivity 4.7.

William and Nakkeeran (2010) proposed a CPW-fed UWB slot antenna. The antenna consists of a cross-shaped structure at the anterior portion of the feed line that acts like a tuning stub. Time domain analysis is also carried out to prove the suitability of the antenna in UWB frequencies. The antenna has an overall size of 20×19 mm^2 on a substrate of relative permittivity 4.4.

Gautam *et al*. (2013) have proposed a CPW-fed UWB microstrip antenna loaded with an inverted L-strip extended from the ground plane over the patch to lower the height of the antenna. The overall size of the antenna is 25×25 mm^2 on a substrate of thickness 1.6 mm and relative permittivity 4.4 and impedance bandwidth is from 2.6-13.04 GHz.

Kim and Jee (2007) used a CPW-fed L-shaped monopole and an I-shaped open stub monopole to form three different surface current paths for UWB operation. The antenna has overall dimensions of 30×25 mm^2 and provides impedance matching from 3-11 GHz with a gain variation of 1.4-4.6 dBi.

The working principles of CPW-fed UWB printed antennas are investigated by Tanyer-Tigrek *et al*. (2010). Using a quasi-magnetic antenna the analysis demonstrates that the most important aspect for achieving UWB characteristics is to ensure current distributions that display traveling-wave characteristics.

Choi *et al*. (2009) have proposed a CPW-fed triangular patch antenna with a pair of wide stubs on the lower side of the patch and linearly tapered coplanar ground plane for achieving wide bandwidth. The antenna has $S_{11} \leq -10$ dB from 2.9-13.2 GHz and group delay is less than 0.94 ns over the entire UWB band.

A CPW-fed UWB antenna with modified ground is presented by Shameena *et al*. (2011). The antenna exhibits a 2:1 VSWR bandwidth from 3.1-12 GHz with a peak gain of 5 dBi and group delay variation less than 2 ns. The antenna has an overall size of 30×22 mm^2 on a substrate of permittivity 4.4 and thickness 1.6 mm.

A new CPW-fed super wideband printed antenna is introduced by Gorai *et al*. (2013). A conventional disc monopole is modified to resemble a propeller shape to produce an extremely wide bandwidth from 3-35 GHz. The antenna has an overall size of 55×38 mm^2 and is fabricated on a substrate of permittivity 4.4.

Yang *et al*. (2009) presented a novel ultrawideband antenna with three pairs of multi-resonant split-ring loops and a CPW feed. Dual concentric microstrip split-ring loops with different geometrical ground planes are analyzed and compared. The proposed antennas have a wide bandwidth from 2-20 GHz.

A compact CPW-fed multi-frequency circular slot antenna design loaded with arc-shaped metallic strips is investigated by Chiang *et al*. (2012). The antenna has an overall size of 40×40 mm^2 on a substrate of thickness 0.8 mm and relative permittivity 4.4. The compact size of the slot antenna is determined by the upper resonant frequency unlike lower resonant frequency as in conventional antennas.

Soni *et al*. (2013) presented a compact integrated Bluetooth and UWB CPW-fed antenna by using modified rectangular tuning stub with notched corner and tapered shape near the feed line. The antenna is fabricated on a substrate of permittivity 4.4 and has a compact size of 26×20 mm^2. Dual frequency band characteristics of the antenna are achieved by creating quarter wavelength C-shaped Bluetooth element near the radiating plane.

A multiband monopole antenna with inverted trapezoidal CPW-feeding is presented by Zhang *et al*. (2014). The antenna has a size of 15x50 mm^2 on a substrate of permittivity

4.4 and thickness 1.6 mm with ground plane dimensions of 100×50 mm^2. Impedance bandwidth from 770-1100 MHz and 1690-2950 MHz are obtained with gain in the range 1.8-2.3 dBi and 3.5-5 dBi respectively.

A CPW-fed meander resonator is combined with a folded resonator and integrated into a single monopole to produce a multiband antenna for GSM, GPS, PCS and wideband code division multiple access (W-CDMA) by Baek and Jee (2011). The antenna is fabricated on a substrate of relative permittivity 7.3 and has a compact size.

A fork-shaped CPW-fed monopole antenna is presented by Darvish and Hassani (2012). The multi-band antenna is obtained by adding an inverted U-shaped strip on it. The proposed antenna covers frequency bands including universal mobile telecommunication service (UMTS), Bluetooth, WLAN and WiMAX application. Two such antenna elements are placed in orthogonal configuration and studied for multiple input multiple output (MIMO) applications.

Lee *et al*. (2011) proposed a multi-band CPW-fed metamaterial antenna. A meander monopole and two open-ended stubs attached parallel to the meander are used to create the metamaterial structure. The antenna has an overall size of 25×20 mm^2 and its lowest frequency of operation is 740 MHz.

A CPW-fed antenna for multi-band operation covering the digital video broadcasting signal reception in the UHF band, GSM band and the 2.4 GHz 802.11g/n band is introduced by Lee *et al*. (2012). The size of the antenna is 114×60 mm^2 on a substrate of permittivity 4.4 and lowest frequency of operation is 470 MHz.

A CPW-fed planar quasi-Yagi antenna with CPW-to-coplanar strip (CPS) transition for multiband operation with directional radiation pattern is proposed by Ding *et al*. (2011). This structure can transform even-mode electrical field at the CPW line to odd-mode electrical field at the CPS line to enable multiband operation.

Chen *et al*. (2014) studied the use of stepped impedance resonators in CPW-fed multiband and broadband slot antennas. The antenna is fabricated on a substrate of permittivity 4.4 and in comparison to the conventional uniform-impedance resonator; the proposed resonator shows a better control over spurious response.

1.5 MOTIVATION AND OBJECTIVE

The motivation for integrating multiple applications in one antenna is due to the current trend for short-range wireless systems of beyond 3G, which are envisioned to enable wireless connectivity for "everybody and everything at any place and any time". This ambitious goal requires a comprehensive integration of existing and future wireless systems that link devices as diverse as portable and fixed appliances, personal computers (PCs) and entertainment equipment. Consumer electronics like wireless universal serial bus (USB) and Bluetooth applications require narrow planar antennas with a width of only a few centimeters. However, with the reduction of antenna size, impedance bandwidth degrades. The trade off in integrating UWB and lower frequency standards into a single antenna geometry is the geometrical asymmetry introduced by the lower band element. Also, since compact antennas show significant ground plane length/shape effects on its performance, it is important to design antennas resistant to

such effects. The conflicting requirements of good performance and compact size make the design of such antennas challenging.

The objective is to explore properties of fractal, slotted and spiral monopole structures to develop novel compact CPW-fed multiband antennas incorporating UWB applications. Radiation characteristics of the antennas are studied in both frequency and time domains. The designs proposed are CPW-fed fractal multiband antenna, CPW-fed slotted multiband antennas and CPW-fed spiral multiband antennas. The antennas are built on a low-cost substrate that enables the integration of different operation bands onto a compact and light weight substrate suitable for mass production.

1.6 THESIS ORGANIZATION

The thesis presents a study on the radiation characteristics of CPW-fed multiband antennas incorporating UWB applications. In all the antennas, lower band operation is introduced without increase in overall size of the UWB antenna which makes the design compact.

Chapter 1 of the thesis presents an overall introduction to UWB technology and discusses the evolution of printed UWB antennas. The significance of CPW-feed technique is also highlighted followed by the motivation and objective of the thesis.

Chapter 2 presents the experimental and simulation methodology utilized for the analysis of antennas described in the thesis. The electromagnetic simulation tool high frequency structure simulator (HFSS™) which is used for simulation studies is presented and fabrication steps are explained. Measurements in the frequency domain

such as return loss, radiation pattern, gain and the relevant theory behind time domain measurements and the quantification of measured results are elaborated.

Chapter 3 deals with the design and characterization of a CPW-fed fractal multiband antenna. This chapter begins with a literature survey on fractal antennas for UWB systems. The fractal antenna is developed for triple-narrowband operation. Detailed parametric analysis is performed at each stage of the evolution of the antenna to develop the design equations. Experimental results are compared with simulated results and the antenna is compared with some of the fractal multiband antennas in literature.

Chapter 4 deals with CPW-fed slotted multiband antennas. A literature survey on slot antennas for UWB systems is given at the beginning of the chapter. Geometry, design and optimization of a dual-band circular antenna suitable for UWB applications is presented. Then a fractal design is introduced to obtain dual-band characteristics with improved impedance matching in the UWB band. A third design is also presented in which a bent monopole is introduced in the structure for triple-band operation. Experimental results in the frequency domain and time domain are presented for all three antennas followed by conclusions.

Chapter 5 deals with CPW-fed spiral multiband antennas. A detailed literature survey of wideband spiral antennas is presented at the beginning of the chapter. In this chapter, first a design is presented for a dual-band spiral antenna for UWB applications. This is followed by a modified design to cover lower frequencies of operation. Antenna geometry, design and optimization are explained and experimental results in the frequency domain and time domain are presented.

Chapter 6 gives the summary and conclusion of the overall work and a brief description on the scope for future investigations.

Appendix A presents a CPW-fed UWB antenna with dual notch bands created by slots introduced in the feed line and ground plane.

Appendix B presents frequency and time domain characterization of a CPW-fed dual-band spiral antenna with UWB application. This work is carried out to validate design equations developed in Chapter 5 for a different substrate.

Chapter 2

METHODOLOGY

The methodology adopted for simulation studies and subsequent measurement techniques are crucial in determining the antenna characteristics. Parametric analysis for all the proposed antennas are carried out using Ansys HFSS™ and from the parametric analysis results obtained using the software, a design guideline is formulated using regression analysis. Photolithography is used to fabricate the antennas on microwave laminates and measurements are carried out at the test facility consisting of programmable network analyzer (PNA) and anechoic chamber. A description of the measurement techniques for frequency and time domain is presented here.

2.1 ANTENNA FABRICATION

Photolithographic technique is used to fabricate the antenna on a laminate. A negative mask of the antenna geometry is first printed on butter paper. A single sided copper clad lamination of suitable dimension is then cleaned with acetone to remove impurities. This is immersed in photo resist and allowed to dry so as to form a thin film of the photo resist on the laminate. The photo resist coated clad with the antenna mask carefully aligned over it is then exposed to ultra violet (UV) radiation. During this process, exposed portions of photo resist harden, while the unexposed region remains unaffected. The laminate is then immersed in developer solution in a dark room. Next, the laminate is placed in ferric chloride solution and gradually agitated till all the unwanted copper in unexposed regions dissolves, leaving behind the antenna pattern.

Microwave circuits need to be fabricated on low loss, thermally stable substrates with constant permittivity across the operating band. Prototypes of the antennas presented in the thesis have been fabricated on FR-4 glass epoxy of relative permittivity 4.4 and thickness 1.6 mm. It is a widely used substrate as it is very economical. However, it is very lossy at high frequencies but this enables the evaluation of radiation characteristics in the worst-case scenario. Fabrication is also carried out on Rogers RT/Duroid 5880 substrate for the CPW-fed spiral multiband antenna Type-II to validate design equations.

2.2 ANTENNA MEASUREMENT FACILITIES

The Agilent PNA E8362B series microwave network analyzers provide a comprehensive solution for the characterization of either active or passive networks over the 45 MHz to 50 GHz frequency range. For all frequency domain measurements, the network analyzer at the antenna research facility at center for research in electromagnetics and antennas (CREMA), Dept. of Electronics, CUSAT is used. For gain measurement, readings are taken by mounting the antenna under test (AUT) on a microcontroller based turn table assembly interfaced with a computer. A linearly polarized wideband standard horn antenna is used as the transmitter while the AUT is used as the receiver for the radiation pattern measurement. Both the AUT and the horn antenna are placed in an anechoic chamber. This is a room lined with microwave absorbers on the walls, roof and floor to minimize electromagnetic reflections. During measurement, a MATLAB$^{®}$ based graphical user interface (GUI) synchronizes all components in the measurement setup and performs the antenna characterization.

Measurement of the antenna's transient response can be performed either in time domain or in frequency domain followed by inverse Fourier transform. Measurements in time domain, using very short pulses or step functions as driving voltage, can be faster than measurements in frequency domain (Bazaz *et al*., 2011; Kumar *et al*., 2011; Lim *et al*., 2008; Powell and Chandrakasan, 2004). However, frequency domain measurements take advantage of the high dynamic range and the standardized calibration of the network analyzer (Koohestani *et al*., 2013; Elmansouri and Filipovic, 2011; Nazli *et al*., 2010; Sorgel *et al*., 2003). In this thesis, antenna transient response is evaluated by frequency domain measurement.

2.3 ELECTROMAGNETIC SIMULATION TOOL

Ansys HFSS™ is a popular commercial software for the study of electromagnetic structures using finite element method (FEM) solver (HFSS, 2005). The optimization tool available with HFSS™ is very useful for antenna engineers to study the effect of various design parameters. There are several boundary schemes available in HFSS™ of which, radiation and perfect electric conductor (PEC) boundaries are widely used in this work. The vector as well as scalar representations of simulated electric field intensity, E, magnetic field intensity, H and current density, J values give a good insight into the behaviour of the antenna at various frequencies.

2.4 MULTIVARIABLE REGRESSION ANALYSIS

To obtain a desired lower resonance on an arbitrary substrate, a generalized design equation is formulated using the regression tool in Microsoft excel (Remenyi *et al*., 2011). It is a powerful tool that relates multiple independent variables to a dependent

variable. The variable that is to be predicted is known as the dependent variable and the variables of known values that are used for prediction are independent variables. In the cases described in this thesis, the independent variables are the height of the substrate, h (in mm), relative permittivity, ϵ_r of the substrate and resonant frequency, f (in GHz) (Bindu, 2015). The dependent variable is the parameter dominantly controlling the lower resonance band. Extensive simulation studies are carried out by varying each of the independent variables while keeping others constant. Based on the simulation results, a database is developed and from these values, the regression tool is used to obtain the design equation.

2.5 FREQUENCY DOMAIN CHARACTERIZATION

2.5.1 Reflection Characteristics

When a transmission line is not terminated in its characteristic impedance, mismatch at the load cause a backward travelling wave to propagate down the transmission line which results in standing waves. Reflection coefficient Γ is defined as the ratio of the reflected wave voltage (or current) to the incident wave voltage (or current). Impedance bandwidth indicates the bandwidth for which the antenna is sufficiently matched to its input transmission line such that less than 10 % of the incident signal is lost due to reflections (Mobashsher *et al*., 2011). An acceptable value of Γ that enables only 10 % of reflected power is $\Gamma = 0.3162$.

Voltage standing wave ratio (VSWR) measures the ratio of the maximum amplitude to the minimum amplitude of the standing wave (Pozar, 2011). Typically, a VSWR value of 2.0 or less indicates a good impedance match. This is obtained from the relation

$$VSWR = \frac{1+|\Gamma|}{1-|\Gamma|} \qquad\qquad (2.1)$$

Return loss is another measure of impedance match quality, and is dependent on Γ as

$$\text{Return loss} = -20\log_{10}|\Gamma| \qquad\qquad (2.2)$$

The reflection coefficient Γ expressed in dB is equivalent to the S_{11} parameter of the scattering matrix and is expressed as

$$S_{11} = 20\log_{10}|\Gamma| \qquad\qquad (2.3)$$

Impedance bandwidth of an antenna is evaluated as the range for which $\Gamma < 0.3162$, VSWR < 2, Return loss > 10 dB or $S_{11} < -10$ dB.

In order to measure the reflection characteristics of the AUT, it is connected to any one of the network analyzer ports. S_{11} or S_{22} measurement option of the chosen PNA port is selected and the port is then calibrated for the required frequency range using standard open, short and matched loads before connecting the AUT. During measurement, the scattering parameter values captured over the frequency band of interest are stored in .csv format using the indigenously developed measurement automation software – CREMA SOFT.

2.5.2 Radiation Pattern

Radiation pattern of an antenna is the spatial distribution of electromagnetic energy emanating from the antenna. Though the pattern has a three-dimensional distribution,

measurement is carried out in only two principal planes due to limitations of the measurement setup.

The radiation pattern measurement is carried out in the anechoic chamber with the help of Agilent PNA E8362B. The AUT is mounted on a turntable assembly placed in the anechoic chamber and connected to one port of the network analyzer. It is configured in the receiver mode. The other port of the network analyzer is connected to a wideband horn which acts as the transmitter. The AUT and horn antenna are spatially separated such that measurement is carried out in far field. Initially the two antennas are aligned along bore-sight. Then the turn table assembly rotates the AUT in increments of 5º. Meanwhile, the system interfaced to the turn table performs the S_{21} measurement for each step angle and records the angular transmission characteristics in a data file. In each principal plane, measurements are taken for two orthogonal orientations of the horn antenna to obtain co-polarization and cross-polarization readings.

2.5.3 Antenna Gain

The most important figure-of-merit that describes the performance of a radiator is the gain. It is defined as the ratio of the intensity in a given direction to the radiation intensity that would be obtained if the power accepted by the antenna were radiated isotropically. There are two basic methods to evaluate gain: absolute gain and gain transfer measurements. Gain transfer method must be used in conjunction with standard gain antennas to determine gain of the AUT. On the other hand, absolute gain method requires no *a priori* knowledge of the gains of the antennas used. The two-antenna absolute gain method is adopted for gain measurements in the thesis.

Two antennas with identical radiation characteristics are placed in far field and aligned for maximum directional radiation. Based on Friis transmission formula, gain of the antenna can be evaluated using the relation

$$(G_t)dB + (G_r)dB = 20log_{10}\left(\frac{4\pi r}{\lambda}\right) + 10log_{10}\left(\frac{P_r}{P_t}\right) \qquad (2.4)$$

where r is the separation distance, λ is free space wavelength, G_t is the gain of transmitting antenna, G_r is the gain of receiving antenna, P_t is the transmitted power and P_r is the received power. The gain is calculated for different orientations of the AUT. The maximum gain obtained from all the orientations at a particular frequency is chosen to plot peak gain of the antenna.

2.5.4 Antenna Efficiency

Radiation efficiency is defined as the ratio between the total power radiated by the antenna and the power delivered into the antenna. The Wheeler Cap method is conventionally used to measure radiation efficiency of narrow band antennas. This method takes into account the reflected power due to mismatch as an explicit loss.

The proposed antennas are designed to work in narrow bands at lower frequencies and throughout UWB range. To measure efficiency in the UWB range as well, a modification of the Wheeler Cap method is used. In the conventional method used for narrow band antennas, the radiation from the antenna is restricted to a radiation sphere of radius $\lambda/2\pi$, where λ is free space wavelength. In the UWB Wheeler Cap method, first the antenna is allowed to radiate in free space. Then a second set of measurements are taken, in which the antenna receives its transmitted signal after reflection.

The power budget for a transmit antenna may be expressed in terms of power fractions. A fraction of the incident power, P_{in} is dissipated in losses ($l = P_{loss} / P_{in}$), a fraction is reflected away due to mismatch ($m = P_{refl} / P_{in}$) and a fraction is radiated ($\eta = P_{rad} / P_{in}$). Averaging over a suitable time interval and applying conservation law:

$$l + m + \eta = 1 \tag{2.5}$$

The oblate shell surrounding the AUT enforces a near ideal time reversal of the transmitted signal. Thus, the antenna receives the reflected signal with negligible structural scattering, and the antenna mode scattering term is simply the mismatch fraction ($m = |S_{11\text{-}FS}|^2$). By reciprocity theorem, the efficiencies (η) in receive and transmit mode are identical. The scattering coefficient inside the UWB Wheeler Cap becomes (Schantz, 2002):

$$|S_{11-WC}|^2 = m + \eta^2 + \eta^2 m^1 + \eta^2 m^2 + \eta^2 m^3 + \cdots$$

$$= |S_{11-FS}|^2 + \eta^2 \sum_0^\infty |S_{11-FS}|^{2n}$$

$$= |S_{11-FS}|^2 + \eta^2 \frac{1}{1-|S_{11-FS}|^2} \tag{2.6}$$

which solves to yield the following result for the radiation efficiency:

$$\eta = \sqrt{(1 - |S_{11-FS}|^2)(|S_{11-WC}|^2 - |S_{11-FS}|^2)} \tag{2.7}$$

For measurements, an oblate metallic chamber with diameter 70 cm is used. First, the AUT is placed in free space and the reflection coefficient S_{11-FS} is measured. It is then

placed at the center of the closed metallic chamber and the reflection coefficient S_{11-WC} is measured. Finally, (2.7) is used to calculate the radiation efficiency.

2.5.5 Group Delay

An antenna in a UWB system can be analyzed as a filter by means of magnitude and phase responses. When a signal passes through a filter, it experiences both amplitude and phase distortions depending on the characteristics of the filter. By representing the receiver/transmitter antenna as a filter, the phase linearity within the frequency band of interest can be determined by looking at its group delay (Ifeachor and Jervis, 1993). Group delay is defined as the negative derivative of the filter phase with respect to frequency. It characterizes the frequency dependence of the time delay and gives an indication of the dispersive nature of the device.

For a device with frequency response $H(\omega) = A(\omega)e^{j\theta(\omega)}$

$$\text{Group delay } \tau = -\frac{d\theta(\omega)}{d(\omega)} \tag{2.8}$$

In impulse radio, communication is by means of serial pulses with a very low duty cycle. The pulse input to the antenna system has an extremely large bandwidth and hence, any variation in group delay across the pass band of the antenna will tend to distort the pulse. A non-distorting antenna geometry is characterized by a constant group delay, i.e., linear phase, in a relevant frequency range. Nonlinear group delay indicates the resonant character of the device, which shows the ability of the structure to store energy.

To evaluate the group delay, two antennas with identical radiation characteristics are placed 15 cm apart in three different orientations: face to face, face to side and side to side. The two antennas are connected to ports 1 and 2 of the network analyzer and S_{12} or S_{21} measurement option of the PNA is selected. The ports of the analyzer are calibrated using the standard open, short and matched load for the frequency range of interest, prior to the measurement.

2.6 TIME DOMAIN CHARACTERIZATION

2.6.1 Transfer Function and Impulse Response

In the best-known embodiment, UWB systems communicate using a series of narrow un-modulated pulses instead of using a high frequency carrier. The pulse can be seen as a burst of radio frequency (RF) energy where each pulse carries one symbol of information. Hence it is not sufficient to evaluate the antenna performance solely through traditional frequency domain parameters such as return loss, radiation patterns and gain.

The effects of antenna on the signal transmission can be analyzed by considering the envelope of the transient response. The transient response is measured by a frequency domain measurement followed by inverse Fourier transformation. Frequency domain measurements are carried out by modeling the antenna as a linear time invariant (LTI) system. Consider the UWB channel model shown in Fig. 2.1.
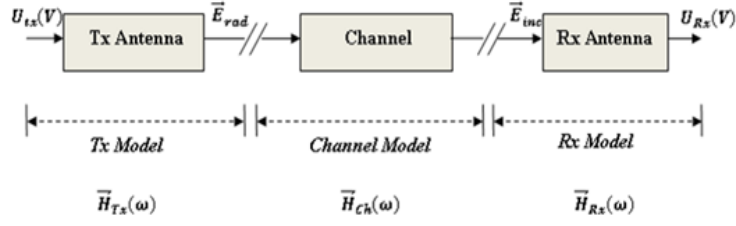
Fig. 2.1 UWB system channel model

The frequency domain relation between received voltage pulse $U_{Rx}(\omega, r, \theta, \varphi)$ and incident electric field pulse $\vec{E}_{rad}(\omega, r, \theta, \varphi)$ (Weisbeck *et al.*, 2009) is

$$\frac{U_{Rx}(\omega,r,\theta,\varphi)}{\sqrt{z_c}} = \vec{H}_{Rx}(\omega, \theta, \varphi)\frac{\vec{E}_{rad}(\omega,r,\theta,\varphi)}{\sqrt{z_0}} \qquad (2.9)$$

Where z_c and z_0 are characteristic impedance of the antenna port and free space. The transfer function of the receiving antenna $\vec{H}_{Rx}(\omega, \theta, \varphi)$ is a function of the direction of arrival of the incident field pulse.

The frequency domain relation between transmitted electric field pulse $\vec{E}_{rad}(\omega, r, \theta, \varphi)$ and incident voltage pulse $U_{Tx}(\omega, r, \theta, \varphi)$ is

$$\frac{\vec{E}_{rad}(\omega,r,\theta,\varphi)}{\sqrt{z_0}} = \vec{H}_{Tx}(\omega, \theta, \varphi)\frac{e^{-j\omega\frac{r}{c}}}{r}\frac{U_{Tx}(\omega,r,\theta,\varphi)}{\sqrt{z_c}} \qquad (2.10)$$

where $\qquad \vec{H}_{Tx}(\omega, \theta, \varphi) = \frac{j\omega}{2\Pi c}\vec{H}_{Rx}(\omega, \theta, \varphi)$ $\qquad (2.11)$

Substituting (2.10) in (2.9)

$$\frac{U_{Rx}(\omega,r,\theta,\varphi)}{\sqrt{z_c}} = \vec{H}_{Rx}(\omega, \theta, \varphi)\vec{H}_{Tx}(\omega, \theta, \varphi)\frac{e^{-j\omega\frac{r}{c}}}{r}\frac{U_{Tx}(\omega,r,\theta,\varphi)}{\sqrt{z_c}} \qquad (2.12)$$

Now the whole input to output characteristic is given as

$$S_{21} = \frac{U_{Rx}(\omega,r,\theta,\varphi)}{U_{Tx}(\omega,r,\theta,\varphi)} = \vec{H}_{Rx}(\omega,\theta,\varphi)\vec{H}_{Tx}(\omega,\theta,\varphi)\frac{e^{-j\omega\frac{r}{c}}}{r} \qquad (2.13)$$

Substituting (2.11) in (2.13), transfer function of the antenna can be determined from the measured values of S_{21} using the relation

$$\vec{H}_{Rx}(\omega,\theta,\varphi) = \sqrt{(2\Pi c r S_{21}e^{j\omega r/c})/j\omega} \qquad (2.14)$$

To measure the antenna performance as a system, a pair of the antenna under test are placed in their far field distance, r as shown Fig.2.2.
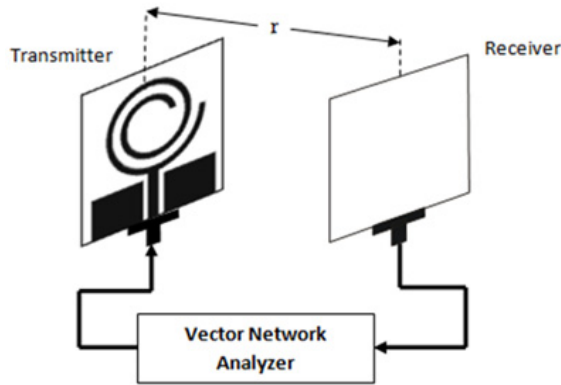
Fig. 2.2   Measurement setup for time domain response

One antenna is used as a transmitter while the other antenna is used as receiver. Measurement is performed for different spatial orientations of the two antennas. The impulse response of the antenna is obtained by taking the inverse fast Fourier transform (IFFT) of the transfer function (Liang, 2006). The data for UWB range is measured from 1 to 11 GHz. It is assumed that the antenna's response is so poor out of band that the data obtained is clearly dominated by noise and it might be advantageous to zero

37

pad data in those frequency ranges. Hence, the data is zero padded from 0 to 1 GHz. To correspond to the spectrum of a real signal, the conjugate of the zero-padded data is taken and reflected to the negative frequencies. This results in a double-sided spectrum which is symmetric around DC. The IFFT of the resulting data in frequency domain gives a real impulse waveform.

A measure for the linear distortion of the antenna is the envelope width, which is defined as the full width at half maximum (FWHM) of the magnitude of the transient response. If p is the peak value of the antenna's transient response,

$$FWHM = t_2|_{p/2} - t_1|_{p/2}, t_1 < t_2 \qquad (2.15)$$

The duration of ringing is defined as the time until the envelope has fallen from the peak value, p below a fraction α of the main peak.

$$Ringing = t_2|_{\alpha p} - t_1|_p, t_1 < t_2 \qquad (2.16)$$

The lower bound for α is chosen according to the noise floor of the measurement. In order to compare the ringing of antennas with different gains under the constraint of constant noise floor, the fraction α is chosen to be $\alpha = 0.22$ (–13 dB).

2.6.2 Choice of UWB Pulse

As mentioned in Chapter 1, the FCC constrains the radiated power of UWB systems to –41.3 dBm/ MHz as depicted in Fig. 2.3.

In UWB systems used for impulse radio, a series of un-modulated pulses are used for communication and each pulse carries one symbol of information. The pulse width is

very narrow and it can be any function which satisfies the spectral mask regulatory requirements.
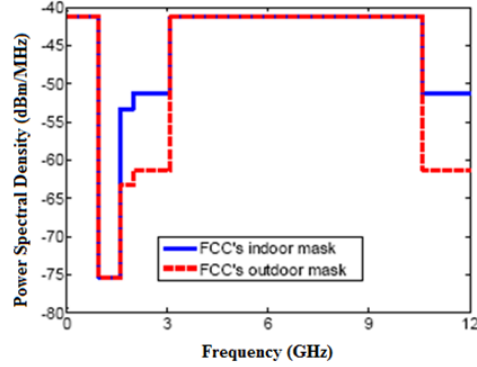
Fig. 2.3 FCC's spectral mask for UWB systems

In principle, all impulses with a spectrum wider than 500 MHz, can be used as UWB signals. However, the choice of the pulse shape is a key design decision in UWB systems. Given the stringent transmission power limitations, the received SNR can be maximized by efficient utilization of the bandwidth and power stipulated by the FCC masks. To satisfy these regulations, it is desirable to use a UWB pulse with very narrow pulse width, typically in nanoseconds. This ensures that the pulse energy will be spread over a wide frequency which minimizes the potential for interference with other user systems. A common choice of the UWB pulse waveform is the Gaussian pulse and has been used in earlier studies of UWB antennas (Norman and Beaulieu, 2005; Chen and Kiaei, 2002; Taylor, 1995). The general form of a Gaussian pulse is

$$V_G(t) = e^{-\left(\frac{t-1}{\sigma}\right)^2} \tag{2.17}$$

where σ is the pulse parameter defined as full width at half maximum.

Small σ corresponds to a pulse that is narrow in the time domain and wide in the frequency domain. However, the power spectral density (PSD) does not comply with the FCC emission mask and so it is not a suitable choice. Higher order derivatives of the Gaussian pulse (Karimabadi and Attari, 2010; Gao et al., 2007; Mao and Chen, 2007) are found to provide a better match to the required FCC emission mask. As the order of the derivative pulse increases, energy moves to higher frequencies. Fig. 2.4 (a) shows the Gaussian pulse and its derivatives shifted in time axis to distinguish between the different pulses. By a suitable choice of pulse parameter and order of the derivative, a pulse that satisfies the regulatory mask can be designed. From Fig. 2.4 (b), it is seen that the fourth derivative Gaussian pulse with $\sigma = 67$ ps conforms best to the FCC indoor emission mask and so this pulse is used for studies in the thesis.
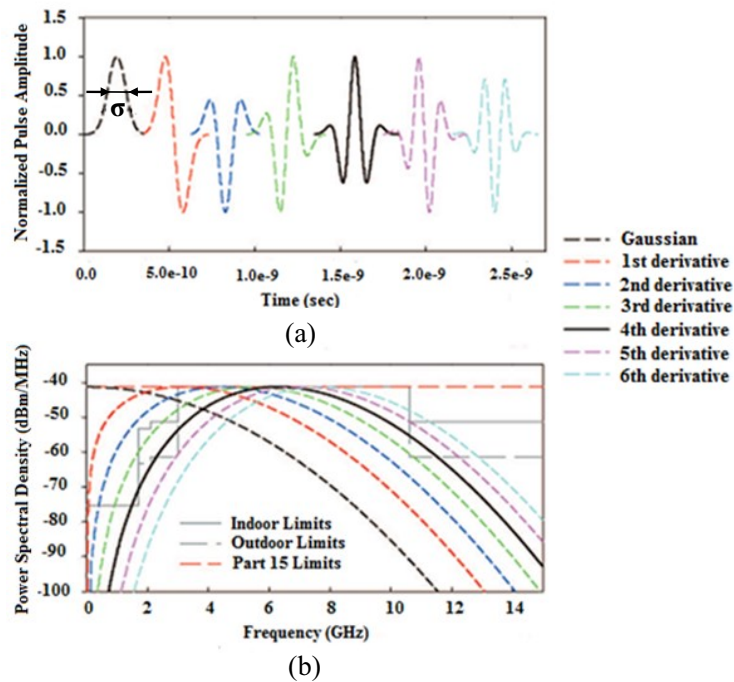
Fig. 2.4   Gaussian pulse and its derivatives (a) Normalized waveform in time domain (b) Power spectral density

The fourth derivative pulse is of the form (Liang, 2006)

$$V_G(t) = \left[\frac{12}{\sigma^4} + \frac{48}{\sigma^6}(t-1)^2 + \frac{16}{\sigma^8}(t-1)^4\right] e^{-\left(\frac{t-1}{\sigma}\right)^2} \qquad (2.18)$$

2.6.3 Fidelity Factor

Ideally, an impulse antenna should faithfully reproduce the transmitted pulse on reception. But the changes in the phase center and radiation characteristics alter the integrity of the transmitted pulses. The non-linearity in the antenna phase response leads to pulse dispersion. To analyze the extent of pulse distortion, the antenna impulse responses for different orientations that are evaluated as described in Section 2.6.1 and the input pulse described in Section 2.6.2, are convolved to obtain the received pulse in the various orientations. The quality of the received pulse in each orientation is assessed using the parameter fidelity factor (Tan *et al.*, 2013). If the input pulse is $s_i(t)$ and the received pulse is $s_o(t)$, then the fidelity factor *FF* is described by the equation

$$FF = max\left(\frac{\int_{-\infty}^{+\infty} s_i(t)s_o(t-\tau)dt}{\sqrt{\int_{-\infty}^{+\infty}|s_i(t)|^2 dt \int_{-\infty}^{+\infty}|s_o(t)|^2 dt}}\right) \qquad (2.19)$$

Fidelity factor is the maximum of the correlation coefficient between the input and output pulse obtained for varying delay, τ. It reflects the similarity between the shapes of the two pulses. For an ideal antenna system that does not distort the input pulse at all, *FF* will be unity as input and output are identical. As distortion increases, *FF* decreases and a minimum value of zero indicates that the input and output pulses are entirely different. High fidelity is desirable in UWB systems.

2.6.4 Radiated Power Spectral Density

UWB systems may cause interferences to other wireless systems since they operate over a large frequency range, which covers many bands being used. Thus, the emission limit is a crucial consideration for the design of UWB antennas. To determine whether the antenna complies with FCC limits in the frequency band of operation, radiated power spectral density is evaluated from Fourier transform of autocorrelation, $R_x(\tau)$ of the radiated pulse as

$$S_x(f) = \int_{-\infty}^{+\infty} R_x(\tau) \exp(-j2\pi f\tau) \, d\tau \qquad (2.20)$$

2.7 CHAPTER SUMMARY

This chapter discusses the methodology adopted for simulation, fabrication and measurement of the multiband UWB antennas presented in the thesis. A detailed account of the frequency domain parameters such as reflection coefficient, gain, efficiency and radiation pattern are provided. In addition to this, important characterizations for UWB range such as group delay is also explained. For time domain analysis of the antenna as a system, details of UWB pulse used as input, transfer function determination and corresponding impulse response of the antenna and evaluation of FWHM, ringing, fidelity factor and radiated power spectral density are also discussed.

Chapter 3

CPW-FED FRACTAL MULTIBAND ANTENNA

Fractals are space-filling geometries defined with an iterative technique resulting in self-similar characteristics. It is a shape that appears similar at all scales of magnification. There are many mathematical structures that are fractals; e.g. Sierpinski's gasket, Cantor's comb, Von Koch's snowflake and the Mandelbrot set. The terms fractal was coined by Mandelbrot, the first person associated with the mathematics of fractals (Mandelbrot, 1983). Fractals have unique properties that can be enticing for antenna designers. Their space-filling property enables miniaturization of antennas since electrically large features can be efficiently packed into small areas, (Gianvittorio and Rahmat-Samii, 2002; Puente *et al*., 1998). The self-similar characteristics of fractals encourages their study as a multiband solution since a self similar antenna will operate in a similar manner at several wavelengths.

When the operating wavelength is large compared to the size of the antenna, the magnitude of the antenna reactance becomes large compared to its radiation resistance (McDonald, 2003). This poses the challenge that an effective impedance matching circuit is needed between the feed line and the antenna. Fractals present the advantage that it is possible to lower the reactance of the antenna by changing the shape of its conductors without increasing the overall size of the antenna. Since any arbitrarily random shape can pick up electromagnetic waves, fractals as antennas may offer more controlling parameters to the designer. A brief account of some of the recent work carried out on fractal antennas for multiband applications is presented here.

A multiband antenna using fractal-like geometrical structures is proposed by Aziz *et al*. (2011). The antenna can support operation in upto five bands and has an overall size of 62×89.6 mm^2 on a substrate of thickness 0.78 mm and relative permittivity 4.7. Triple-band and quad-band structures are fabricated and operating bands are suitable for global system for mobile (GSM), digital cellular systems (DCS), international mobile telecommunications for year 2000 (IMT-2000) and world inter-operability for microwave access (WiMAX) applications.

Saidatul *et al*. (2009) developed a fractal planar inverted-F antenna (PIFA) for multiband applications in GSM, universal mobile telecommunications system (UMTS) and high performance radio local area network (HiperLAN) bands with -6 dB operating frequency ranges from 1.9-2.1 GHz, 1.885-2.2 GHz and 4.8-5.8 GHz respectively. The fractal PIFA is fabricated on a substrate of thickness 0.813 mm and relative permittivity 3.38 and has an overall size of 27×27 mm^2. The antenna is incorporated into a mobile phone and a detailed study is also carried out on specific absorption rate (SAR) levels. This is done to evaluate the antenna performance in the presence of a human body with emphasis on the human head.

Mirkamali *et al*. (2010) have presented a modified multiple ring monopole antenna for multiband applications. The antenna consists of four half rings and a half disk and is fabricated by printing on a 0.8 mm thick substrate of relative permittivity 4.4. The antenna is then mounted perpendicularly over a metallic ground plane of size 150×150 mm^2. The -10 dB bands are 1.65-2.35 GHz, 3.5-5 GHz and 6.5-10.1 GHz respectively.

A CPW-fed multiband antenna using the Sierpinski gasket fractal is proposed by Kaur *et al*. (2012). The antenna is designed on a substrate of relative permittivity 4.4, thickness of 1.59 mm and loss tangent 0.02. Overall size of the antenna is 40×40 mm^2 and it is suitable for IEEE Bluetooth/wireless local area network (WLAN), WiMAX and wireless fidelity (Wi-Fi) communication applications.

A multiband CPW-fed slot antenna with fractal stub and parasitic line is proposed by Hongnara *et al*. (2012). The conventional wideband slot antenna with a fractal stub is modified to obtain multiband operation by inserting the parasitic line, resulting in the dual harmonic notched frequency in wideband operation. The antenna has an overall dimension of 10×25 mm^2 and is fabricated on a substrate of relative permittivity 4.2 and thickness 0.8 mm.

Oraizi and Hedayati (2014) developed a CPW-fed slot antenna using Giusepe Peano fractal for multiband applications. The antenna is fabricated on a substrate of relative permittivity 4.4 and thickness 1.6 mm and has an overall size of 33.5×26.5 mm^2. The fractal pattern in the slot increases the electrical length of the antenna without increase in the overall area occupied by the antenna. The antenna is suitable for WLAN and WiMAX applications and covers the bands from 2.9-3.3 GHz, 3.8-5.1 GHz and a wideband 5.8-8.5 GHz.

From the review carried out on the various fractal antennas proposed in existing literature, it is seen that fractals offer a distinct advantage in developing compact antennas for multiband transmission. Also, taking into consideration the advantages

offered by CPW-feeding technique, a planar fractal antenna is developed for multiband operation suitable for GSM, IMT advanced system and upper WLAN applications. The fractal pattern is developed using a combination of self-similarity and space filling techniques.

3.1 ANTENNA GEOMETRY

The evolution of the proposed CPW-fed fractal multiband antenna is shown in Fig.3.1. The simple circular monopole has a very wideband radiation characteristic and its lowest frequency of operation is determined by the diameter of the monopole. Inscribing a hexagon within the monopole forms the iteration 0 structure as shown in Fig. 3.1 (b).

| (a) | (b) | (c) | (d) |
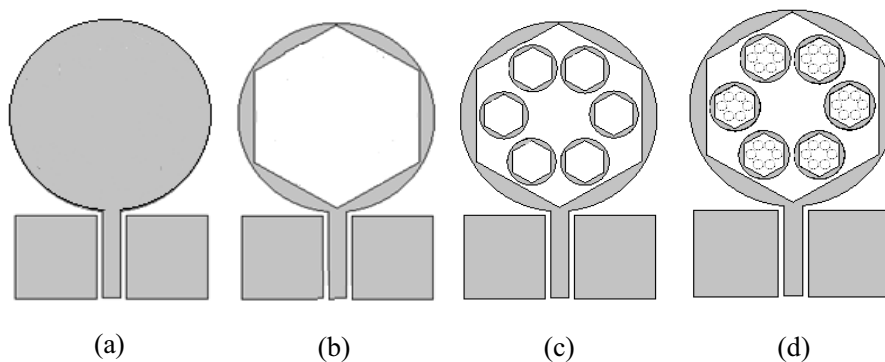
Fig. 3.1   Evolution of the CPW-fed fractal multiband antenna geometry (a) Simple circular monopole (b) Iteration 0 (c) Iteration 1 (d) Iteration 2

Iteration 1 structure results in dual-band operation suitable for GSM and IMT advanced system applications. Due to the hexagonal slot, the current is forced to flow along a longer path created by the perimeter of the slot. This lowers the frequency of operation of the monopole without an increase in its physical size. The diameter of the circle with

inscribed hexagon is then scaled down and six such structures are arranged in a hexagonal manner to form a fractal pattern as shown in Fig. 3.1 (c) in the configuration of iteration 1. This results in the second band shifting to lower frequencies and an additional band close to WLAN frequency. Thus a total of three 2:1 VSWR bands are obtained. Now within each smaller hexagon, the pattern is repeated to obtain the structure of iteration 2. The results obtained with the iteration 2 structure did not vary significantly from that of iteration 1 structure. Also, due to fabrication difficulties, this configuration is not considered further. Fig. 3.2 shows a plot of S_{11} for the different iterations with optimal dimensions as detailed in Section 3.2.
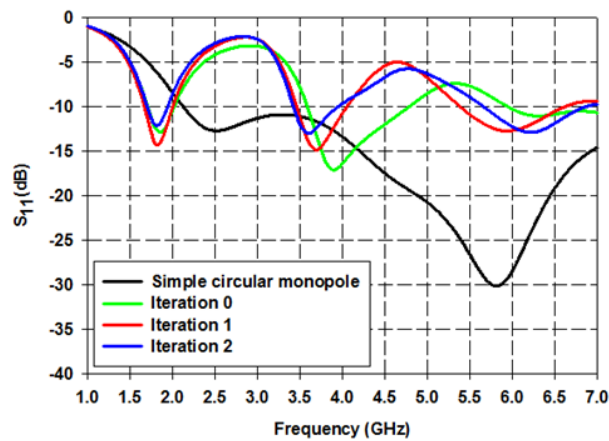
Fig. 3.2   Simulated S_{11} vs frequency of CPW-fed fractal multiband antenna for various iterations with $\epsilon_r = 4.4$, h = 1.6 mm, D = 34 mm, L_g = 17 mm, W_g = 13 mm, W_f = 3 mm, g_1 = 0.3 mm, s = 0.55 mm, g_2 = 0.6 mm, L_h = 16.7 mm, D_i = 8.4 mm and L_{hi} = 3.9 mm

The CPW-feed line is designed for 50 Ω impedance. For a given characteristic impedance, there are several solutions for the geometry of a CPW line. The desired impedance is attained by adjusting the line width, W_f and gap, g_1 dimensions. However, there is a tradeoff between size of the circuitry and the line loss; narrow lines

47

can be quite lossy. Taking into consideration this tradeoff and fabrication limitations, the width and gap dimensions of the CPW feed line are chosen as 3 mm and 0.3 mm respectively. The circular monopole has a diameter D and is spaced from the truncated ground plane of length, L_g and width, W_g by a gap, s. The antenna is designed to support GSM (1.71-1.98 GHz), IMT advanced system for 4G mobile communication (3.4-4.2 GHz) and upper WLAN (5.725-5.875 GHz) bands. The geometry is shown in Fig. 3.3.
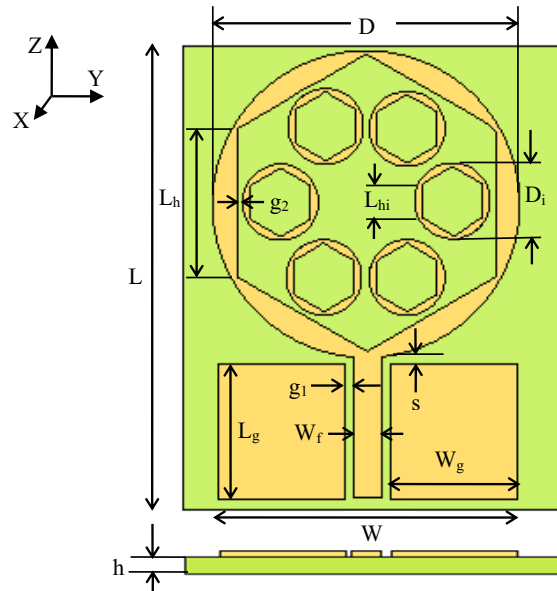
Fig. 3.3   Geometry of CPW-fed fractal multiband antenna with optimized dimensions W = 34 mm, L = 51.3 mm, D = 34 mm, L_g = 17 mm, W_g = 13 mm, W_f = 3 mm, g_1 = 0.3 mm, s = 0.55 mm, g_2 = 0.6 mm, L_h = 16.7 mm, D_i = 8.4 mm and L_{hi} = 3.9 mm for ϵ_r = 4.4, h = 1.6 mm

The antenna is printed on a substrate of thickness h = 1.6 mm, relative permittivity ϵ_r = 4.4 and loss tangent tan δ = 0.02 and has an overall size of 34×51.3 mm². For the optimized dimensions, the simulated reflection characteristics show that the antenna

exhibits triple-band operation from 1.63-1.98 GHz, 3.46-4.05 GHz and 5.38-6.58 GHz. This makes the antenna suitable for GSM, IMT advanced system and upper WLAN applications respectively.

3.2 PARAMETRIC ANALYSIS OF CPW-FED FRACTAL MULTIBAND ANTENNA

To gain insight on how the various dimensions of the antenna determine its performance, a thorough parametric analysis is carried out at various iteration stages. Dimensions are optimized at each stage to finally develop a triple-band antenna suitable for the intended application bands.

3.2.1 Optimization of Simple Circular Monopole for Wideband Response

A CPW-fed circular monopole can exhibit an extremely wide -10 dB bandwidth. The first resonant frequency is predominantly determined by the diameter of the disc. The diameter approximately corresponds to the quarter-wavelength at the resonant frequency (Liang, 2006). Also, the optimal feed gap, s is found to be same as the CPW line gap, g_1. This is because this dimension ensures a smooth transition from the feed line to the monopole. In accordance with this relationship, a circular monopole is designed for a resonance frequency of 2.45 GHz. From the current distributions, it is established that the performance of the antenna is almost independent of the length of the ground plane. However, a variation in the ground plane width shifts all the resonance modes across the spectrum.

Effect of ground plane width, W_g

A parametric analysis on the ground plane width of a simple circular monopole of diameter D = 21 mm corresponding to 2.45 GHz resonance frequency is shown in Fig. 3.4.
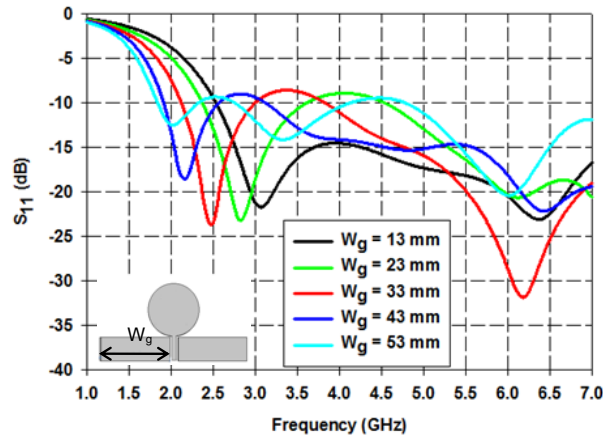
Fig. 3.4   Simulated S_{11} vs frequency of simple circular monopole structure for varying W_g with ϵ_r = 4.4, h = 1.6 mm, L_g = 17 mm, W_f = 3 mm, g_1 = 0.3 mm, s = 0.3 mm and D = 21 mm

It is seen that to obtain the desired resonance, the width of the ground plane on either side of the feed line should be around 33 mm. Thus, the overall size of the antenna becomes 69.6× 38.3 mm². However, the antenna should be integrated in the system circuit board of a communication device. The limited space of the circuit board imposes a constraint on the size of the antenna and its ground plane.

To make the antenna more compact, width of the ground plane, W_g can be reduced. Since it is observed that this causes a shifting of the operating band to higher frequencies, the diameter of the monopole, D is increased as detailed next.

Effect of diameter, D of circular monopole

Compact monopole antennas can be designed on truncated ground planes with the additional advantage of broadband behavior. To make the antenna more compact, the diameter of the monopole is increased while using a smaller ground plane width. The ground plane dimensions are selected as the optimized values $L_g = 17$ mm and $W_g = 13$ mm (Shameena, 2012) for wideband operation. These dimensions correspond to $0.566\lambda_c$ and $0.433\lambda_c$ respectively where λ_c is the guide wavelength at center of the UWB operating range. The parametric analysis on diameter of the monopole with this truncated ground plane is shown in Fig. 3.5.
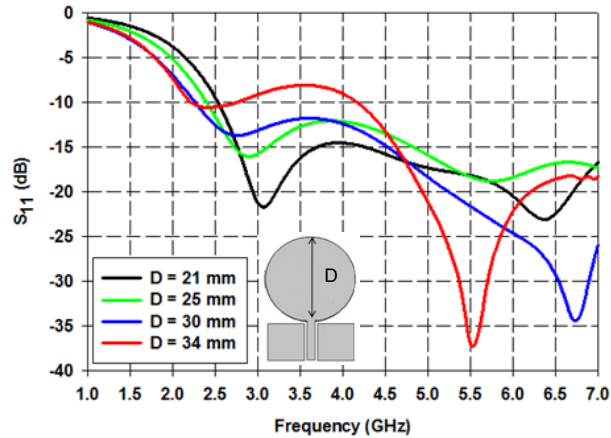
Fig. 3.5   Simulated S_{11} vs frequency of simple circular monopole structure for varying D with $\epsilon_r = 4.4$, h = 1.6 mm, $L_g = 17$ mm, $W_g = 13$ mm, $W_f = 3$ mm, $g_1 = 0.3$ mm and s = 0.3 mm

For a diameter D = 21 mm which corresponds to quarter-wavelength of 2.45 GHz, the monopole with truncated ground yields the first resonance at 3 GHz. As diameter of the monopole is increased, the resonance shifts to lower frequency side and at D = 34 mm, the first resonance is obtained at the desired 2.45 GHz. For this dimension of

51

monopole and truncated ground, the overall antenna size is 34×51 mm^2. This structure has significantly less area compared to the structure without truncated ground.

Effect of spacing between monopole and ground plane, s

The spacing between the monopole and ground plane plays an important role in impedance matching of antenna, especially at higher frequencies. To determine the optimum required spacing for the truncated ground structure, a parametric analysis is carried out as shown in Fig. 3.6.
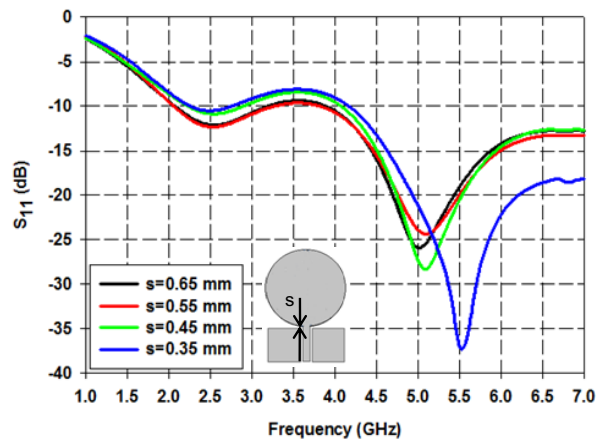
Fig. 3.6   Simulated S_{11} vs frequency of simple circular monopole structure for varying s with $\epsilon_r = 4.4$, h = 1.6 mm, $L_g = 17$ mm, $W_g = 13$ mm, $W_f = 3$ mm, $g_1 = 0.3$ mm and D = 34 mm

As spacing between the monopole and ground plane is increased, impedance matching improves and for s = 0.55 mm $S_{11} \leq$ -10 dB throughout the operating band. This corresponds to $0.017\lambda_c$, where λ_c is guide wavelength corresponding to center of the ultrawide operating range from 2.45 GHz.

With the monopole optimized for wideband response, a hexagonal slot of side L_h is inserted to obtain a dual-band response. The optimization of this structure is discussed next.

3.2.2 Optimization of Iteration 0 Structure for Dual-band Response

The parametric analysis of L_h for the structure of iteration 0 is shown in Fig. 3.7. All other dimensions are the optimized values for wideband response for the simple circular monopole.
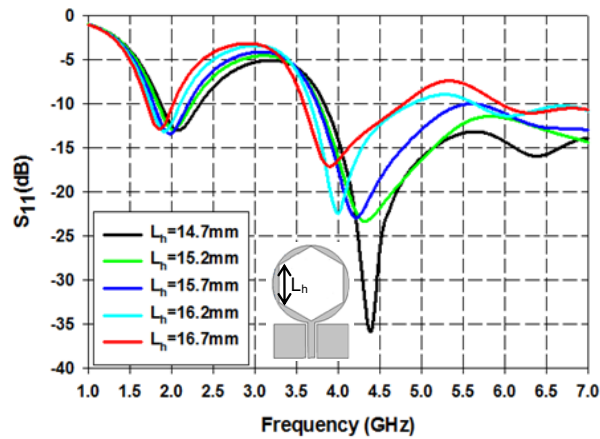
Fig. 3.7   Simulated S_{11} vs frequency of CPW-fed fractal multiband antenna Iteration 0 structure for varying L_h with $\epsilon_r = 4.4$, h = 1.6 mm, $L_g = 17$ mm, $W_g = 13$ mm, $W_f = 3$ mm, $g_1 = 0.3$ mm, s = 0.55 mm, D = 34 mm

As L_h is increased, the perimeter of the hexagon increases and the two resonances shift to the lower frequency side. Also, the bandwidth of the second resonance band decreases. This is because the current on the outer edge of the circular monopole, which is primarily responsible for wideband characteristic, is perturbed. For the chosen monopole of 17 mm radius (D = 34 mm), the side length of the hexagon cannot be

increased beyond 16.7 mm due to a fabrication tolerance of 0.3 mm. Thus, the iteration 0 geometry with $L_h = 16.7$ mm offers two resonant bands. The first resonant band (1.63-2.07 GHz) supports GSM application and the second band (3.58-4.8 GHz) covers the IMT advanced system for 4G mobile communication application band. This optimized iteration 0 geometry is further modified by introducing the fractal pattern to obtain triple-band response as explained below.

3.2.3 Optimization of Iteration 1 Structure for Triple-band Response

Effect of fractal scaling factor, F

The fractal scaling factor $F = \frac{D_i}{D} = \frac{L_{hi}}{L_h}$ for iteration 1 structure is optimized by a parametric analysis of dimensions of the inner circles. The simulated S_{11} results with different scaling factors are shown in Fig. 3.8.
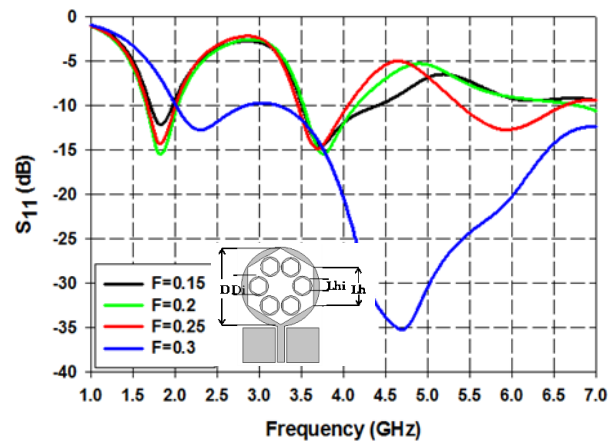
Fig. 3.8   Simulated S_{11} vs frequency of CPW-fed fractal multiband antenna for different fractal scaling factors F with $\epsilon_r = 4.4$, h = 1.6 mm, $L_g = 17$ mm, $W_g = 13$ mm, $W_f = 3$ mm, $g_1 = 0.3$ mm, s = 0.55 mm, $g_2 = 0.6$ mm, D = 34 mm, $L_h = 16.7$ mm

It is seen that for fractal scaling factor F of 0.3 and greater, the structure exhibits very wideband characteristics. This is because the inner circles merge with the sides of the hexagon of iteration 0 structure and the antenna behaves as a simple circular monopole. For a scaling factor of 0.25, triple-band behavior is observed with a lowering in the bandwidth of second band of the structure of iteration 0. Triple-band behavior suitable for GSM, IMT advanced system for 4G mobile communication systems and upper WLAN is obtained for optimum fractal scaling factor $F = 0.25$ which results in $D_i = 8.4$ mm and $L_{hi} = 3.9$ mm.

Effect of gap between inner circles and hexagonal slot side, g_2

The effect of varying the gap g_2 between the inner circles of iteration 1 structure and adjacent edges of hexagonal slot of iteration 0 structure is shown in Fig. 3.9.
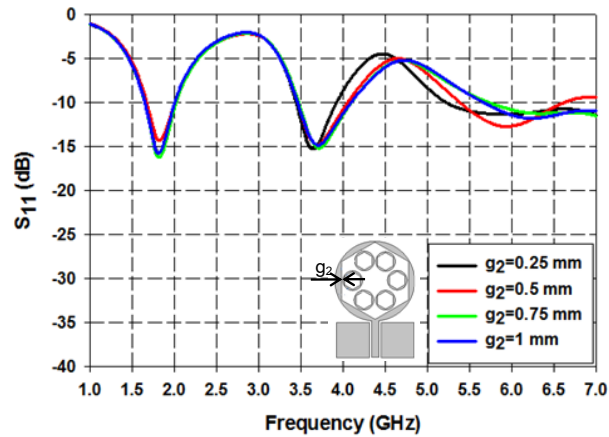
Fig. 3.9   Simulated S_{11} vs frequency of CPW-fed fractal multiband antenna for varying g_2 with $\epsilon_r = 4.4$, h = 1.6 mm, $L_g = 17$ mm, $W_g = 13$ mm, $W_f = 3$ mm, $g_1 = 0.3$ mm, s = 0.55 mm, D = 34 mm, $L_h = 16.7$ mm, $L_{hi} = 3.9$ mm, $D_i = 8.4$ mm (for F = 0.25)

55

The gap variation does not have much effect on the first resonance. However, there is a change in the bandwidth of second and third resonance band. As the gap decreases, impedance bandwidth decreases in second band and increases in third band. This could be due to variation in coupling from outer monopole edge to inner circles as well as mutual coupling between the inner circles. From the exhaustive simulation, g_2 is optimized as 0.5 mm so that second and third bands cover the intended application frequencies. This corresponds to $0.014\lambda_{g3}$ where λ_{g3} is the guide wavelength at third resonance.

3.3 SURFACE CURRENT DISTRIBUTION OF CPW-FED FRACTAL MULTIBAND ANTENNA

The surface current distribution of the antenna at the three resonance frequencies is shown in Fig. 3.10.
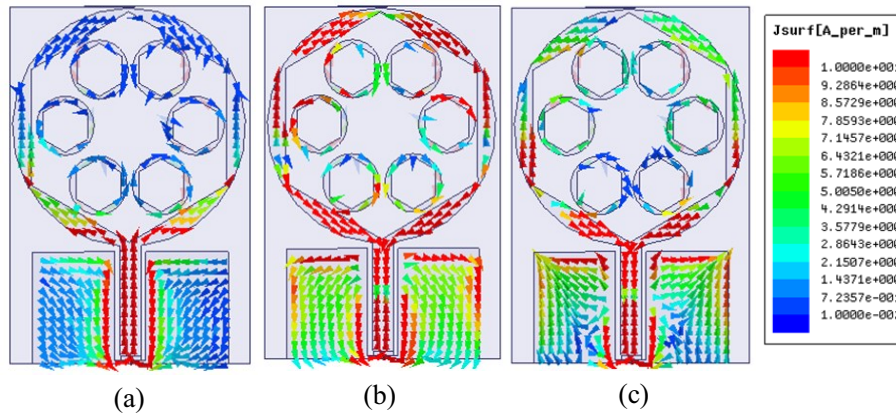
Fig. 3.10   Simulated surface current distribution of CPW-fed fractal multiband antenna at resonance frequencies (a) 1.8 GHz (b) 3.8 GHz (c) 5.8 GHz with ϵ_r = 4.4, h = 1.6 mm, D = 34 mm, L_g = 17 mm, W_g = 13 mm, W_f = 3 mm, g_1 = 0.3 mm, s = 0.55 mm, g_2 = 0.5 mm, L_h = 16.7 mm, D_i = 8.4 mm and L_{hi} = 3.9 mm (for F = 0.25)

56

At the first resonance, a full wave variation in current is seen along the perimeter of the hexagon. This confirms that the first band can be designed based on the side of the hexagon L_h. The current distribution on the inner circles indicates that they have minimal effect on the first resonance band. At the second resonance, there is a variation in current on the upper and middle inner circles which shows an increased coupling of energy between monopole and inner circles. This results in the shifting in resonance of the second band to the lower side when the structure is iterated to iteration 1, as seen in Fig. 3.2. At the third resonance, current variation is seen on all the inner circles and also along the length and width of the ground plane.

3.4 DESIGN EQUATIONS OF CPW-FED FRACTAL MULTIBAND ANTENNA

Based on the parametric analysis it is seen that each resonance is controlled by a different set of antenna parameters. Accordingly, the design equations for the triple-band antenna are formulated. The step by step procedure for designing the antenna is as follows:

1) Design a 50 Ω CPW line of width, W_f and gap, g_1 on a substrate with relative permittivity ϵ_r (Garg *et al*., 2001). Calculate effective permittivity of the substrate ϵ_{reff} using $\epsilon_{\text{reff}} = (\epsilon_r + 2) / 3$.

2) The length of the ground plane on either side of the feed line is calculated using

$$L_g = 0.566\lambda_c \tag{3.1}$$

where λ_c is the guide wavelength corresponding to center frequency of the UWB operating range.

3) The width of the ground plane on either side of the feed line is calculated using

$$W_g = 0.433\lambda_c \tag{3.2}$$

57

4) Design a circular monopole of diameter

$$D = 0.405\lambda_m \tag{3.3}$$

where λ_m is the guide wavelength corresponding to the average frequency, f_m of desired lower resonance frequency and UWB lower limit.

5) The gap between monopole and ground, s is set using

$$s = 0.017\lambda_{c\prime} \tag{3.4}$$

where $\lambda_{c\cdot}$ is the guide wavelength corresponding to center of ultra wide operating range from f_m.

6) Design the hexagonal slot side length using the regression equation

$$L_h = -5.33f_1 - 0.85\epsilon_r - 0.558h + 30.987 \tag{3.5}$$

where f_1 is the frequency in GHz corresponding to the first resonance. This equation is valid for substrates with $2.2 < \epsilon_r < 6.15$ and 0.8 mm $< h < 2$ mm for frequency range 1.6 GHz $< f_1 < 2.2$ GHz.

7) The inner circles that form the fractal pattern are designed using fractal scaling factor

$$F = \frac{D_i}{D} = \frac{L_{hi}}{L_h} = 0.25 \tag{3.6}$$

8) Spacing between inner circles and hexagonal slot side is calculated as

$$g_2 = 0.014\lambda_{g3} \tag{3.7}$$

where λ_{g3} is the guide wavelength corresponding to the third resonance.

To validate the design equations, the antenna dimensions to obtain three resonance frequencies 1.8 GHz, 3.8 GHz and 5.8 GHz are computed for different substrates as shown in Table 3.1. The simulated reflection characteristics obtained for the antennas so designed on different substrates are shown in Fig. 3.11.

Table 3.1 CPW-fed fractal multiband antenna parameters for
different substrates obtained from design equations

Parameter (mm)	Substrate			
	1	2	3	4
	Rogers 5880 $\epsilon_r = 2.2$	Rogers RO4003 $\epsilon_r = 3.55$	FR-4 Epoxy $\epsilon_r = 4.4$	Rogers RO3006 $\epsilon_r = 6.15$
h	1.57	0.8	1.6	1.28
W_f	4	6	3	2.58
g_1	0.17	0.3	0.3	0.45
L_g	21	18.2	16.98	15.03
W_g	16.03	13.94	13	11.49
L_h	18.65	17.9	16.7	15.45
D	41.9	36.5	33.9	31
s	0.66	0.57	0.53	0.47
D_i	10.5	9.1	8.5	7.75
L_{hi}	4.4	4.25	3.9	3.63
g_2	0.61	0.53	0.49	0.44
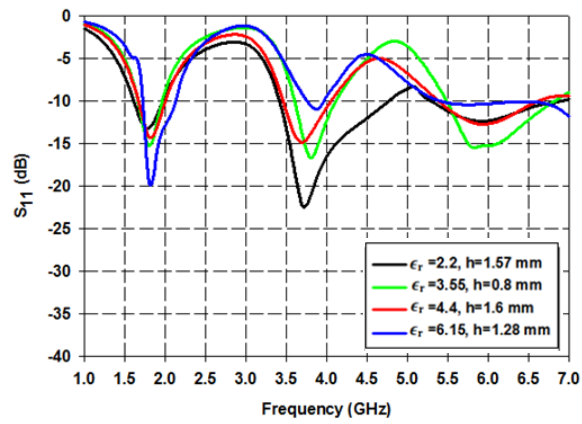
Fig. 3.11   Simulated reflection characteristics of CPW-fed fractal
multiband antenna on different substrates

On all the substrates, the designed antenna resonances are in reasonably good agreement with desired results which ensures repeatability of the proposed design. The resonances obtained by simulation are compared with the desired resonances and percentage error is shown in Table. 3.2. On all substrates, the design results in triple-band operation for similar frequency ranges with a maximum error less than 3 %.

Table 3.2   % Error in simulated frequency of CPW-fed fractal multiband antenna for different dielectric substrates at f_1 = 1.8 GHz, f_2 = 3.8 GHz and f_3 = 5.8 GHz

Substrate	Simulated Frequency (GHz)			Error (%)		
	f_1	f_2	f_3	f_1	f_2	f_3
Rogers 5880 (ϵ_r = 2.2, h = 1.57 mm)	1.77	3.71	5.89	1.6	2.3	1.5
Rogers RO4003 (ϵ_r = 3.55, h = 0.8 mm)	1.79	3.79	5.82	0.55	0.26	0.34
FR-4 Epoxy (ϵ_r = 4.4, h = 1.6 mm)	1.82	3.7	5.91	1.11	2.63	1.86
Rogers RO3006 (ϵ_r = 6.15, h = 1.28 mm)	1.81	3.86	5.72	0.55	1.5	1.37

3.5   REFLECTION CHARACTERISTICS OF CPW-FED FRACTAL MULTIBAND ANTENNA

The antenna is fabricated on a substrate of thickness 1.6 mm and permittivity 4.4 with optimized dimensions as shown in Fig. 3.12 (a). Measurements are carried out using Agilent PNA E8362B. The reflection characteristics show fairly good agreement as seen in Fig. 3.12 (b).
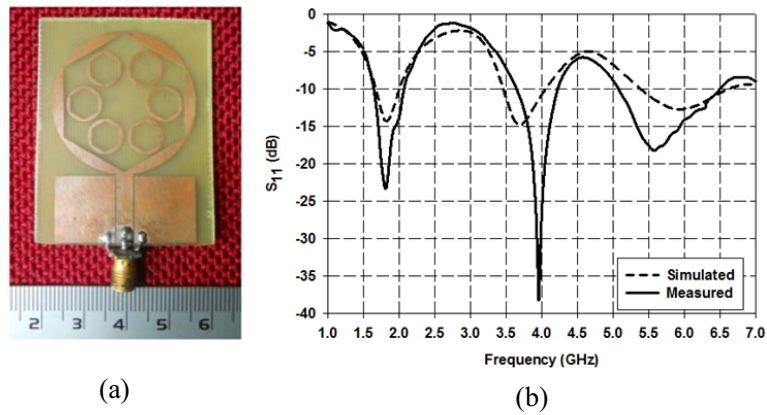
Fig. 3.12   (a) Fabricated prototype (b) Simulated and measured reflection characteristics of the CPW-fed fractal multiband antenna with $\epsilon_r = 4.4$, $h = 1.6$ mm, $D = 34$ mm, $L_g = 17$ mm, $W_g = 13$ mm, $W_f = 3$ mm, $g_1 = 0.3$ mm, $s = 0.55$ mm, $g_2 = 0.5$ mm, $L_h = 16.7$ mm, $D_i = 8.4$ mm and $L_{hi} = 3.9$ mm (for $F = 0.25$)

Simulated and measured results show similar behaviour and desired triple-band characteristics are obtained.

At higher frequencies, the measured and simulated results show some difference. This may be due to uncertainty in thickness and/or dielectric constant of substrate and soldering effects of the sub miniature version A (SMA) connector, which have been neglected in the simulations. But the structure still exhibits triple-band behaviour as observed in simulated results. The measured bandwidths are from 1.63 - 2.07 GHz, 3.63 - 4.22 GHz and 5.08 - 6.48 GHz for $S_{11} \leq -10$ dB.

3.6 RADIATION PATTERN OF CPW-FED FRACTAL MULTIBAND ANTENNA

The simulated 3D radiation pattern of the antenna at the resonance frequencies is plotted in Fig. 3.13. As is seen in the current distribution of Fig. 3.10, the first

61

resonance is due to perimeter of the hexagon alone and there is negligible contribution of the ground plane. This results in a doughnut shaped pattern which is typical of a dipole antenna.

(a)　　　　　　(b)　　　　　　(c)
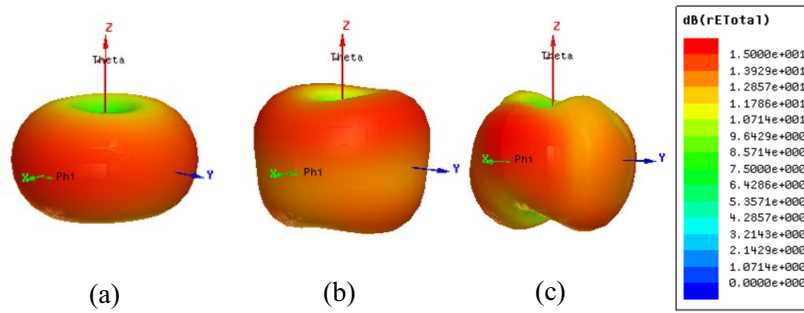
Fig. 3.13　Simulated 3D radiation patterns of the CPW-fed fractal multiband antenna at the three resonance frequencies (a) 1.8 GHz (b) 3.8 GHz (c) 5.8 GHz with $\epsilon_r = 4.4$, h = 1.6 mm, D = 34 mm, L_g = 17 mm, W_g = 13 mm, W_f = 3 mm, g_1 = 0.3 mm, s = 0.55 mm, g_2 = 0.5 mm, L_h = 16.7 mm, D_i = 8.4 mm and L_{hi} = 3.9 mm (for F = 0.25)

At the second resonance, the current distribution along the perimeter of the hexagon resembles a second order harmonic. Thus the pattern changes its shape to a slightly pinched doughnut with a radiation increase along $\theta = 45º$ as shown in Figure 3.13 (b). At the third resonance, current distribution along the perimeter of the hexagon corresponds to a higher order mode. There is a current variation on the lower and middle inner circles which also causes radiation. Due to the combined effect a slight degradation is seen in the radiation pattern.

Measured radiation patterns of the antenna at the resonances observed during testing are plotted in Fig. 3.14.
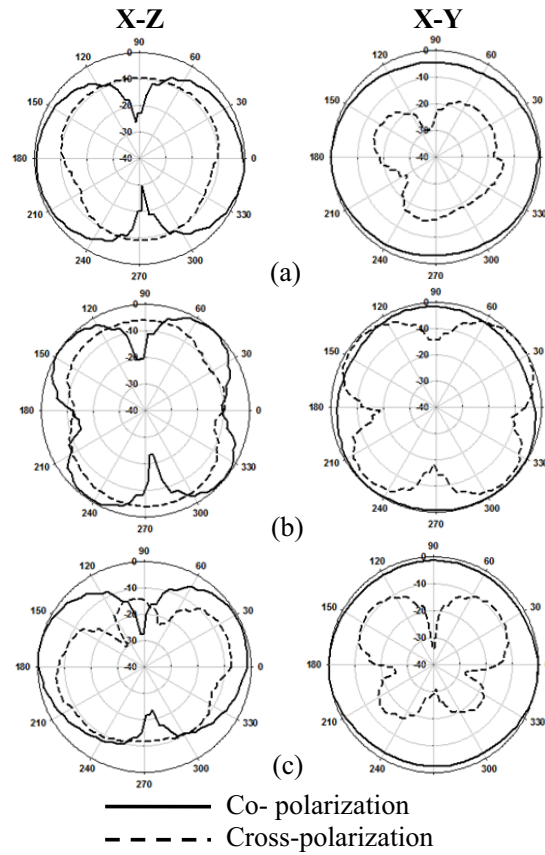
Fig. 3.14   Normalized 2D radiation pattern of the CPW-fed fractal multiband antenna measured at (a) 1.8 GHz (b) 3.8 GHz (c) 5.8 GHz with $\epsilon_r = 4.4$, h = 1.6 mm, D = 34 mm, L_g = 17 mm, W_g = 13 mm, W_f = 3 mm, g_1 = 0.3 mm, s = 0.55 mm, g_2 = 0.5 mm, L_h = 16.7 mm, D_i = 8.4 mm and L_{hi} = 3.9 mm (for F = 0.25)

Normalized patterns of the antenna are plotted in two principal planes. The antenna has a figure-8 pattern in the E-plane (X-Z). In the H-plane (X-Y) the pattern is non-directional in all the frequency bands of interest like that of an ordinary dipole antenna. The radiation patterns show good cross polarization levels at the first and third resonance. At the second resonance however, the antenna exhibits poor cross

polarization which could be attributed to the second harmonic characteristics seen at this resonance.

3.7 GAIN AND EFFICIENCY OF CPW-FED FRACTAL MULTIBAND ANTENNA

The antenna gain and efficiency are measured and the results are shown in Fig. 3.15.

(a)   (b)
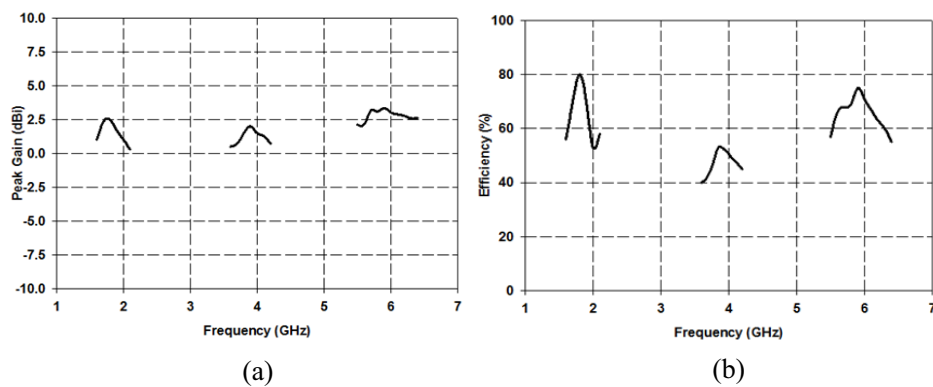
Fig. 3.15   (a) Peak gain and (b) Efficiency of CPW-fed fractal multiband antenna with ϵ_r = 4.4, h = 1.6 mm, D = 34 mm, L_g = 17 mm, W_g = 13 mm, W_f = 3 mm, g_1 = 0.3 mm, s = 0.55 mm, g_2 = 0.5 mm, L_h = 16.7 mm, D_i = 8.4 mm and L_{hi} = 3.9 mm (for F = 0.25)

The antenna has a peak gain of 2.51 dBi in the first band, 2.45 dBi in the second band and 2.67 dBi in the third band. The efficiency plot shows a similar variation as the gain values with a maximum of 78 %, 52 % and 76 % in the three bands respectively.

3.8 CHAPTER SUMMARY

This chapter presents a CPW-fed fractal antenna design for triple-band applications. The overall antenna size is 34×51.3 mm^2 on a substrate of relative permittivity 4.4 and

thickness 1.6 mm. The operating bands are 1.63-2.07 GHz, 3.63-4.22 GHz and 5.08-6.48 GHz which makes the antenna suitable for GSM, IMT advanced system for 4G mobile communication systems and upper WLAN applications. The results of the proposed antenna were published initially, however further optimization led to better results which are presented in this chapter. The antenna is compared with some of the recently proposed multiband fractal antennas as shown in Table 3.3.

Table 3.3   Comparison of proposed antenna with existing multiband fractal antennas

Antenna	No. of operating bands	Lowest operating frequency	Size(mm³)	ϵ_r	Peak Gain
Mirkamali *et al*. (2010)	5	0.89 GHz	43×43×0.8 Ground plane- 15 cm×15 cm	4.4	1.9-7.1 dBi
Aziz *et al*. (2011)	4	0.88 GHz	62×89.6×0.78	4.7	1-4 dBi
Hongnara *et al*. (2012)	3	1.67 GHz	48×50×0.8	4.2	1-3.5 dBi
Oraizi and Hedayati (2014)	3	2.9 GHz	26.5×33.5×1.6	4.4	3-5 dBi
Kumar *et al*. (2014)	3	2.33 GHz	50×50×3.34	2.2/ 4.4	6.33- 8.68 dBi
Proposed antenna	3	1.63 GHz	34×51.3×1.6	4.4	2.45- 2.67 dBi

In the antenna proposed by Mirkamali *et al*. (2010), higher number of operating bands with a much lower operating frequency is reported. The antenna monopole is also compact; however, a very large ground plane is required. The antenna by Aziz *et al*. (2011) also has a higher number of operating bands with a much lower operating

frequency for the first resonance, but the antenna size is much larger compared to the proposed structure. The performance of the antenna by Hongnara *et al*. (2012) is quite similar to the proposed antenna but is of larger size. Three operating bands are achieved in the antenna by Oraizi and Hedayati (2014), and the antenna size is smaller than the proposed geometry. However, the lowest operating frequency is much higher for this antenna. The antenna proposed by Kumar *et al*. (2014), has much higher gain than the proposed antenna. However, a stacked design involving two types of substrates with an air gap in between is used which makes the antenna very bulky. Hence on comparison with some of the antennas developed on substrates with similar relative permittivity, it is seen that the proposed antenna has a compact size and appreciable gain. The antenna is thus suitable for multiband wireless applications in handheld devices.

The objective was to develop a multiband antenna incorporating UWB applications. Multiband behavior is achieved by inserting a hexagonal slot in a circular monopole and then creating a fractal pattern. However, on introducing the hexagonal slot, UWB characteristics of the circular monopole degraded. To achieve lower bands of operation while retaining UWB characteristics, the shape of the hexagonal slot is modified to create a new design as proposed in Chapter 4.

Chapter 4

CPW-FED SLOTTED MULTIBAND ANTENNAS

Conventionally, a planar slot antenna comprises of a slot in the ground plane of a microstrip line such that the slot is perpendicular to the strip conductor of the microstrip line. The slot can have any shape and like microstrip patch antennas, they can also be fed by a coplanar waveguide (Pell *et al*., 2008; Angleopoulos *et al*., 2006; Eldek *et al*., 2005). The slot width and feed structure affect the impedance bandwidth of the antenna. Wider slots have more bandwidth and an optimum feed structure gives good impedance matching.

Slots are commonly used for band-notched UWB antenna design. These slots can be embedded either in the monopole or in the ground plane. Several slot shapes have been investigated such as L-shaped (Trang *et al*., 2011), Ring-shaped (Kumar *et al*., 2011), U or C-shaped (Deng *et al*., 2012; Trang *et al*., 2011; Yu and Wang, 2009), T-shaped (Zhang *et al*., 2009), capacitive loaded loop (CLL) (Lin and Ziolkowski, 2010), complementary split ring resonator (CSRR) (Liu *et al*., 2008; Awad and Abdelazeez, 2013) etc. These are narrow slots with an overall length of $\lambda_n/4$ where λ_n is the wavelength of the notched frequency. The slot design is such that at the notched frequency the currents flowing along the interior and exterior edges of the slot are in opposite directions (Dong *et al*., 2014). By using a wide slot in the monopole, the current path can be altered to produce a resonance in addition to the resonance produced by the monopole. The slot perimeter controls the resonance and this approach is used for the design of two multiband antennas in this chapter.

Several research articles have been published using this technique and a review of such work is presented here.

Kim and Yook (2005) proposed a coplanar waveguide (CPW)-fed meander slot antenna for multiband applications. A non-uniform slot width is used and by increasing the meander sections, frequency of operation is lowered without increase in overall physical size of the antenna. The antenna is fabricated on a Teflon substrate of relative permittivity 2.3 and thickness 0.508 mm. The technique adopted results in 92 % size reduction compared to a conventional rectangular microstrip antenna.

A CPW-fed monopole antenna with slots embedded for global system for mobile (GSM), wireless local area network (WLAN) and worldwide interoperability for microwave access (WiMAX) operation is proposed by Wang and Yang (2014). The antenna is fabricated on a substrate of relative permittivity 4.4 and has an overall size of 47×44 mm^2. The slots redistribute the surface current which results in the various operating bands.

Zhang *et al*. (2012a) proposed a microstrip fed triple-band antenna for WiMAX and WLAN applications using an E-shaped and a C-shaped slot embedded in a rectangular monopole. The antenna has a size of 30×25 mm^2 on a substrate of relative permittivity 2.65 and thickness 1 mm. The inverted E-shaped slot controls the bands 2.4–2.484 GHz and 3.4–3.69 GHz, while the inverted C-shaped slot controls the bands 3.4 GHz–3.69 GHz and 5.15–5.825 GHz.

Elsheakh and Abdallah (2012) proposed a CPW-fed L-loaded PIFA in which multiband behavior is achieved by loading folded slots on the CPW-feed line. The proposed antenna is suitable for use in GSM 850/900, LTE, ISM 2.45 GHz, WiMAX bands at 3.5 GHz and 5.7 GHz, WLAN 5.2 GHz and other wireless communication applications. The antenna is fabricated on a substrate of size 38×43 mm^2.

Wang *et al*. (2011) proposed a multiband antenna using square nested loops. The center frequency and the number of operating bands are controlled by the side length of the square-loops and the number of loops respectively. The antenna is fabricated on a substrate of relative permittivity 4.4 and thickness 1.6 mm with size 42×42 mm^2.

A CPW-fed ultrawideband (UWB) antenna using a Koch fractal slot antenna is presented by Zhang *et al*. (2012b). The antenna is fabricated on a substrate of relative permittivity 4.6 and thickness 1.6 mm and is of size 72×72 mm^2. The antenna achieves a -10 dB impedance bandwidth of 1.27-4.67 GHz with a maximum gain variation of 2.1 dBi over the UWB range.

The Sierpinski carpet fractal design is incorporated on a CPW-fed circular monopole antenna for UWB applications by Shahu *et al*. (2013). The antenna is designed on RT/Duroid 5880 substrate with thickness of 1.57 mm and relative permittivity of 2.2 having loss tangent 0.0009 and has an overall size of 37×46 mm^2. Operating bands for VSWR < 2 and S_{11}< -10 dB are from 3.1-11 GHz with a maximum gain variation of less than 3 dBi over the UWB range.

A CPW-fed UWB antenna with a fractal pattern of triangular slot in a circular monopole is presented by Natarajamani *et al*. (2011). The antenna is printed on a 39.2×43.5 mm^2 substrate of relative permittivity 4.4 and thickness 1.6 mm. Band notch characteristics for WiMAX and WLAN bands are achieved by inserting L shaped slots in the ground plane and hook shaped slits above the monopole. Simulated and measured readings are in good agreement; however, group delay is very high at upper UWB frequencies.

Jahromi *et al*. (2011) presented a Sierpinski carpet fractal monopole antenna with grounded coplanar waveguide to obtain wideband characteristics. The fractal monopole using conventional feed is compared with the grounded CPW-fed monopole. Fabrication is carried out on a Rogers RO4003 substrate thickness 1.5 mm, relative permittivity 3.38 and a loss tangent about 0.0027. Both antennas use the same square ground plane of side length 30 mm and substrate dimensions of 20.4×18 mm^2. While the conventional Sierpinski carpet monopole has an impedance bandwidth from 6.25–8.4 GHz, the modified Sierpinski carpet monopole is matched throughout the 4.65–10.5 GHz band. The gain of the modified Sierpinski carpet monopole is also found to be greater than that of the conventional Sierpinski carpet monopole.

A CPW-fed monopole antenna for quad-band applications is presented by Sujith *et al*. (2011). A modified T-shaped monopole is used to create various current paths to achieve quad-band operation suitable for GSM 900, digital cellular system (DCS) 1800, IEEE 802.11a, IEEE 802.11b and HiperLAN-2 bands. The antenna has a dimension of 32×31 mm^2 on a substrate of relative permittivity 4.4 and thickness 1.6 mm.

A planar inverted-F antenna (PIFA) with multiband resonance is presented by Jegadeesan and Mansouri (2015). Slots and stubs are used in the ground plane to achieve lower resonances in addition to UWB characteristic. The antenna is built on FR-4 substrate with relative permittivity 4.4 and loss tangent 0.02. The substrate height is 1.6 mm and the substrate dimensions are 120×60 mm^2. The top plate size is 45×26 mm^2 and it has a slot with size of 4.5×22 mm^2. The operating bands are 0.8-1.02 GHz, 1.75-2.02 GHz and 2.37-6 GHz with gain of 2-6.5 dBi.

A microstrip fed planar monopole with multiple branches is presented by Liao *et al*. (2010). Four resonant branches on the top surface and one parasitic branch on the back are used to achieve multiband operation. Impedance matching and size reduction are improved by meandered lines and closed loop structures. The antenna has a size 17.5×35.7 mm^2 on a substrate of relative permittivity 4.4 and thickness 0.8 mm.

A CPW-fed antenna with two types of slots for dual-band operation is presented by Liu *et al*. (2010). The embedded slots excite multi-resonant modes for dual-band operation from 2.34-2.55 GHz and 4.8-9.62 GHz with average gain of 1.4 dBi and 5.1 dBi respectively. The antenna has an overall size of 30×25 mm^2 on a substrate of relative permittivity 4.4 and thickness 1.6 mm.

From the literature review carried out on antennas using slots for multiband operation, it is seen that slots can increase the electrical length of an antenna which makes them desirable for miniaturization of design. The self-similarity property of fractals will result in multiple resonances (Nur *et al*., 2011). These multiple resonances can also be converted into wide band characteristics by bringing the resonance frequencies closer

71

and letting the bands overlap. Using this technique, several articles have explored the feasibility of fractal antennas for UWB applications.

Several designs using meandered stubs to develop compact multiband antennas have also been proposed. However, most of the work presented so far use separate antennas for lower bands and UWB applications.

In this chapter, three designs are presented for multiband UWB applications using a CPW-fed circular monopole.

In Type-I design, a slot is inserted in the monopole to attain dual-band operation suitable for GSM and UWB applications. The slot shape is obtained by modifying the hexagonal slot proposed in Chapter 3 to ensure UWB characteristics of the circular monopole are retained.

In Type-II design, a fractal pattern is introduced in the slotted antenna to obtain dual-band characteristics in GSM and UWB bands with improved matching in UWB range.

In Type-III design, a bent monopole is inserted in the space created by the slot of Type-I design. The bent monopole extends the perimeter of the slot which results in a resonance band suitable for wireless medical telemetry service (WMTS) operation. The bent monopole also creates a resonance for universal mobile telecommunication system (UMTS) applications which results in a triple-band antenna.

4.1 DUAL-BAND CIRCULAR MONOPOLE ANTENNA (TYPE-I)

4.1.1 Antenna Geometry

First, the 50 Ω CPW-feed line is designed on the FR-4 substrate. To develop the antenna, a circular monopole that has an inherent wideband characteristic is designed for a resonance frequency of 2.45 GHz using a truncated ground plane. The ground plane length, width and spacing from monopole are optimized for wideband response from 2.45 GHz to cover the entire UWB range. First, a hexagonal slot is inserted in the monopole as described in Chapter 3. Then, the sides of three isosceles triangles are merged with alternate sides of the hexagon. The evolution of the geometry is shown in Fig. 4.1.

| (a) | (b) | (c) |
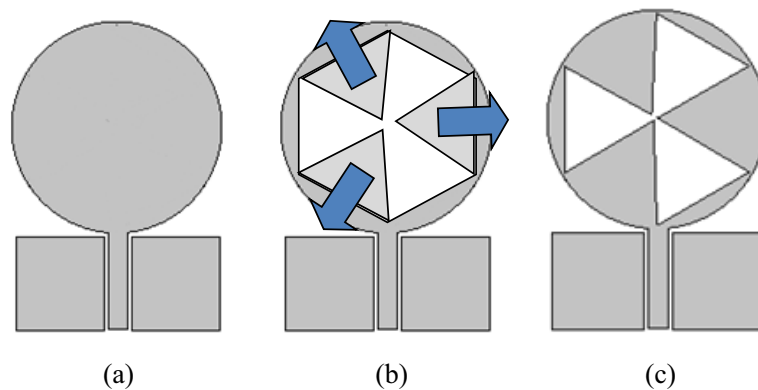
Fig. 4.1   Evolution of the dual-band circular monopole antenna (Type-I) geometry (a) Simple circular monopole (b) Merging triangles with hexagonal slot (c) Proposed antenna

The antenna is fed by a 50 Ω CPW on a substrate of size W×L. The substrate used is of thickness h = 1.6 mm and relative dielectric constant ϵ_r = 4.4 with loss tangent tan δ = 0.02. The CPW-feed line has a width, W_f = 3 mm and is spaced at a distance, g = 0.3

mm from the ground plane of length, L_g and width, W_g on both sides. The circular monopole is of diameter D and is spaced at a distance s from the ground conductor. The vertices of the three triangles used to form the slot shape are separated from each other by g_s and the edges of the slot are of length, L_s. The slot orientation is such that a symmetrical line drawn through its center makes an angle α with respect to the CPW feed line. The slot is introduced to obtain a resonance band for GSM application. The final design layout of the proposed antenna shown in Fig. 4.2 is suitable for dual-band operation in GSM and UWB bands.
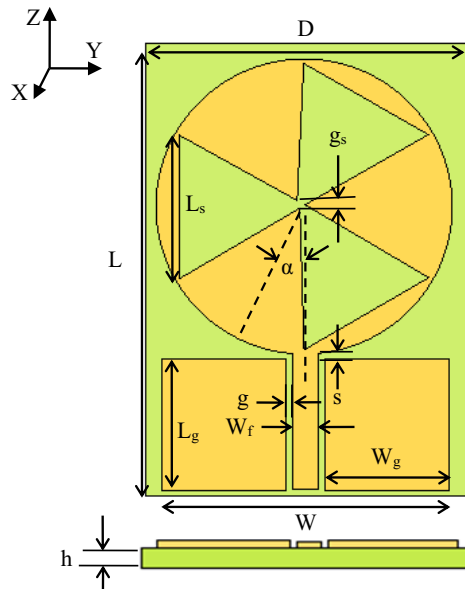
Fig. 4.2   Geometry of dual-band circular monopole antenna (Type-I) with optimized dimensions D = 34 mm, W = 29.6 mm, L = 51 mm, L_s = 16.7 mm, g_s = 1 mm, α = 30⁰, L_g = 17 mm, W_g = 13 mm, W_f = 3 mm, g = 0.3 mm and s = 0.55 mm for ϵ_r = 4.4, h = 1.6 mm

4.1.2 Parametric Analysis of Dual-band Circular Monopole Antenna (Type-I)

To obtain a resonance at GSM band, while retaining wideband response over the UWB range from 3.1-10.6 GHz, the hexagonal slot shape of CPW-fed fractal multiband

antenna design presented in Chapter 3 is modified. A parametric analysis on various slot parameters is carried out to optimize the antenna for operation in both GSM and UWB bands.

Effect of slot side length, L_s

In order to obtain a lower resonance while retaining UWB characteristics, the sides of three isosceles triangles are merged with alternate sides of the hexagonal slot in the structure of CPW-fed fractal multiband antenna. A gap is provided at the center of the slot where the corners of the three triangles meet. The value chosen for the gap is 0.3 mm due to fabrication constraints. Due to the slot, the current is forced to flow along a longer path created by the perimeter of the slot. This results in a dual-band antenna with a lower resonance band suitable for GSM. The lower band is mainly controlled by the perimeter of the slot as shown in the parametric analysis of slot side length, L_s in Fig. 4.3.
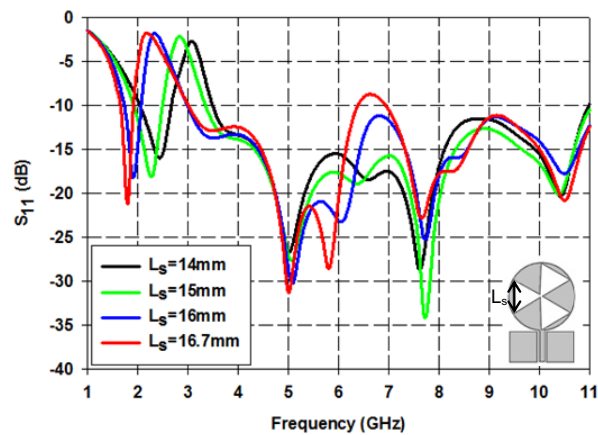
Fig. 4.3   Simulated S_{11} vs frequency of dual-band circular monopole antenna (Type-I) for varying L_s with $\epsilon_r = 4.4$, h = 1.6 mm, $L_g = 17$ mm, $W_g = 13$ mm, $W_f = 3$ mm, g = 0.3 mm, $\alpha = 30^o$, $g_s = 0.3$ mm, s = 0.55 mm and D = 34 mm

75

As slot side length increases, the first resonance frequency as well as the lower limit of the UWB band shifts towards the lower frequencies. This clearly illustrates the effect of overall dimension of the slot on the lower resonance band. L_s is increased towards circular monopole radius 17 mm while maintaining a fabrication tolerance of 0.3 mm. For $L_s = 16.7$ mm, the slot perimeter is approximately 150 mm which corresponds to $1.5\lambda_g$ of the resonance frequency in the GSM band and so this dimension is chosen for slot side length.

Effect of slot gap, g_s

The slot gap, g_s at the center of the slot is varied and the reflection characteristics are shown in Fig. 4.4.
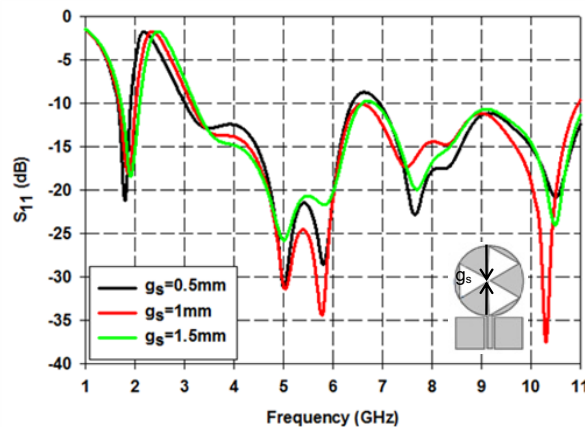
Fig. 4.4   Simulated S_{11} vs frequency of dual-band circular monopole antenna (Type-I) for varying g_s with $\epsilon_r = 4.4$, h = 1.6 mm, D = 34 mm, $L_s = 16.7$ mm, $\alpha = 30^o$, $L_g = 17$ mm, $W_g = 13$ mm, $W_f = 3$ mm, g = 0.3 mm and s = 0.55 mm

As slot gap is increased, better matching is achieved in the UWB range. This is because the gap capacitance counter balances the inductance created by the slot leading to an improvement in impedance matching. However, for increased slot gap, the first

76

resonance and lower frequency limit of the UWB band increases slightly. This could

be due to the decrease in the overall slot perimeter with increase in slot gap. Optimum

results are obtained for g_s = 1 mm which is $0.033\lambda_c$ where λ_c corresponds to the center

frequency of the UWB band.

Effect of slot orientation, α

The slot is introduced in the circular monopole to obtain a lower band while

maintaining impedance matching in the UWB band. For a circular monopole, current

distribution is mainly on the outer edge of the monopole. Hence the orientation of the

slot with respect to the feed line is also an important parameter in determining the

impedance bandwidth of the antenna. To study its effect, the slot with optimized side

length L_s and center gap g_s is rotated and the results are shown in Fig. 4.5.
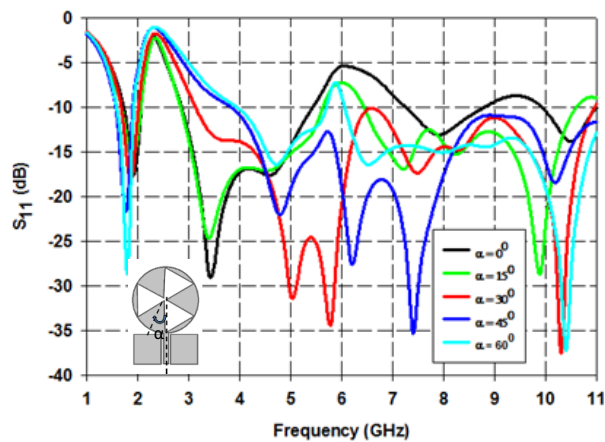
Fig. 4.5   Simulated S_{11} vs frequency of dual-band circular
monopole antenna (Type-I) for varying orientation of slot
with ϵ_r = 4.4, h = 1.6 mm, D = 34 mm, L_s = 16.7 mm, L_g =
17 mm, W_g = 13 mm, W_f = 3 mm, g = 0.3 mm, s = 0.55
mm and g_s = 1 mm

When $\alpha = 0^o$, the slot is symmetrical with respect to the feed line and there is considerable mismatch in the UWB range. As α is increased, matching in the UWB range improves and optimum results are obtained for $\alpha = 30^o$. As α is further increased, the lower frequency limit of the UWB band increases.

When $\alpha = 60^o$, which is also an orientation in which the slot is symmetrical with respect to feed line, impedance matching in the UWB range again decreases. This is because the slot corners that get aligned near the feed line create relatively more perturbation to the current on the outer edge of the circular monopole. This causes impedance mismatch in the UWB range.

The first resonance however remains unchanged for all orientations because slot dimensions remain unchanged.

4.1.3 Surface Current Distribution of Dual-band Circular Monopole Antenna (Type-I)

The current distribution on the surface of the antenna is simulated at various operating frequencies and shown in Fig. 4.6.

At the first resonance, the current is mainly concentrated along the edges of the slot which clearly reveals that the perimeter of the slot controls the first resonance. At higher resonances, the distribution is typical of higher order mode excitation. At the upper end of the UWB range current variation is more along the length and width of the ground plane. However, the currents are in opposing phase and hence do not contribute to radiation.

78
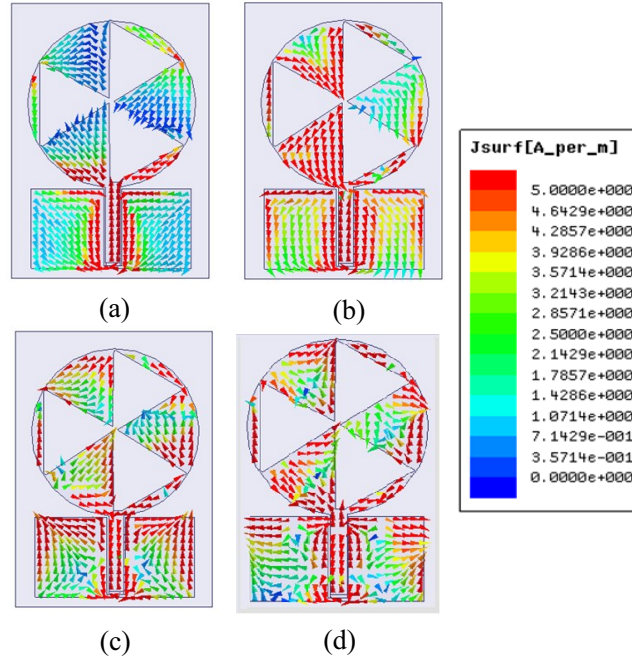
Fig. 4.6   Simulated surface current distribution of dual-band circular monopole antenna (Type-I) at resonance frequencies (a) 1.8 GHz (b) 3.3 GHz (c) 5.8 GHz (d) 10.4 GHz with $\epsilon_r = 4.4$, h = 1.6 mm, D = 34 mm, L_s = 16.7 mm, g_s = 1 mm, $\alpha = 30^0$, L_g = 17 mm, W_g = 13 mm, W_f = 3 mm, g = 0.3 mm and s = 0.55 mm

4.1.4 Design Equations of Dual-band Circular Monopole Antenna (Type-I)

From the parametric analysis carried out for the various dimensions of the antenna, the

design equations can be formulated and the step by step procedure is listed below:

1)   Design a 50 Ω CPW line of width, W_f and gap, g from ground plane on a substrate with permittivity ϵ_r. Calculate ϵ_{reff} using $\epsilon_{reff} = (\epsilon_r + 2) / 3$ where ϵ_{reff} is the effective permittivity of the substrate.

2)   The length of the ground plane on either side of the feed line is calculated using

$$L_g = 0.566\lambda_c \qquad (4.1)$$

where λ_c is the guide wavelength corresponding to center frequency of the UWB operating range.

3) The width of the ground plane on either side of the feed line is calculated using

$$W_g = 0.433\lambda_c \qquad (4.2)$$

4) Design a circular monopole of diameter

$$D = 0.405\lambda_m \qquad (4.3)$$

where λ_m is the guide wavelength corresponding to the average frequency, f_m of desired lower resonance frequency and UWB lower limit.

5) The gap between monopole and ground, s is set using

$$s = 0.017\lambda_{c'} \qquad (4.4)$$

where $\lambda_{c'}$ is the guide wavelength corresponding to center of ultra wide operating range from f_m.

6) Design the slot side length using the regression equation

$$L_s = -5.33f_1 - 0.85\epsilon_r - 0.558h + 31.987 \qquad (4.5)$$

where f_1 is the frequency in GHz corresponding to the first resonance. This equation is valid for substrates with $2.2 < \epsilon_r < 6.15$ and 0.8 mm $< h < 2$ mm for frequency range 1.6 GHz $< f_1 < 2.2$ GHz.

7) Gap in the middle of the slot, g_s is set as

$$g_s = 0.033\lambda_c \qquad (4.6)$$

To validate the design equations, the antenna dimensions to obtain UWB band and a lower resonance at 1.8 GHz are computed for the different substrates as shown in Table 4.1.

Table. 4.1   Dual-band circular monopole antenna (Type-I) parameters for different substrates obtained from design equations

Parameter (mm)	Substrate			
	1	2	3	4
	Rogers 5880 $\epsilon_r = 2.2$	Rogers RO4003 $\epsilon_r = 3.55$	FR-4 Epoxy $\epsilon_r = 4.4$	Rogers RO3006 $\epsilon_r = 6.15$
h	1.57	0.8	1.6	1.28
W_f	4	6	3	2.58
g	0.17	0.3	0.3	0.45
L_g	21	18.2	16.98	15.03
W_g	16.03	13.94	13	11.49
L_s	19.65	18.9	17.7	16.45
D	41.9	36.5	33.9	31
s	0.66	0.57	0.53	0.47
g_s	1.22	1.06	0.99	0.88

The reflection characteristics obtained for the antenna designed on the different substrates are shown in Fig. 4.7.
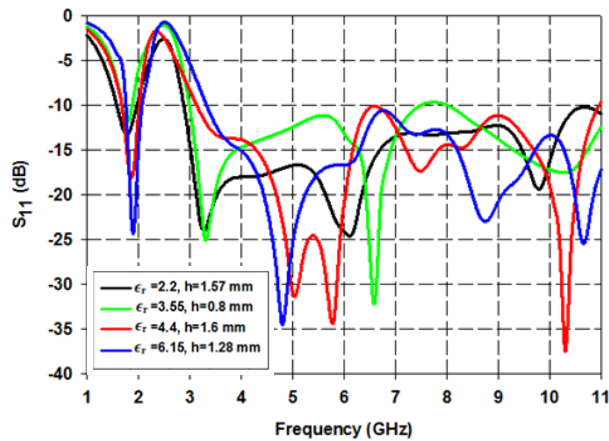
Fig. 4.7   Simulated reflection characteristics of dual-band circular monopole antenna (Type-I) on different substrates

The lower band resonances and lower limit of the UWB band obtained from simulation using the design values are compared with desired resonance of 1.8 GHz and 3.1 GHz in Table 4.2.

 On all substrates, the design results in dual-band behavior with a wide band suitable for UWB which validates the formulated empirical design equations.

Table.4.2   % Error in simulated frequency of dual-band circular monopole antenna (Type-I) for different dielectric substrates at f_l = 1.8 GHz and f_L = 3.1 GHz

Substrate	Simulated Frequency (GHz)		Error (%)	
	f_l	f_L	f_l	f_L
Rogers 5880 (ϵ_r = 2.2, h = 1.57 mm)	1.77	2.93	1.6	5
Rogers RO4003 (ϵ_r = 3.55, h = 0.8 mm)	1.79	3	0.5	3.2
FR-4 Epoxy (ϵ_r = 4.4, h = 1.6 mm)	1.87	3.12	3.9	0.6
Rogers RO3006 (ϵ_r = 6.15, h = 1.28 mm)	1.89	3.3	5	6.4

4.1.5 Reflection Characteristics of Dual-band Circular Monopole Antenna (Type-I)

The antenna with optimized dimensions is fabricated on a substrate of thickness 1.6 mm and permittivity 4.4 as shown in Fig. 4.8 (a). Testing is done using programmable network analyzer (PNA) E8362B. Simulated and measured readings are compared in Fig. 4.8 (b). The simulated and measured readings are found to be in good agreement with $S_{11} \leq -10$ dB for 1.68–2.06 GHz and 3.27–11 GHz. Mismatch in readings are observed beyond 5 GHz which could be due to soldering effects of the SMA connector.

(a)   (b)
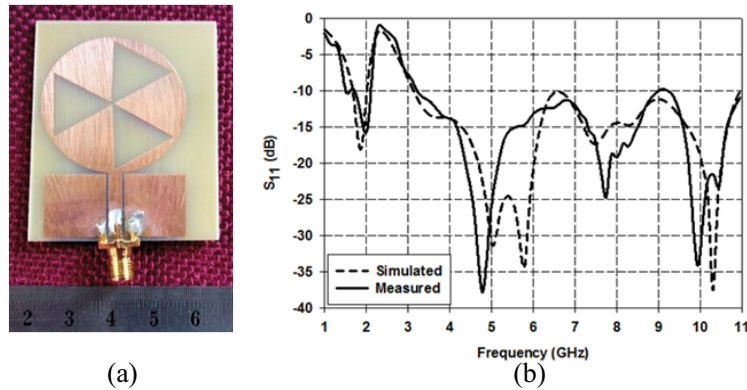
Fig. 4.8   (a) Fabricated prototype (b) Simulated and measured reflection
characteristics of dual-band circular monopole antenna (Type-I)
with $\epsilon_r = 4.4$, h = 1.6 mm, D = 34 mm, L_s = 16.7 mm, g_s = 1 mm,
$\alpha = 30^0$, L_g = 17 mm, W_g = 13 mm, W_f = 3 mm, g = 0.3 mm and
s = 0.55 mm

4.1.6 Radiation Pattern of Dual-band Circular Monopole Antenna (Type-I)

The simulated 3D radiation patterns of the antenna at the lower resonance frequency

and lower, middle and upper frequencies of the UWB band are shown in Fig. 4.9.
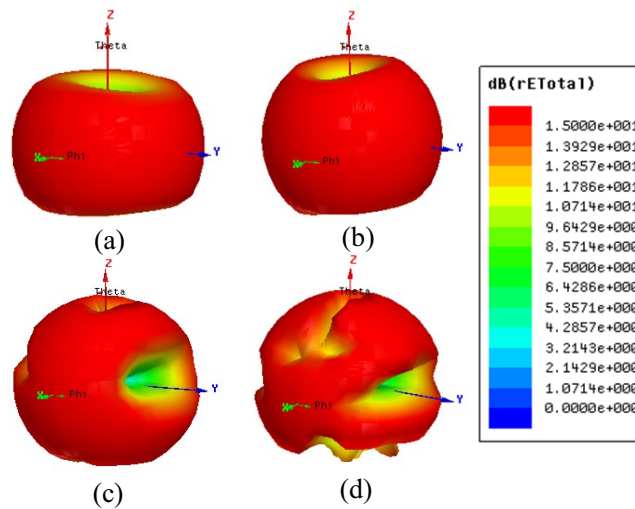
Fig. 4.9   Simulated 3D radiation patterns of the dual-band circular
monopole antenna (Type-I) at the operating frequencies (a) 1.8
GHz (b) 3.3 GHz (c) 5.8 GHz (d) 10.4 GHz with $\epsilon_r = 4.4$, h =
1.6 mm, D = 34 mm, L_s = 16.7 mm, g_s = 1 mm, $\alpha = 30^0$, L_g =
17 mm, W_g = 13 mm, W_f = 3 mm, g = 0.3 mm and s = 0.55 mm

83

The corresponding measured radiation patterns are shown in Fig. 4.10.
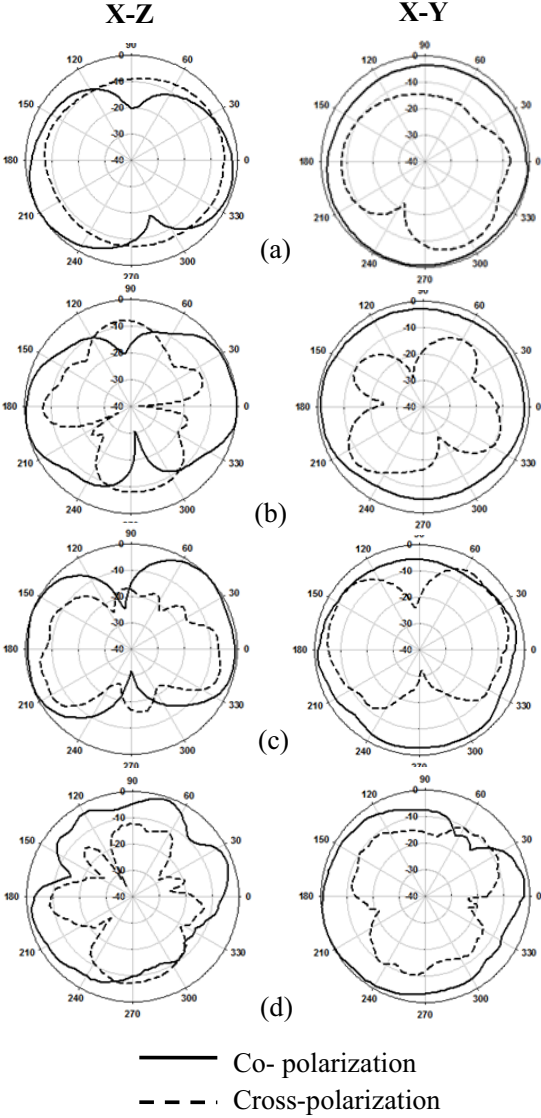
Fig. 4.10   Normalized 2D radiation pattern of dual-band circular monopole antenna (Type-I) measured at (a) 1.8 GHz (b) 3.3 GHz (c) 5.8 GHz (d) 10.4 GHz with $\epsilon_r = 4.4$, h = 1.6 mm, D = 34 mm, L_s = 16.7 mm, g_s = 1 mm, $\alpha = 30^0$, L_g = 17 mm, W_g = 13 mm, W_f = 3 mm, g = 0.3 mm and s = 0.55 mm

At the resonance corresponding to the lower band, a doughnut pattern is observed. This is because this band is controlled only by the perimeter of the slot in the monopole. The radiation patterns show good cross polarization levels at the lower resonance. Throughout the UWB band, the levels are moderate, and better than that of the antenna presented in Chapter 3. At lower frequencies of the UWB band also, the doughnut pattern is seen. At 5.8 GHz, the pattern shape changes but is almost non-directional in the horizontal plane. At 10.4 GHz, the pattern becomes quite distorted due to the excitation of higher order modes in the monopole. The patterns have a near figure-8 shape in the E-plane (X-Z) and are non-directional in the H-plane (X-Y). At higher frequencies, the shape is somewhat distorted which is due to the excitation of higher modes as commonly seen in such antennas.

4.1.7 Gain and Efficiency of Dual-band Circular Monopole Antenna (Type-I)

The peak gain and efficiency of the antenna are measured using the techniques outlined in Chapter 2 and are plotted in Fig. 4.11.

(a)   (b)
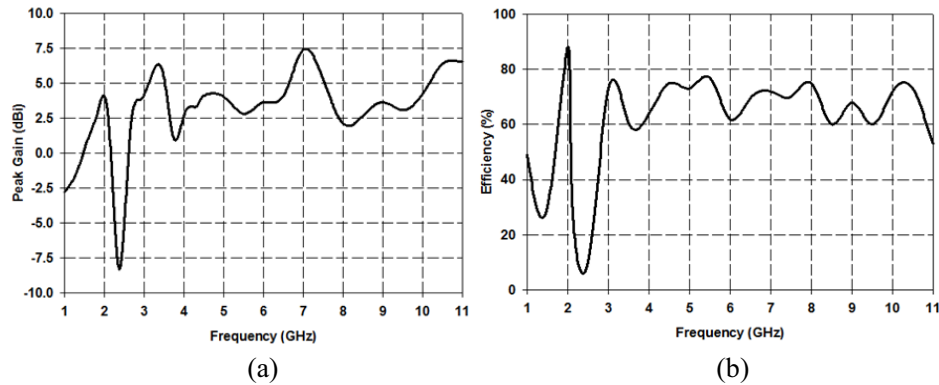
Fig. 4.11   (a) Peak gain and (b) Efficiency of dual-band circular monopole antenna (Type-I) with ϵ_r = 4.4, h = 1.6 mm, D = 34 mm, L_s = 16.7 mm, g_s = 1 mm, α = 30^0, L_g = 17 mm, W_g = 13 mm, W_f = 3 mm, g = 0.3 mm and s = 0.55 mm

The antenna gain is 2.82 dBi at 1.8 GHz while in the UWB range the maximum gain is 7.35 dBi. The efficiency readings are in reasonably good agreement with the gain values. The antenna offers an efficiency of 88 % at lower resonance and a maximum of 78 % in the UWB range.

In order to improve the impedance matching in the UWB range of the dual-band antenna, a fractal design is proposed. Here, the slotted circular monopole is scaled down in diameter and inserted in the space created by the slot. This space filling geometry is proposed as Type-II design and details are discussed next.

4.2 DUAL-BAND CIRCULAR FRACTAL MONOPOLE ANTENNA (TYPE-II)

4.2.1 Antenna Geometry

In Type-I design, the CPW-fed simple circular monopole from which the design is developed, has a wideband characteristic starting from 2.45 GHz. By inserting the proposed slot, dual-band characteristics are obtained with a lower resonance at 1.8 GHz suitable for GSM and a wide band from 3-11 GHz for UWB applications. But impedance matching is poor from 6.4-7 GHz. On introducing a fractal design the lower resonance frequency is undisturbed while improved impedance matching is seen in the UWB band. The evolution of the geometry is shown in Fig. 4.12.

The geometry of Type-I antenna is modified to obtain the structure of Type-II antenna. This antenna supports GSM (1.71-1.98 GHz) and UWB (3.1-10.6 GHz) applications. The antenna is fed by a similar 50 Ω CPW and printed on a substrate of thickness h = 1.6 mm, relative dielectric constant ϵ_r = 4.4 and loss tangent tan δ = 0.02.
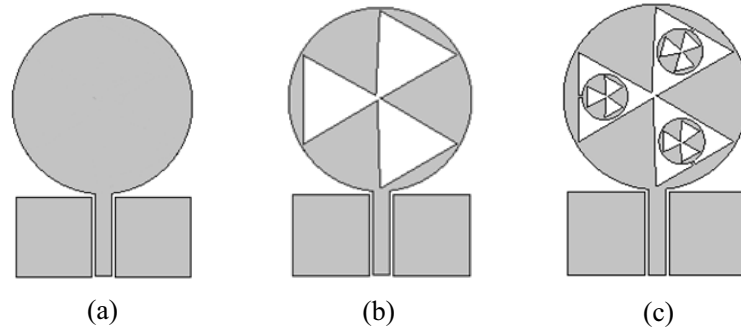
Fig. 4.12　Evolution of the dual-band circular fractal monopole antenna (Type-II) geometry (a) Simple circular monopole (b) Iteration 0 (c) Iteration 1

The simple circular monopole shown in Fig. 4.12 (a) results in wideband operation and on introducing a slot in the monopole, dual band characteristics are obtained. By introducing the fractal pattern, dual band characteristics are retained with improved impedance matching is obtained between 6 and 7 GHz. The fractal pattern is obtained using a similar procedure used for the multiband fractal antenna described in Section 3.1. The reflection characteristics for each iteration are shown in Fig. 4.13.
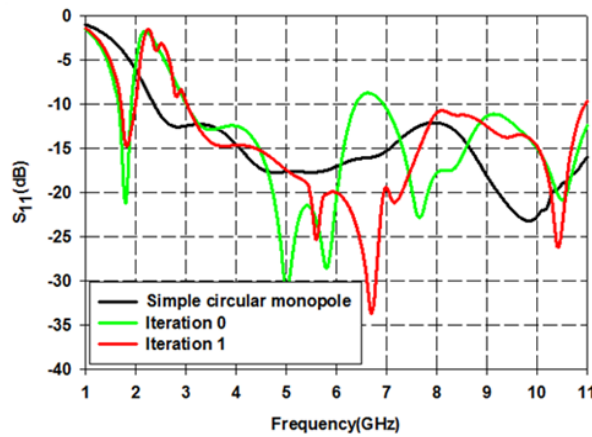
Fig 4.13　Simulated S_{11} vs frequency of dual-band circular fractal monopole antenna (Type-II) for various iterations with ϵ_r = 4.4, h = 1.6 mm, D = 34 mm, L_g = 17 mm, W_g = 13 mm, W_f = 3 mm, g_1 = 0.3 mm, s = 0.55 mm, g_2 = 0.5 mm, g_s = 0.3 mm, L_s = 16.7 mm, D_i = 8.4 mm and L_{si} = 3.9 mm

87

The circular monopole has a diameter D and is spaced from the ground plane by a distance s. The truncated ground plane is of length L_g and width W_g. The slot inscribed in the circular monopole has a side length L_s and the fractal pattern is created by inner circles of diameter D_i with inscribed slots of side length L_{si}. The antenna has a same overall size of 34×51 mm^2 as that of Type-I antenna. The geometry of the proposed antenna with the optimized dimensions is shown in the Fig. 4.14.
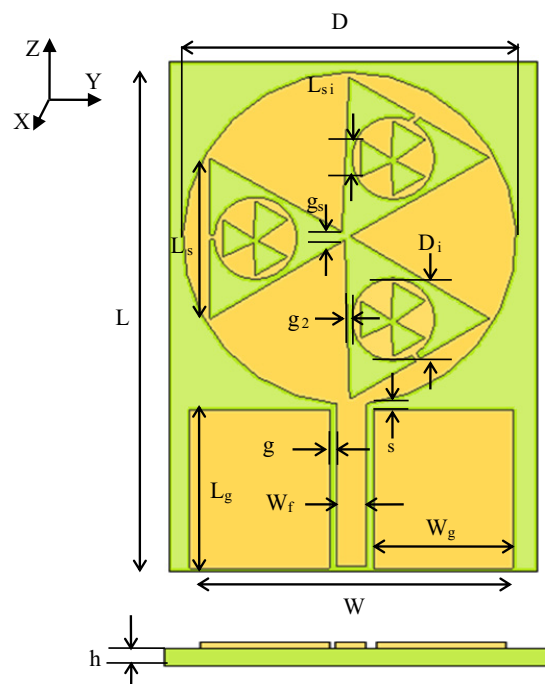
Fig. 4.14   Geometry of dual-band circular fractal monopole antenna (Type-II) with optimized dimensions D = 34 mm, W = 29.6 mm, L = 51 mm, L_g = 17 mm, W_g = 13 mm, W_f = 3 mm, g_1 = 0.3 mm, s = 0.55 mm, g_2 = 0.5 mm, g_s = 0.3 mm, L_s = 16.7 mm, D_i = 8.4 mm and L_{si} = 3.9 mm for ϵ_r = 4.4, h = 1.6 mm

4.2.2 Parametric Analysis of Dual-band Circular Fractal Monopole Antenna (Type-II)

Following the parametric analysis of the CPW-fed slotted multiband antenna Type-I discussed in Section 4.1.2, the Type-II antenna differs in the fractal pattern that is introduced. In Type-I antenna, the slot dimensions are optimized for operation in GSM and UWB bands. However, for the chosen dimension of slot side length, there is mismatch in the UWB range.

To improve the matching in the UWB range without disturbing the first resonance, the slotted circular monopole diameter is scaled down to diameter D_i and inserted in space within the slot to create a fractal design. Fig. 4.15 shows reflection characteristics for varying fractal scaling factor, F.
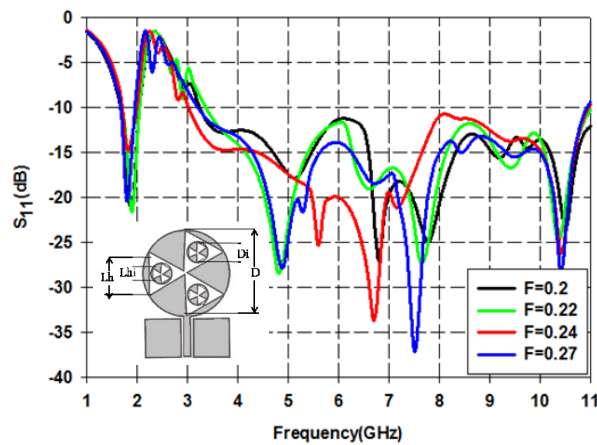
Fig. 4.15   Simulated S_{11} vs frequency of dual-band circular fractal monopole antenna (Type-II) with varying F with $\epsilon_r = 4.4$, h = 1.6 mm, $L_g = 17$ mm, $W_g = 13$ mm $W_f = 3$ mm, $g_1 = 0.3$ mm, s = 0.55 mm, $g_2 = 0.5$ mm, $g_s = 0.3$ mm, $L_s = 16.7$ mm and D = 34 mm

As fractal scaling factor, F changes, the lower band remains unchanged but matching in the UWB range varies significantly. At F = 0.24, significant improvement in

89

matching is obtained, especially in the range 5.5-7 GHz. This corresponds to $D_i = 8.4$

mm and $L_{si} = 3.9$ mm.

4.2.3 Surface Current Distribution of Dual-band Circular Fractal Monopole Antenna (Type-II)

The surface current distribution of the antenna Type-II at various resonance frequencies

is shown in Fig. 4.16.
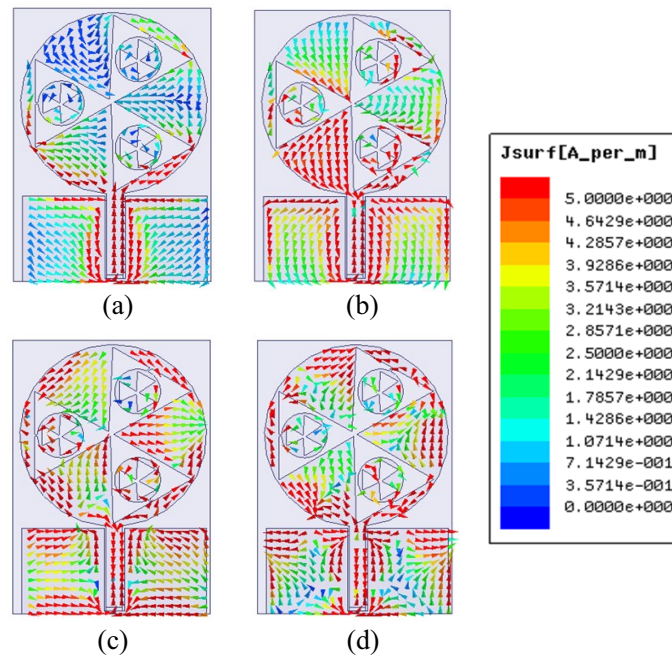
Fig. 4.16   Simulated surface current distribution of dual-band circular fractal monopole antenna (Type-II) at resonance frequencies (a) 1.8 GHz (b) 3.3 GHz (c) 6.7 GHz (d) 10.4 GHz with $\epsilon_r = 4.4$, h = 1.6 mm, $L_g = 17$ mm, $W_g = 13$ mm, $W_f = 3$ mm, $g_1 = 0.3$ mm, s = 0.55 mm, $g_2 = 0.5$ mm, $g_s = 0.3$ mm, $L_s = 16.7$ mm, $D_i = 8.4$ mm, $L_{si} = 3.9$ mm and D = 34 mm (for F = 0.24)

At the first resonance of 1.8 GHz, variation in current is seen along the perimeter of the

slot. There is very little contribution of the inner circles to radiation characteristics at

this resonance. At 6.7 GHz however, there is a significant variation in current on the

inner circles. This explains the contribution of the fractal pattern to improved matching at this frequency. There is also a variation in current along the length of the ground plane on either side of the feed line. However, the currents are in opposing phase and hence do not contribute to radiation. At 10.4 GHz, the distribution is typical of higher order modes in CPW-fed circular monopoles. Current variations are seen along the perimeter of the monopole as well as along length and width of the ground plane. However, currents along the width and length of the ground plane are in opposing phase and so will not cause radiation.

4.2.4 Design Equations of Dual-band Circular Fractal Monopole Antenna (Type-II)

Based on the parametric analyses, the design equations for the dual-band antenna are formulated. The procedure for designing the antenna is the same as steps (1)-(7) outlined in Section 4.1.4 of Type-I design. The inner circles that form the fractal pattern are designed using fractal scaling factor

$$F = \frac{D_i}{D} = \frac{L_{si}}{L_s} = 0.24 \qquad (4.7)$$

Using these design equations, the antenna is designed and simulated on different substrates for dual-band UWB operation with lower resonance frequency f_1=1.8 GHz and the parameter values are obtained as shown in Table 4.3.

The designs are simulated in HFSS™ and dual-band operation covering GSM and UWB bands is achieved on all substrates as shown in Fig. 4.17.

Table 4.3 Dual-band circular fractal monopole antenna (Type-II) parameters for different substrates obtained from design equations

Parameter (mm)	Substrate			
	1	2	3	4
	Rogers 5880 $\epsilon_r = 2.2$	Rogers RO4003 $\epsilon_r = 3.55$	FR-4 Epoxy $\epsilon_r = 4.4$	Rogers RO3006 $\epsilon_r = 6.15$
h	1.57	0.8	1.6	1.28
W_f	4	6	3	2.5
g_1	0.17	0.3	0.3	0.45
L_g	21	18.2	16.98	15.03
W_g	16.03	13.94	13	11.49
L_s	19.65	18.9	17.7	16.45
D	41.9	36.5	33.9	31
s	0.66	0.57	0.53	0.47
D_i	10.05	8.76	8.14	7.44
L_{si}	4.98	4.07	3.78	3.25
g_2	0.65	0.54	0.5	0.43
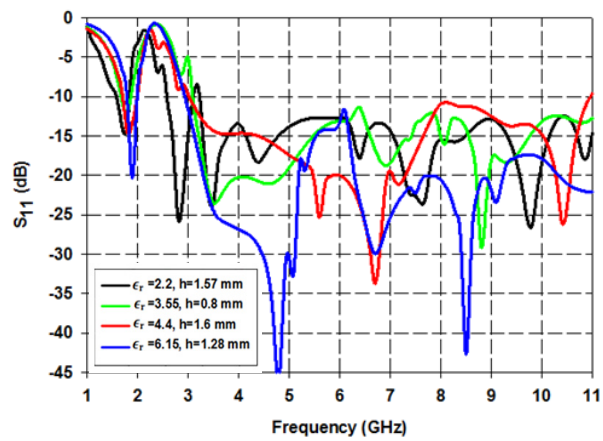
Fig. 4.17 Simulated reflection characteristics of dual-band circular fractal monopole antenna (Type-II) on different substrates

The lower band resonances and lower limit of the UWB band obtained from simulation using the design values are compared with desired frequencies 1.8 GHz and 3.1 GHz in Table 4.4.

Table 4.4   % Error in simulated frequency of dual-band circular fractal monopole antenna (Type-II) for different dielectric substrates at f_1 = 1.8 GHz and f_L = 3.1 GHz

Substrate	Simulated Frequency (GHz)		Error (%)	
	f_1	f_L	f_1	f_L
Rogers 5880 (ϵ_r = 2.2, h = 1.57 mm)	1.75	3.2	2.7	3.2
Rogers RO4003 (ϵ_r = 3.55, h = 0.8 mm)	1.79	3.08	0.5	0.6
FR-4 Epoxy (ϵ_r = 4.4, h = 1.6 mm)	1.81	3.02	0.5	2.5
Rogers RO3006 (ϵ_r = 6.15, h = 1.28 mm)	1.89	2.95	5	4.8

On all substrates error is only upto a maximum of 5 % which ensures repeatability of the design.

4.2.5 Reflection Characteristics of Dual-band Circular Fractal Monopole Antenna (Type-II)

The antenna designed with optimized dimensions is fabricated on a substrate of permittivity 4.4 and thickness 1.6 mm as shown in 4.18 (a). Testing is done using Agilent PNA E8362B. The measured results are compared with simulation values as shown in Fig. 4.18 (b).

Measured results show very good impedance match in the UWB range for the antenna. The measured and simulated readings show good agreement in their variation;

however, the lower frequency limit of the UWB range differs from simulated results and increases to 3.4 GHz. At higher frequencies, there is a mismatch between simulated and measured readings. This can be attributed to soldering effects that have not been considered in simulation studies. The operating bands of the antenna are 1.5-2 GHz and 3.4-11 GHz for $S_{11} \leq -10$ dB.

<table>
<tr><td>(a)</td><td>(b)</td></tr>
</table>
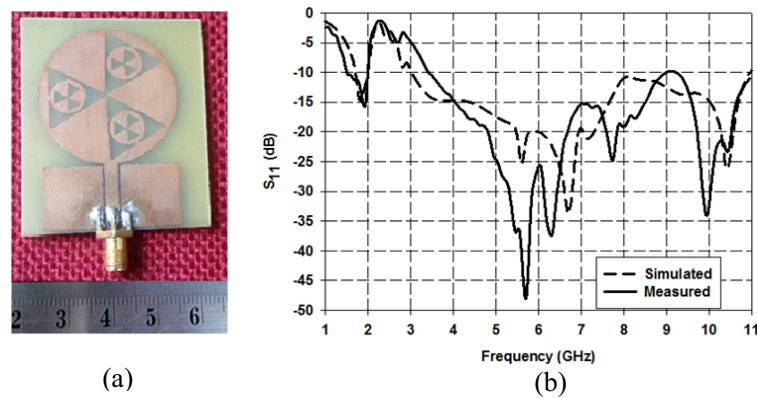
Fig. 4.18   (a) Fabricated prototype (b) Simulated and measured reflection characteristics of dual-band circular fractal monopole antenna (Type-II) with $\epsilon_r = 4.4$, h = 1.6 mm, L_g = 17 mm, W_g = 13 mm, W_f = 3 mm, g_1 = 0.3 mm, s = 0.55 mm, g_2 = 0.5 mm, g_s = 0.3 mm, L_s = 16.7 mm, D_i = 8.4 mm, L_{si} = 3.9 mm and D = 34 mm (for F = 0.24)

4.2.6 Radiation Pattern of Dual-band Circular Fractal Monopole Antenna (Type-II)

The 3D radiation patterns of the antenna are simulated in HFSS™ and shown in Fig. 4.19.

At the resonance corresponding to the lower band, a doughnut pattern is observed. At 6.7 GHz, the pattern shape changes but is almost non-directional in the horizontal

plane. At 10.4 GHz, the pattern becomes quite distorted due to the excitation of higher

order modes in the monopole.
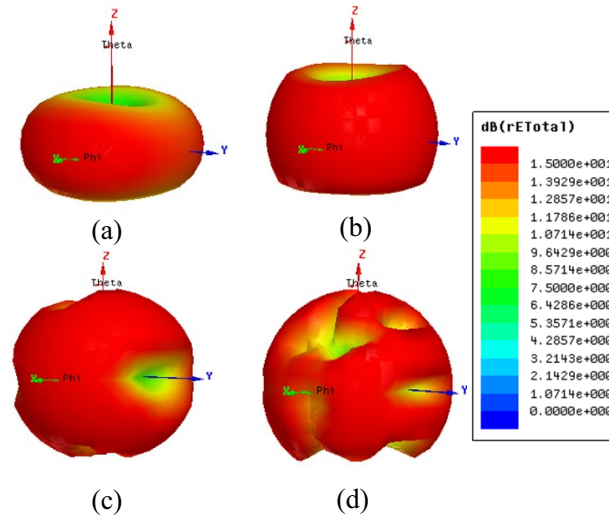
Fig. 4.19   Simulated 3D radiation patterns of the dual-band circular
fractal monopole antenna (Type-II) at the operating
frequencies (a) 1.8 GHz (b) 3.4 GHz (c) 6.7 GHz (d) 10.4
GHz with ϵ_r = 4.4, h = 1.6 mm, L_g = 17 mm, W_g = 13 mm,
W_f = 3 mm, g_1 = 0.3 mm, s = 0.55 mm, g_2 = 0.5 mm, g_s =
0.3 mm, L_s = 16.7 mm, D_i = 8.4 mm, L_{si} = 3.9 mm and D
= 34 mm (for F = 0.24)

The radiation patterns are measured using the technique outlined in Section 2.5.2 and

are normalized and plotted in two principal planes as shown in Fig. 4.20.

The patterns are similar to those inferred from the 3D simulations and have a figure-8

shape in the E-plane (X-Z) and are non-directional in the H-plane (X-Y) for most of

the intended range of frequencies. The cross polarization levels are similar to the levels

seen in Type-I antenna. It is also seen that the fractal design improves cross polarization

levels at frequencies in the mid range of the UWB band.

X-Z   **X-Y**

(a)

(b)

(c)

(d)

——— Co- polarization
- - - - Cross-polarization
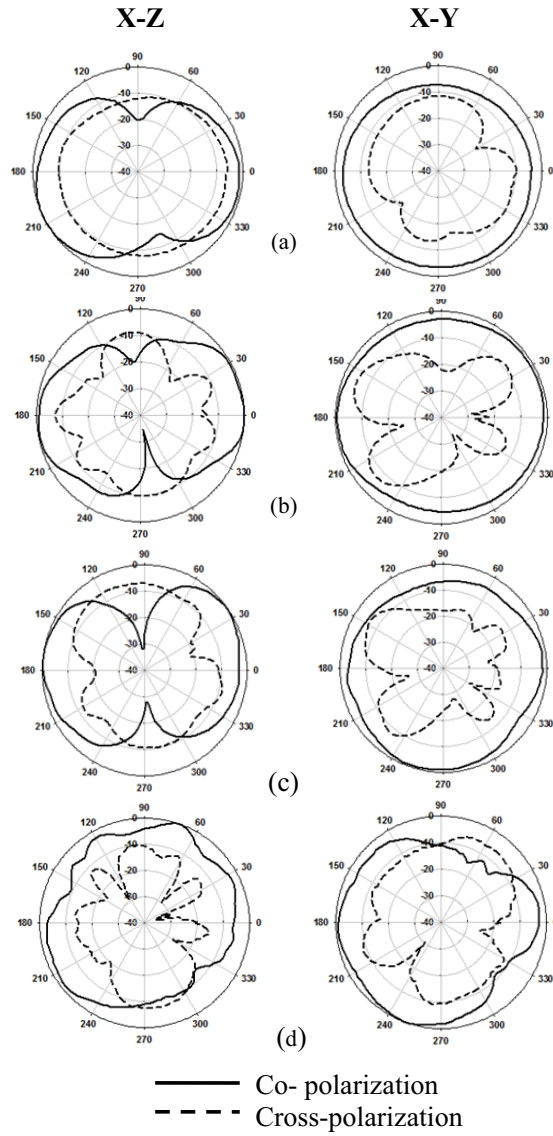
Fig. 4.20   Normalized 2D radiation pattern of the dual-band circular fractal monopole antenna (Type-II) measured at (a) 1.8 GHz (b) 3.4 GHz (c) 6.7 GHz (d) 10.4 GHz with ϵ_r = 4.4, h = 1.6 mm, L_g = 17 mm, W_g = 13 mm, W_f = 3 mm, g_1 = 0.3 mm, s = 0.55 mm, g_2 = 0.5 mm, g_s = 0.3 mm, L_s = 16.7 mm, D_i = 8.4 mm, L_{si} = 3.9 mm and D = 34 mm (for F = 0.24)

4.2.7 Gain and Efficiency of Dual-band Circular Fractal Monopole Antenna (Type-II)

The peak gain and efficiency of the antenna are measured over the entire operating range and results are shown in Fig. 4.21.

<div align="center">(a)   (b)</div>
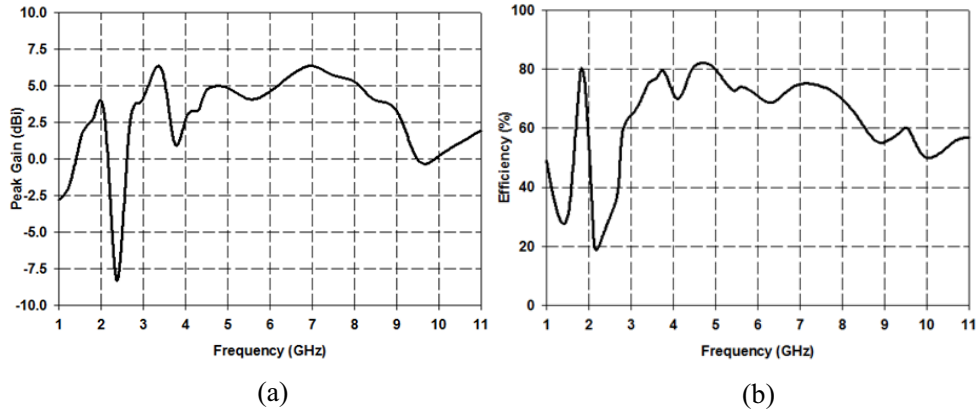
Fig. 4.21   (a) Peak gain and (b) Efficiency of dual-band circular fractal monopole antenna (Type-II) with $\epsilon_r = 4.4$, $h = 1.6$ mm, $L_g = 17$ mm, $W_g = 13$ mm, $W_f = 3$ mm, $g_1 = 0.3$ mm, $s = 0.55$ mm, $g_2 = 0.5$ mm, $g_s = 0.3$ mm, $L_s = 16.7$ mm, $D_i = 8.4$ mm, $L_{si} = 3.9$ mm and $D = 34$ mm (for $F = 0.24$)

The gain is 2.82 dBi at 1.8 GHz and in the UWB range maximum gain is 6.5 dBi. The efficiency plot is in good agreement with the gain readings with an efficiency of 80 % at lower resonance and maximum efficiency of 82 % in the UWB band. At higher frequencies, the efficiency drops which is due to the lossy nature of the substrate used.

The dual-band Type-I design can be made suitable for triple-band operation by inserting a bent monopole in the space created by the slot. The bent monopole lowers the operating frequency of the antenna and also introduces an additional resonance

without increasing the overall size of the antenna. The proposed Type-III design is presented next.

4.3 TRIPLE-BAND CIRCULAR MONOPOLE ANTENNA (TYPE-III)

4.3.1 Antenna Geometry

A triple-band antenna suitable for WMTS (1.395-1.4 GHz), UMTS (1.92-2.17 GHz) and UWB (3.1-10.6 GHz) bands is proposed. The optimized geometry of the dual-band monopole antenna (Type-I) is modified to obtain a triple-band antenna in which the first resonance is lowered without increase in the overall antenna size. In order to develop the triple-band antenna, a bent monopole is inserted in the space created by the slot. The evolution of the geometry is shown Fig. 4.22.
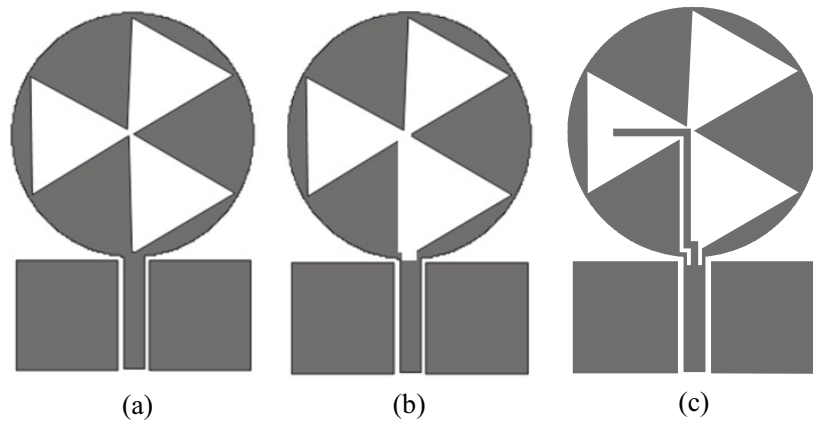
Fig. 4.22   Evolution of the triple-band circular monopole antenna (Type-III) geometry (a) Type-I geometry (b) Removal of metal near feed line (c) Insertion of bent monopole in space created by slot

The feed line and ground plane dimensions are the same as Type-I antenna on a substrate of thickness h = 1.6 mm and relative dielectric constant ϵ_r = 4.4 with loss tangent tan δ = 0.02. The antenna geometry is shown in Fig. 4.23.
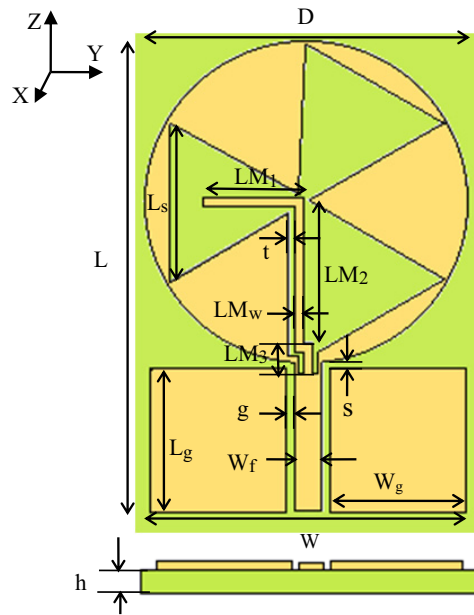
Fig. 4.23 Geometry of triple-band circular monopole antenna (Type-III) with optimized dimensions D = 34 mm, W = 29.6 mm, L = 51 mm, L_s = 16.7 mm, L_g = 17 mm, W_g = 13 mm, W_f = 3 mm, g = 0.3 mm, s = 0.55 mm, g_s = 1 mm, LM_1 = 10 mm, LM_2 = 16 mm, LM_3 = 4 mm, LM_w = 1 mm and t = 0.6 mm for ϵ_r = 4.4, h = 1.6 mm

The bent monopole is made up of three segments of lengths LM_1, LM_2 and LM_3 of width LM_w and will be efficiently excited if it is placed along the direction of current flow near the main CPW feed line. To accommodate the monopole in this manner, a portion of the circular monopole is cut away near the feed and the bent monopole is spaced at a distance, t from the slot edge as shown in Fig. 4.23. All other dimensions are the same as that of CPW-fed slotted multiband antenna Type-I.

4.3.2 Parametric Analysis of Triple-band Circular Monopole Antenna (Type-III)

The main modification in the Type-I structure to obtain the Type-III structure is the introduction of the bent monopole in the space created by the slot. The parameters of

99

the bent monopole such as length, width and spacing from slot edge are varied to study
their effect on the various operating bands.

Effect of bent monopole segment length, LM_1

The overall length of the monopole is $LM_1+LM_2+LM_3$ and results in the resonance
frequency at 2.1 GHz suitable for UMTS application. The length of the monopole
increases the overall perimeter of the slot and this lowers the first resonance frequency
of Type-I antenna to 1.4 GHz which is suitable for WMTS applications. To carry out
the parametric study on length of the bent monopole, the segment length LM_1 is varied
and S_{11} results are shown in Fig. 4.24.
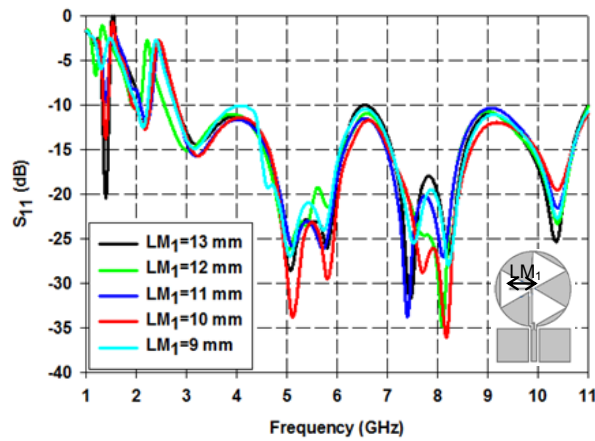
Fig. 4.24   Simulated S_{11} vs frequency of triple-band circular
monopole antenna (Type-III) for varying LM_1 with $\epsilon_r =$
4.4, h = 1.6 mm, D = 34 mm, L_s = 16.7 mm, L_g = 17 mm,
W_g = 13 mm, W_f = 3 mm, g = 0.3 mm, s = 0.55 mm, $g_s =$
1 mm, LM_2 = 16 mm, LM_3 = 4 mm, LM_w = 1 mm and t =
0.6 mm

As the length of the segment increases, the first two resonance frequencies shift towards
the lower frequency side but matching in these bands is poor. This is due to increased

100

inductance created by the bent monopole. With $LM_1 = 10$ mm there is good impedance matching in all the intended bands of operation. For the optimized dimensions, $LM_1+LM_2+LM_3$ corresponds to $0.306\lambda_{g2}$ where λ_{g2} is the guide wavelength at second resonance.

Effect of bent monopole width, LM_w

The width of the monopole is varied and corresponding reflection characteristics are plotted in Fig. 4.25.
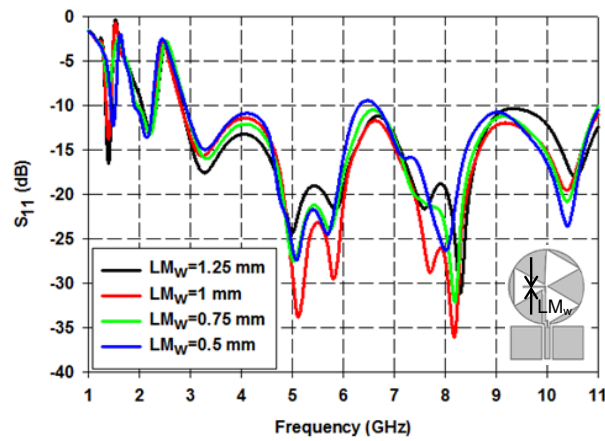
Fig. 4.25   Simulated S_{11} vs frequency of triple-band circular monopole antenna (Type-III) for varying LM_w with $\epsilon_r = 4.4$, h = 1.6 mm, D = 34 mm, L_s = 16.7 mm, L_g = 17 mm, W_g = 13 mm, W_f = 3 mm, g = 0.3 mm, s = 0.55 mm, g_s = 1 mm, LM_1 = 10 mm, LM_2 = 16 mm, LM_3 = 4 mm and t = 0.6 mm

As width is varied, the resonant frequencies are not affected much, but matching in the UWB range varies. As width is increased, the matching in the UWB range improves. This is because the increased width results in a smoother transition from feed line to the monopole at feed junction. Because of fabrication tolerance in the limited space available at the monopole feed junction the width is chosen as 1 mm. The optimum

101

width of $LM_w = 1$ mm equates to $0.035\lambda_c$ where λ_c is the guide wavelength at center of the UWB band.

Effect of gap between bent monopole and slot edge, t

The parametric analysis on separation of bent monopole from edge of the slot is shown in Fig. 4.26.
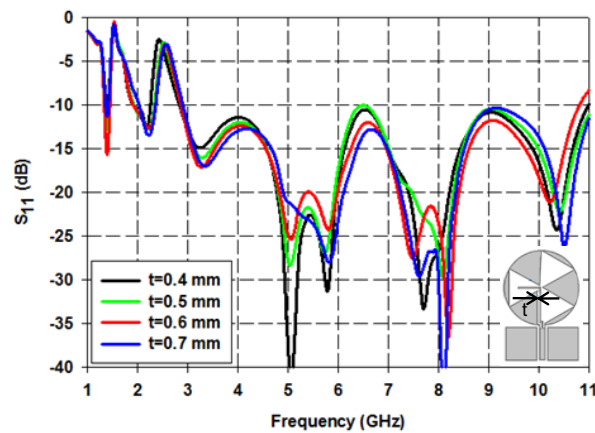
Fig. 4.26   Simulated S_{11} vs frequency of triple-band circular monopole antenna (Type-III) for varying t with $\epsilon_r = 4.4$, h = 1.6 mm, D = 34 mm, L_s = 16.7 mm, L_g = 17 mm, W_g = 13 mm, W_f = 3 mm, g = 0.3 mm, s = 0.55 mm, g_s = 1 mm, LM_1 = 10 mm, LM_2 = 16 mm, LM_3 = 4 mm and LM_w = 1mm

The parametric study on separation, t from the slot edge shows that as separation is increased, matching in UWB range improves. The increase in gap increases the capacitive reactance which cancels the inductive reactance created by the monopole and this improves matching in the UWB range. The gap is not increased further as this would make it difficult to accommodate the bent monopole without merging with the edges of the slot at the monopole feed junction. The optimized gap of t = 0.6 mm corresponds to $0.021\lambda_c$.

4.3.3 Surface Current Distribution of Triple-band Circular Monopole Antenna (Type-III)

The effect of antenna dimensions on antenna characteristics can be understood from

the surface current distribution shown in Fig. 4.27.
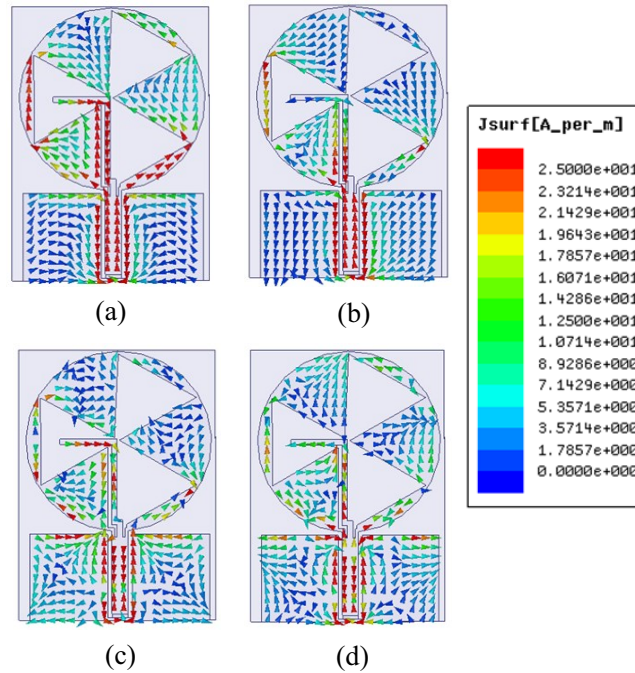
Fig. 4.27   Simulated surface current distribution of triple-band circular monopole antenna (Type-III) at resonance frequencies (a) 1.4 GHz (b) 2.1 GHz (c) 7 GHz (d) 10.4 GHz with ϵ_r = 4.4, h = 1.6 mm, D = 34 mm, L_s = 16.7 mm, L_g = 17 mm, W_g = 13 mm, W_f = 3 mm, g = 0.3 mm, s = 0.55 mm, g_s = 1 mm, LM_1 = 10 mm, LM_2 = 16 mm, LM_3 = 4 mm, LM_w = 1 mm and t = 0.6 mm

It is seen that at first resonance the current is distributed on the bent monopole as well

as on the perimeter of the slot. This confirms that the perimeter of the slot is extended

by the monopole. Thus the first resonance of 1.8 GHz in the structure of Type-I antenna

is lowered to 1.4 GHz in the proposed Type-III antenna. At 2.1 GHz distribution is

103

mainly seen along the length of the monopole element. At the higher resonances, the current distribution along perimeter of the monopole and along length and width of the ground plane are typical of higher order modes in circular monopoles.

4.3.4 Design Equations of Triple-band Circular Monopole Antenna (Type-III)

The design procedure is similar to the steps used for Type-I antenna design presented in Section 4.1.4. Since the only modification is the introduction of the bent monopole, the equations used for circular monopole and ground are the same as that of Type-I antenna from step (1)-(7) as listed in Section 4.1.4. The subsequent design steps are:

1) Design a bent monopole of length

$$LM_1 + LM_2 + LM_3 = 0.306\lambda_{g2} \qquad (4.8)$$

where λ_{g2} is the guide wavelength corresponding to the second resonance. The segment lengths are chosen such that the gap from the slot edge, t is uniform.

2) The width of the bent monopole, LM_w is calculated as

$$LM_w = 0.035\lambda_c \qquad (4.9)$$

where λ_c is the guide wavelength corresponding to center frequency of the UWB range.

3) The spacing between the bent monopole and slot edge, t is set as

$$t = 0.021\lambda_c \qquad (4.10)$$

To validate the design equations the antenna is designed on different substrates. The design values for four different substrates to obtain UWB band with two lower resonances at 1.4 GHz and 2.1 GHz are listed in Table 4.5 and the simulated reflection characteristics are shown in Fig. 4.28.

Table 4.5 Triple-band circular monopole antenna (Type-III) parameters for different substrates obtained from design equations

Parameter (mm)	Substrate			
	1	2	3	4
	Rogers 5880 $\epsilon_r = 2.2$	**Rogers RO4003** $\epsilon_r = 3.55$	**FR-4 Epoxy** $\epsilon_r = 4.4$	**Rogers RO3006** $\epsilon_r = 6.15$
h	1.57	0.8	1.6	1.28
W_f	4	6	3	2.58
g	0.17	0.3	0.3	0.45
L_g	21	18.2	16.98	15.03
W_g	16.03	13.94	13	11.49
L_s	19.65	18.9	17.7	16.45
D	41.9	36.5	33.9	31
s	0.66	0.57	0.53	0.47
LM_1	10.69	10.3	9.95	9.46
LM_2	21	16.83	16	13.7
LM_3	5.25	5	4	3.4
LM_w	1.3	1.13	1.05	0.93
t	0.78	0.68	0.63	0.56
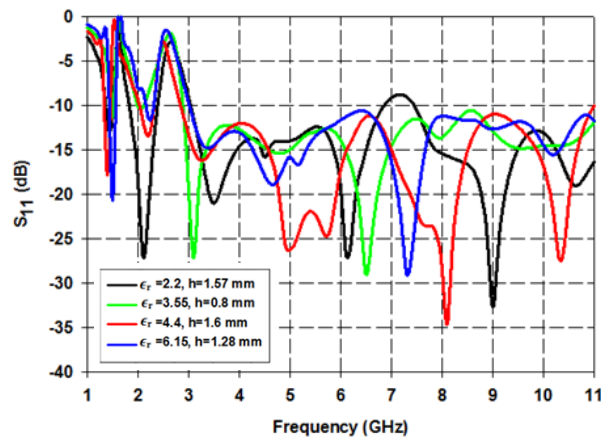
Fig. 4.28   Simulated reflection characteristics of triple-band circular monopole antenna (Type-III) on different substrates

On all substrates triple-band operation is obtained with two lower narrow bands and a UWB band in similar frequency ranges. The resonance frequencies of the two lower bands and lower limit of the UWB range are compared with the desired frequencies of 1.4 GHz, 2.1 GHz and 3.1 GHz in Table 4.6.

Table 4.6   % Error in simulated frequency of triple-band circular monopole antenna (Type-III) for different dielectric substrates, at f_1 = 1.4 GHz, f_2 = 2.1 GHz and f_L = 3.1 GHz

Substrate	Simulated Frequency (GHz)			Error (%)		
	f_1	f_2	f_L	f_1	f_2	f_L
Rogers 5880 (ϵ_r = 2.2, h = 1.57 mm)	1.44	2.13	3.04	2.8	1.4	1.9
Rogers RO4003 (ϵ_r = 3.55, h = 0.8 mm)	1.45	2.05	2.97	3.5	2.4	4.2
FR-4 Epoxy (ϵ_r = 4.4, h = 1.6 mm)	1.39	2.18	2.95	0.7	0.9	4.8
Rogers RO3006 (ϵ_r = 6.15, h = 1.28 mm)	1.46	2.2	3.04	4.2	4.7	1.9

On all substrates, maximum error less than 5 % of desired frequency is observed which ensures that the design equations developed are valid.

4.3.5 Reflection Characteristics of Triple-band Circular Monopole Antenna (Type-III)

The fabricated antenna is tested using Agilent PNA E8362B and reflection characteristics for the antenna are obtained as described in Section 2.5.1. The antenna is fabricated on a substrate of thickness 1.6 mm and permittivity 4.4 as shown in 4.29 (a). Experimental results are compared with simulated values as shown in Fig. 4.29 (b).

Triple-band behaviour is obtained with impedance matching in the desired lower frequency ranges and the UWB range.

<div align="center">(a)   (b)</div>
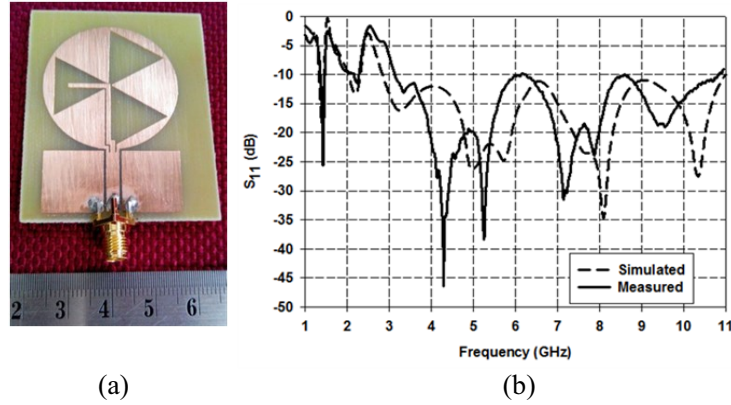
Fig. 4.29   (a) Fabricated prototype (b) Simulated and measured reflection characteristics of triple-band circular monopole antenna (Type-III) with $\epsilon_r = 4.4$, h = 1.6 mm, D = 34 mm, $L_s = 16.7$ mm, $L_g = 17$ mm, $W_g = 13$ mm, $W_f = 3$ mm, g = 0.3 mm, s = 0.55 mm, $g_s = 1$ mm, $LM_1 = 10$ mm, $LM_2 = 16$ mm, $LM_3 = 4$ mm, $LM_w = 1$ mm and t = 0.6 mm

The measured readings have the same variation as the simulated values and the antenna has operating bands for $S_{11} \leq$ -10 dB from 1.35–1.48 GHz, 2–2.27 GHz and 3.14–10.8 GHz. At higher frequencies, the measured and simulated results show some difference. This may be due to uncertainty in thickness and/or dielectric constant of substrate and soldering effects of the SMA connector, which have been neglected in the simulations.

4.3.6 Radiation Pattern of Triple-band Circular Monopole Antenna (Type-III)

The simulated 3D radiation patterns of the antenna at the lower resonances as well as at the middle and upper operating frequencies of the UWB band are shown in Fig. 4.30. At the two lower resonances, the antenna has a doughnut pattern but at higher resonances in the UWB range the pattern shape changes.
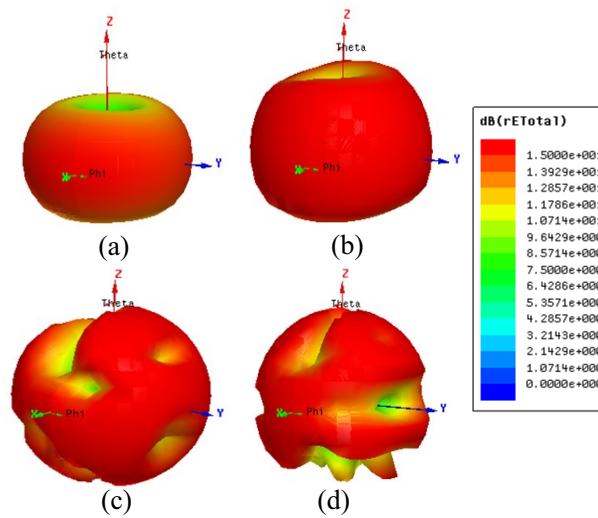
Fig. 4.30   Simulated 3D radiation patterns of the triple-band circular
monopole antenna (Type-III) at the operating frequencies
(a) 1.4 GHz (b) 2.1 GHz (c) 7 GHz (d) 10.4 GHz with ϵ_r
= 4.4, h = 1.6 mm, D = 34 mm, L_s = 16.7 mm, L_g = 17
mm, W_g = 13 mm, W_f = 3 mm, g = 0.3 mm, s = 0.55 mm,
g_s = 1 mm, LM_1 = 10 mm, LM_2 = 16 mm, LM_3 = 4 mm,
LM_w = 1 mm and t = 0.6 mm

The patterns are very similar to the patterns seen in the slotted monopole Type-I

antenna with a distortion at higher frequencies due to the excitation of higher order

modes. The corresponding measured radiation patterns are plotted in Fig. 4.31. The

measured radiation patterns are plotted in two principal planes and they are in good

agreement with the simulated 3D radiation patterns. The patterns have a figure-8 shape

in the E-plane (X-Z) and non-directional pattern in the H-plane (X-Y) for the lower

resonance frequencies but become slightly distorted at higher frequencies. The cross

polarization levels are moderate throughout the operating bands however it degrades at

the second resonance of 2.1 GHz which is due to the asymmetrical structure of the bent

monopole which produces this resonance.

X-Z   **X-Y**

(a)

(b)

(c)

(d)

————— Co- polarization
– – – – · Cross-polarization
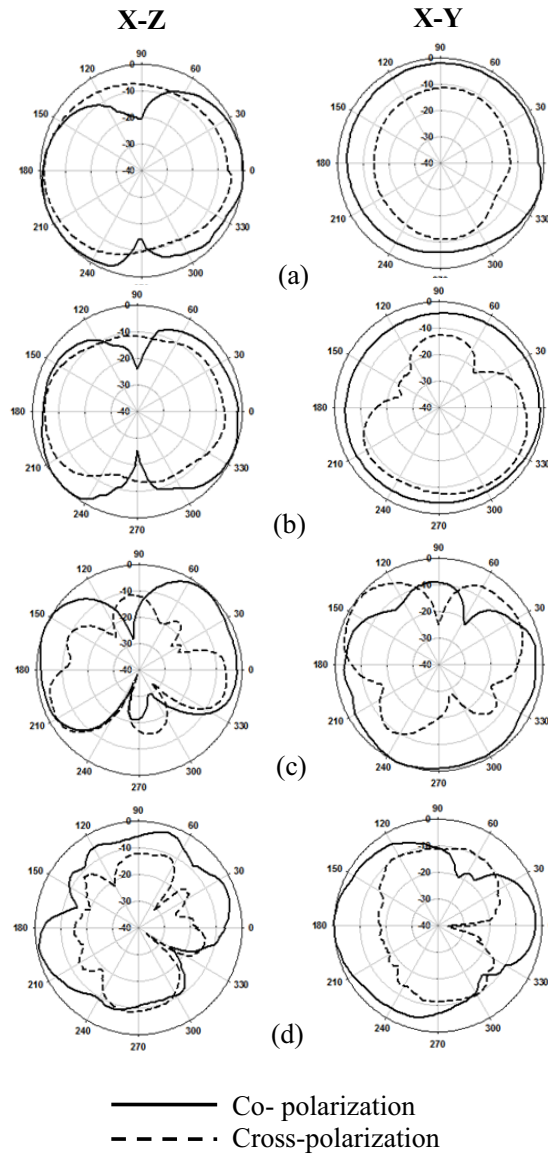
Fig. 4.31   Normalized 2D radiation pattern of triple-band circular monopole antenna (Type-III) measured at (a) 1.4 GHz (b) 2.1 GHz (c) 7 GHz (d) 10.4 GHz with ϵ_r = 4.4, h = 1.6 mm, D = 34 mm, L_s = 16.7 mm, L_g = 17 mm, W_g = 13 mm, W_f = 3 mm, g = 0.3 mm, s = 0.55 mm, g_s = 1 mm, LM_1 = 10 mm, LM_2 = 16 mm, LM_3 = 4 mm, LM_w = 1 mm and t = 0.6 mm

4.3.7 Gain and Efficiency of Triple-band Circular Monopole Antenna (Type-III)

The variation of gain and efficiency of the antenna with frequency is plotted in Fig. 4.32.

(a)	(b)
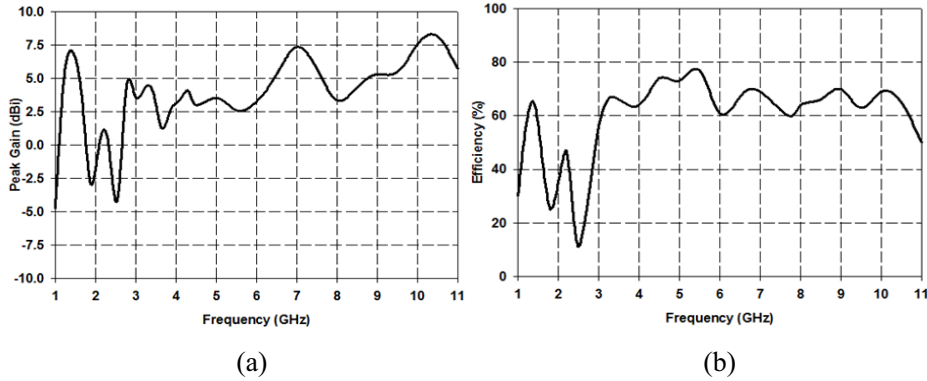
Fig. 4.32   (a) Peak gain and (b) Efficiency of triple-band circular monopole antenna (Type-III) with ϵ_r = 4.4, h = 1.6 mm, D = 34 mm, L_s = 16.7 mm, L_g = 17 mm, W_g = 13 mm, W_f = 3 mm, g = 0.3 mm, s = 0.55 mm, g_s = 1 mm, LM_1 = 10 mm, LM_2 = 16 mm, LM_3 = 4 mm, LM_w = 1 mm and t = 0.6 mm

For the triple-band antenna the gain is 6.9 dBi at 1.4 GHz, 0.2 dBi at 2.1 GHz and a maximum gain of 8.17 dBi in the UWB range. The efficiency plot has a variation similar to that of the peak gain. At the first resonance, efficiency is 65 % and at the second resonance it is 47 %. In the UWB range, efficiency upto 78 % is observed.

4.4 TIME DOMAIN ANALYSIS OF CPW-FED SLOTTED MULTIBAND ANTENNAS

All the proposed CPW-fed slotted multiband UWB antennas are intended to work throughout the frequency range from 3.1-10.6 GHz. UWB systems communicate using a series of narrow un-modulated pulses where each pulse carries one symbol of information. Time domain analysis is carried out to evaluate the suitability of the

proposed antennas for pulsed communication in an impulse radio UWB system.

4.4.1 Group Delay

The group delay of the three types of antennas measured for different azimuth orientations with a separation of 15 cm is shown in Fig. 4.33.
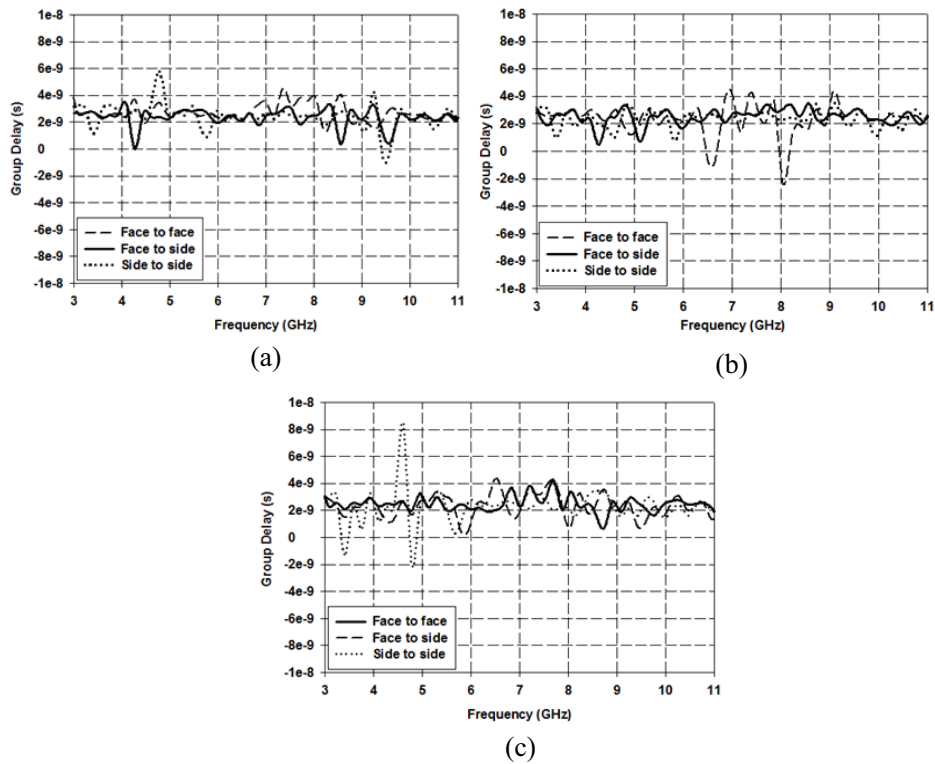
Fig. 4.33   Measured group delay of CPW-fed slotted multiband antenna (a) Type-I (b) Type-II (c) Type-III for different orientations

In the case of Type-I antenna group delay variation is least for face to side orientation with a maximum variation of less than 3 ns. For the other two orientations, group delay occasionally exceeds 5 ns. For Type-II antenna, it is seen that in the face to side and

side to side orientation, maximum group delay variation is 3 ns. In the face to face orientation large variation is seen occasionally. This is due to the complicated current path introduced by the fractal pattern used to achieve improved matching in this frequency range.

Type-III antenna has the lowest operating frequency for the same physical dimensions which corresponds to a reduction in antenna size. As size decreases, phase difference between the surface currents at different parts of the antenna is minimum. Thus, least average group delay is seen for Type-III antenna.

4.4.2 Transfer Function and Impulse Response

The antenna transfer functions obtained from S_{21} values measured at 45° increments in azimuth (X-Y) plane are shown in Fig. 4.34.
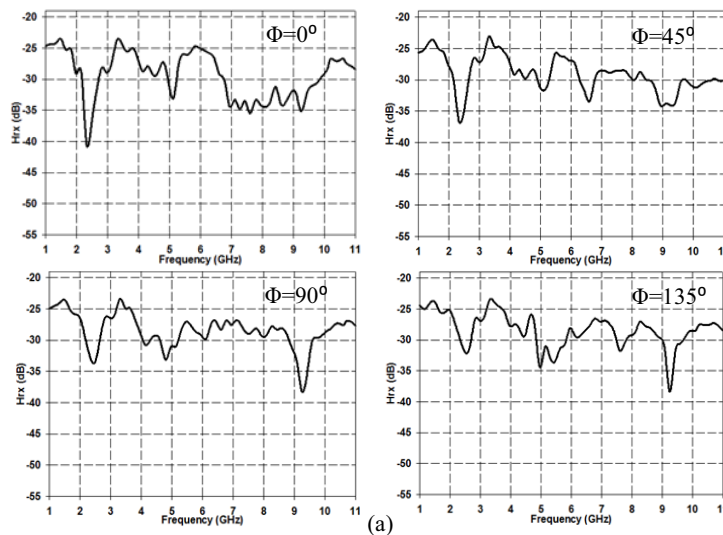
Fig. 4.34   Computed transfer function of CPW-fed slotted multiband antenna (a) Type-I (b) Type-II (c) Type-III for different angles in azimuth plane

112

(b)

(c)
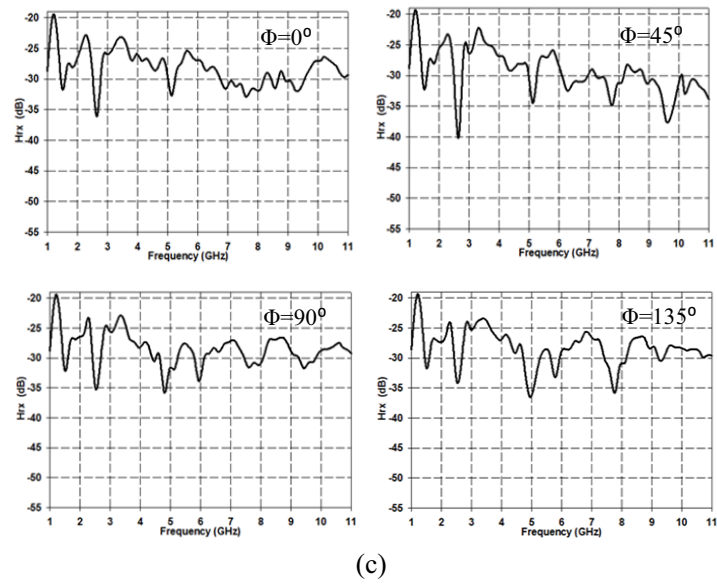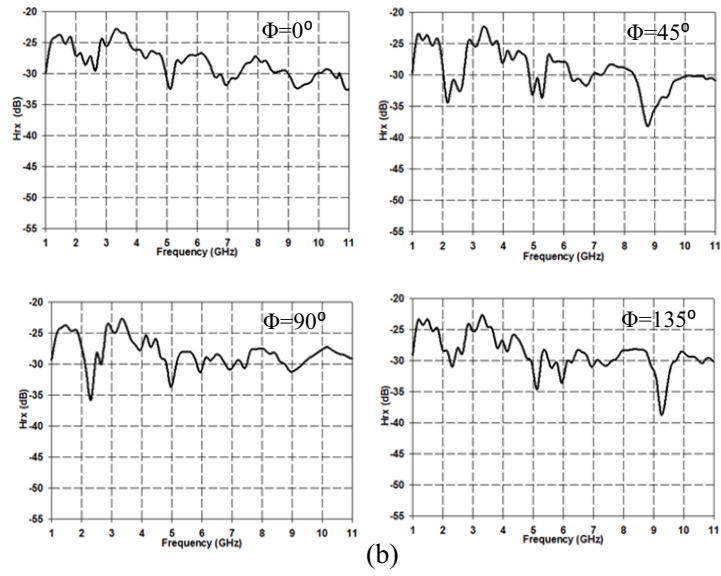
Fig. 4.34 (**contd.**)

From the transfer functions of the three antennas, measured in azimuth plane, impulse

response is obtained by inverse Fourier transform and plotted in Fig. 4.35.

113

(a)

(b)
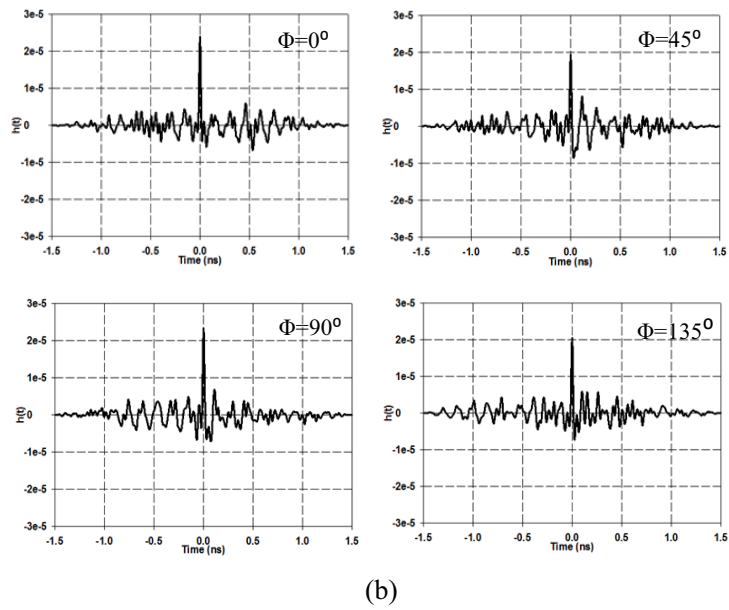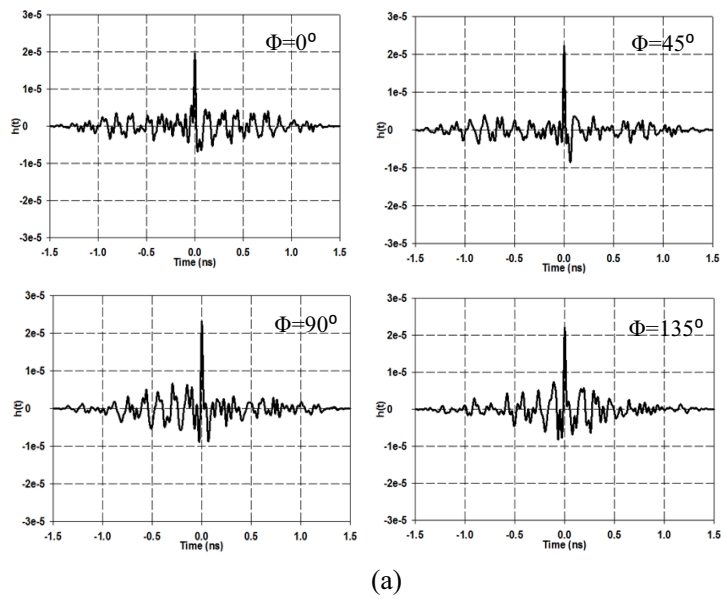
Fig. 4.35   Computed impulse response of CPW-fed slotted multiband antenna (a) Type-I (b) Type-II (c) Type-III for different angles in azimuth plane

114
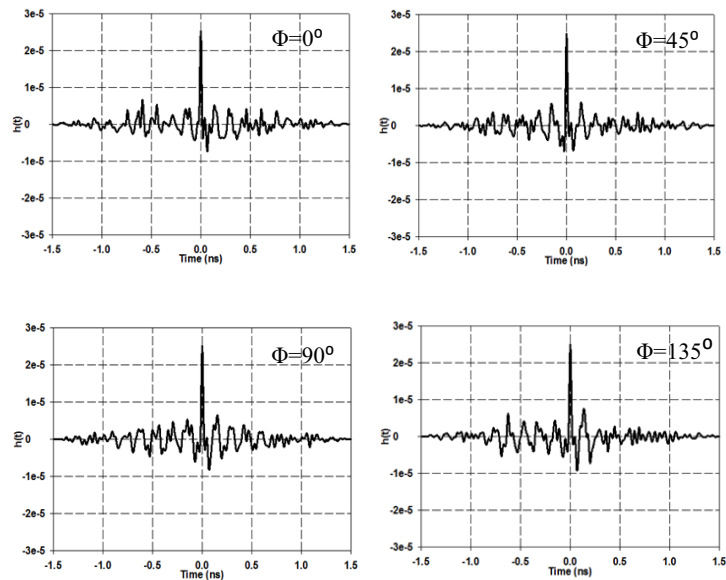
(c)

Fig. 4.35 (**contd**.)

The transfer functions of Type-I antenna show a sharp decrease between 2 and 3 GHz which is an unintended band of operation. For Type-II antenna a similar variation is seen while for Type-III antenna there is significant decrease in transfer function between 1.5-2 GHz and 2.5-3 GHz which is in agreement with the reflection characteristics, gain and efficiency plots.

For all three designs, there is a significant reduction in transfer characteristics at higher frequencies along 45^0 and 135^0 which corresponds to the distortion observed in radiation patterns at higher frequencies. From the envelope of the impulse response waveforms, full width half maxima (FWHM) and ringing are evaluated and results are shown in Table 4.7.

Table 4.7 Computed values of FWHM and ringing of the CPW-fed
slotted multiband antennas for different azimuth angles

Azimuth Angle	Type-I antenna		Type-II antenna		Type-III antenna	
	FWHM (ps)	Ringing (ps)	FWHM (ps)	Ringing (ps)	FWHM (ps)	Ringing (ps)
$\Phi = 0^\circ$	173	373	164	412	163	139
$\Phi = 45^\circ$	175	265	171	450	176	420
$\Phi = 90^\circ$	173	348	164	112	160	235
$\Phi = 135^\circ$	165	112	163	245	169	126

The impulse response shows moderate pulse dispersion and ringing in all antennas. The higher ringing in Type-II antenna can be attributed to the complicated structure created by introduction of the fractal pattern.

4.4.3 Fidelity Factor

Using a fourth order Gaussian pulse as input, the normalized pulse received for different orientations of a pair of the proposed antennas is shown in Fig. 4.36.

The mismatch between input and received pulse is higher for face to face and face to side orientations in the case of Type-I antenna. In Type-II antenna, ringing is observed in all orientations and dispersion is found to be higher than that of Type-I antenna for all orientations. This is in agreement with the higher group delay observed for this antenna. Type-III antenna has the least average ringing of the three types of antennas and input and received pulses show very good matching.
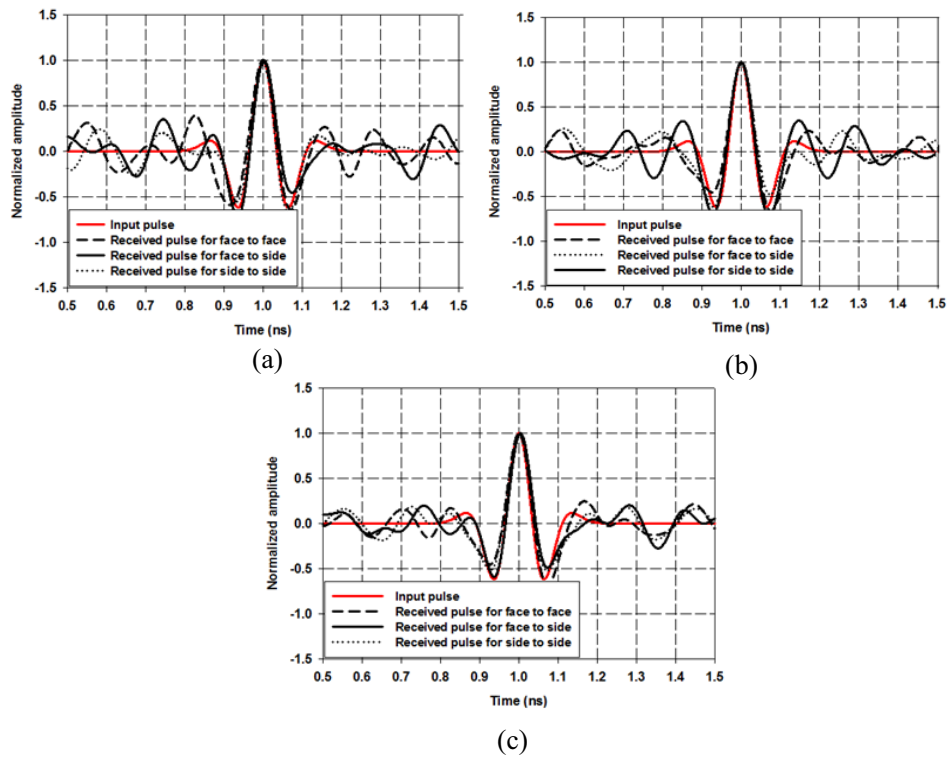
Fig. 4.36   Comparison of input and received pulses in CPW-fed slotted multiband antenna (a) Type-I (b) Type-II (c) Type-III for different orientations

To evaluate how well the input and received pulses match in different azimuth orientations, fidelity is evaluated as per Equation (2.19) and plotted in Fig. 4.37.

Fidelity factor is consistently above 90 % for Type-I antenna with a maximum value of 94.6 %. In Type-II antenna, the ringing seen in the received pulse waveforms reduces the fidelity factor at some angles and fidelity varies between 74.9 % and 93.3 %. For Type-III antenna fidelity values are better than that of Type-II antenna and has a maximum value of 94.4 %.

(a)

(b)

(c)
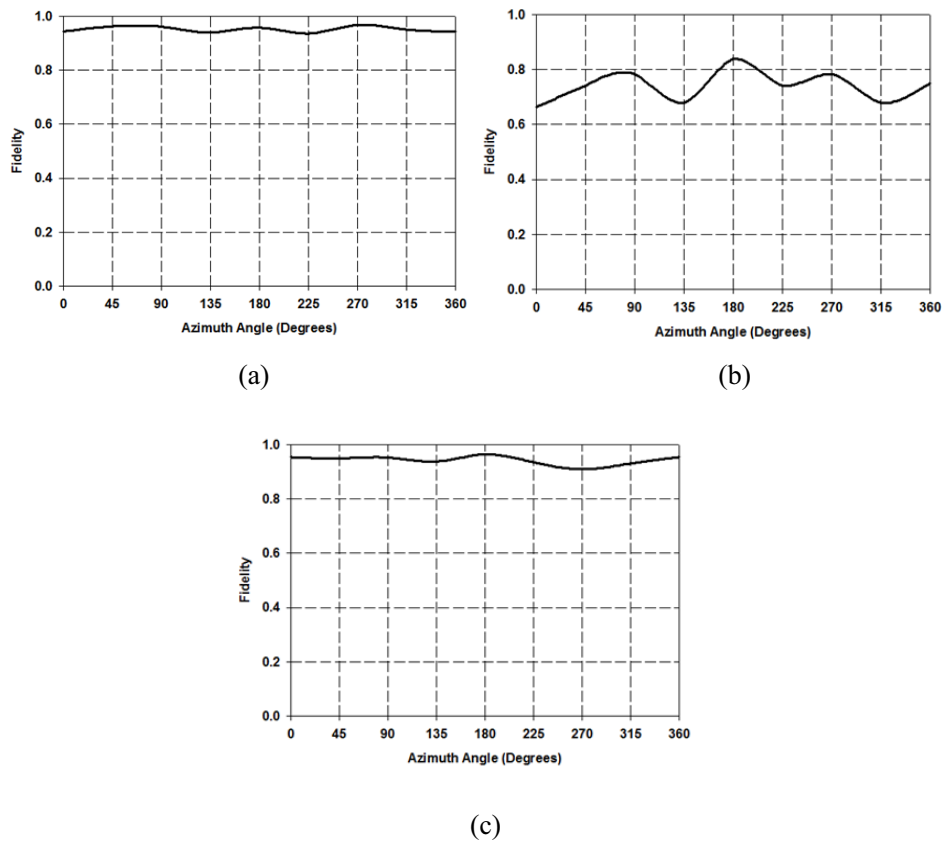
Fig. 4.37   Fidelity factor of CPW-fed slotted multiband antenna   (a)
Type-I (b) Type-II (c) Type-III in azimuth plane

4.4.4 Radiated Power Spectral Density

The emission limit is a crucial consideration for the design of UWB antennas.
According to FCC regulations, UWB systems must comply with stringent emission
limits in the frequency band of operation. Radiated power spectral densities of the
proposed antennas are evaluated as described in Section 2.6.4 and shown in Fig.
4.38. Within the frequency range from 3.1-10.6 GHz the radiated power of all

proposed antennas is compliant with both the indoor and outdoor limits imposed by the FCC which confirms their suitability for UWB applications.
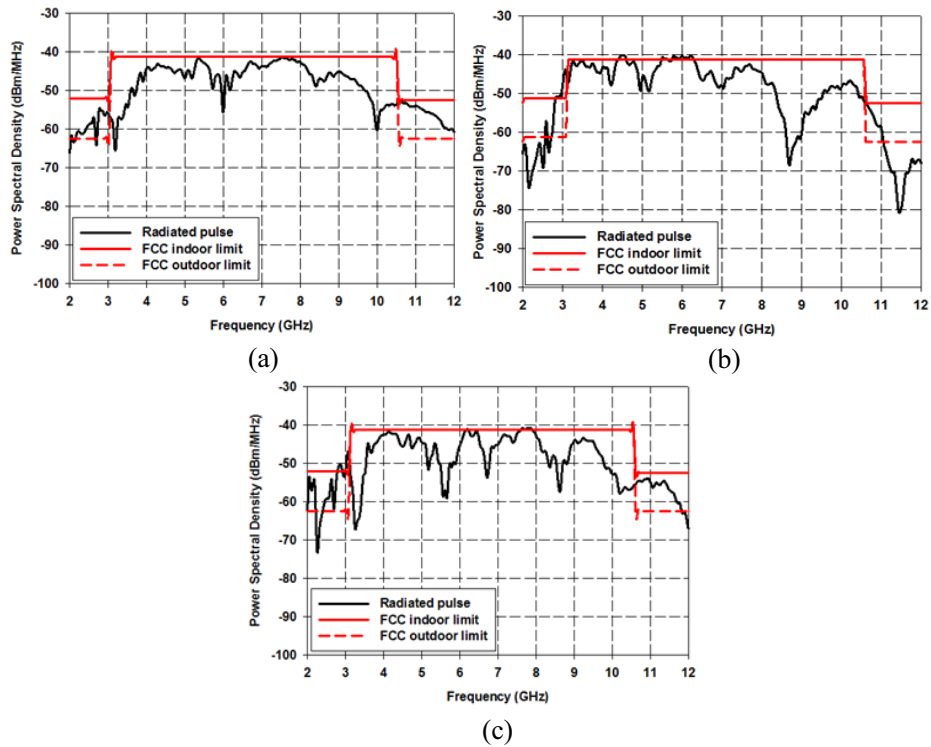
Fig. 4.38   Power spectral density of the radiated pulse for CPW-fed slotted multiband antenna (a) Type-I (b) Type-II (c) Type-III against the FCC emission mask

4.5 CHAPTER SUMMARY

This chapter presents three multiband UWB antennas developed from a conventional CPW-fed circular monopole. The circular monopole operates over the UWB range and in all antennas, lower band operation is obtained while retaining UWB characteristics.

Type-I design consists of a slot inserted in the monopole which results in a lower resonant frequency determined by the perimeter of the slot. The overall antenna size is 34×51.3 mm^2 on a substrate of permittivity 4.4. The operating bands are, 1.68-2.06 GHz and 3.27-11 GHz suitable for GSM and UWB applications. Antenna characteristics are evaluated in both frequency and time domain and the antenna is found to be a suitable candidate for UWB enabled GSM devices.

In Type-II design, a fractal pattern is used to improve impedance matching in the UWB range. The overall antenna size is the same as Type-I design and operating bands are, 1.5-2 GHz and 3.4-11 GHz suitable for GSM and UWB. Time domain analysis is also carried out and it is observed that though the fractal pattern improves impedance matching, the antenna group delay is affected. This is due to the complicated current path and this can lead to a distortion of the pulses used for communication. However, the antenna is suitable for multi-band orthogonal frequency division multiplexing (MB-OFDM) UWB systems. In such applications, the UWB range is divided into 14 subintervals each with a bandwidth of 528 MHz.

In Type-III design, a bent monopole is inserted in the space created by the slot of Type-I design, resulting in triple-band operation. The operating ranges are 1.35-1.48 GHz, 2.1-2.27 GHz and 3.14-10.8 GHz. The introduction of the bent monopole increases the perimeter of the slot which lowers the first resonance. The second resonance is controlled by the length of the monopole. The operating frequency is significantly lowered without increase in the overall size of the antenna which makes the design

compact. Frequency and time domain characteristics show that the antenna is suitable

for multiband wireless communication devices.

The proposed antennas are compared with some of the recently reported multiband

antennas developed using similar techniques outlined in this chapter and summarized

in Table. 4.8.

Table 4.8   Comparison of proposed antennas with existing slotted multiband antennas

Antenna	No. of operating bands	Lowest operating frequency	Size(mm³)	ϵ_r	Peak Gain
Mishra *et al*. (2011)	3	2.18 GHz	24×50×1.6	4.4	1-4 dBi
Bod *et al*. (2012)	4	1.52 GHz	25×28×0.8	4.4	-6-4 dBi
Kumar *et al*. (2012)	1	2.25 GHz	55×62×1.53	4.3	-
Kushwaha and Kumar (2013)	1	2.2 GHz	77×55×1.6	4.4	10 dBi
Awad and Abdelazeez (2013)	2	2.3 GHz	30×30×1.6	4.4	2-4.8 dBi
Naser and Dib (2016)	2	1.84 GHz	25×38×1.6	4.4	1-10 dBi
Proposed antenna Type-I	2	1.68 GHz	34×51.3×1.6	4.4	2.82-7.35 dBi
Proposed antenna Type-II	2	1.5 GHz	34×51.3×1.6	4.4	2.82-6.5 dBi
Proposed antenna Type-III	3	1.35 GHz	34×51.3×1.6	4.4	0.2-8.17 dBi

Mishra *et al.* (2011) achieved Bluetooth operation in addition to UWB band and the wideband is converted to dual-band by introducing band notch characteristics. Antenna size is smaller, but operating bandwidth is lower than proposed antennas. The antenna proposed by Bod *et al.* (2012) is very compact in size and covers three bands in addition to UWB band. However, gain in the lowest band is very low and the antenna does not have the advantage of CPW-feed as in the proposed geometries. The antennas reported in Kumar *et al.* (2012) and Kushwaha and Kumar (2013) are larger than the proposed antennas and cover a single wide frequency band with a lowest frequency of operation of approximately 2.2 GHz. The antenna proposed by Awad and Abdelazeez (2013), is of smaller size than the proposed structures but lowest frequency of operation is much higher. Naser and Dib (2016) proposed an ultrawideband antenna with operating frequency 2.9-50 GHz. The antenna incorporates a meandered strip and the length of the strip is altered using a PIN diode for operation in an additional Bluetooth or GSM band. While the authors state that the gain is as high as 10 dBi, this is at a frequency beyond the UWB band. Within the UWB range, gain is comparable to that of the proposed antennas.

Compared to the CPW-fed fractal multiband antenna proposed in Chapter 3, the antennas proposed in this chapter operate over a wider range of frequencies. The radiation characteristics and the compact size make the proposed antennas suitable for multiband wireless communication devices including MB-OFDM UWB systems. To make the antennas more compact, spiral monopoles are investigated as described next.

Chapter 5

CPW-FED SPIRAL MULTIBAND ANTENNAS

Frequency independent antennas are antennas in which radiation pattern, impedance and polarization remain unchanged over a large bandwidth. They exist in several configurations such as equiangular, sinuous, Archimedean, etc. Of these, the equiangular spiral antenna was introduced by Rumsey in the 1950s. Its shape can be described by angles and lowest frequency of operation occurs when the total arm length is comparable to the wavelength (Balanis, 2007). The spiral can have different geometrical arrangements with a single arm or with two arms. The two arm spiral antenna is popular for its wide bandwidth and circular polarization. However, to maintain symmetrical characteristics, the antenna must be fed by an electrically and geometrically balanced line and thus a wideband balun is often required for impedance matching (Elmansouri and Filipovic, 2011; Chen and Huff, 2011; Seong and Park, 2012; Shih and Behdad, 2014).

The single arm spiral has the advantage over a two arm spiral in that impedance matching to a 50 Ω line is possible without the need for a balun circuit (Nakano *et al*., 2010; Gong *et al*., 2013). A brief account of some of the research carried out on spiral antennas for wideband and multiband applications is presented here.

Valleau *et al*. (2014) proposed the use of stacked pre-fractal metallic rings for miniaturization of the Archimedian spiral antenna. Rings with a modified Von Koch profile are electromagnetically coupled to the spiral antennas to achieve a decrease in the lowest operating frequency while keeping the physical size of the antenna

unchanged. The rings are fabricated on a paper substrate with ink jet printing technology.

A coplanar waveguide (CPW)-fed spiral antenna for wideband applications is presented by Ghassemi *et al*. (2011). The antenna is fabricated on a 0.508 mm thick substrate of relative permittivity 10.2 and loss tangent 0.0001. The high relative permittivity of the substrate reduces the antenna size to 9×7.5 mm^2. The antenna has a relatively constant gain and $S_{11} \leq$ -10 dB within a wide bandwidth from 11.5-17.5 GHz.

A CPW-fed frequency reconfigurable two arm Archimedean spiral antenna is proposed by Dahalan *et al*. (2013). The spiral has four turns and can operate over a wide frequency bandwidth. The wideband spiral antenna is then reconfigured by disturbing the surface at both sides of the CPW-fed slot using a pair of meandered slotline resonators. Two PIN diode switches are used to achieve frequency reconfiguration and switch the wideband mode to a 5.8 GHz narrowband mode. The overall size of the spiral antenna is 60×69 mm^2 on a substrate of thickness 1.6 mm, relative permittivity 4.6 and loss tangent 0.019.

Zhang *et al*. (2013) introduced a monopole antenna in which two spiral ring strips are inserted into the microstrip line on different layers and connected through via hole. Due to the introduction of the spiral ring strips, the direction of surface currents on the spiral ring strips changes with the alteration of spiral structure and their effects on the radiation pattern are reduced. The antenna has an overall size of 28×20 mm^2 on a substrate of thickness 1 mm and relative permittivity 2.65 and operates in wireless local

area network (WLAN)/worldwide interoperability for microwave access (WiMAX) (2.4/3.5/5.2 GHz) bands.

A dual-band single arm spiral antenna is presented by Chiu and Chuang (2009). A broadband spiral antenna fed by coaxial line is first designed to cover LS and WiMAX bands. Then, a finite frequency selective surface is added to the antenna to create a dual-band characteristic in which the main beams corresponding to both bands are widely separated. This makes the antenna suitable for operation in satellite and ground based communication simultaneously. The spiral antenna is printed on the top surface of a substrate of thickness 1.6 mm and a relative permittivity of 4.4 and has an overall size of 52×44 mm^2.

Wan *et al*. (2013) proposed a multiband monopole antenna loaded with spiral ring resonators. The antenna structure is very similar to the antenna of Zhang *et al*. (2013) but uses CPW feed. The antenna size is 27.5×20 mm^2 on a substrate of relative permittivity 2.55, loss tangent 0.0006 and thickness 1 mm.

Wang *et al*. (2010) presented a miniaturized compound spiral antenna for wideband operation from 1.6 to 10 GHz. In comparison with a conventional equiangular spiral antenna of the same size, the proposed antenna has a significantly lower operating frequency, resulting in 44.8 % reduction in size.

A CPW-fed two arm Archimedean spiral slot antenna is investigated by Mashaal *et al*. (2013). The antenna has wide input impedance bandwidth with circular polarization and has an overall size of 74×62 mm^2 on a substrate of relative permittivity 4.6 and

thickness 1.6 mm. The antenna also has the advantage that it does not require any external impedance matching network or balun, which makes fabrication easy.

From the literature survey carried out, it is seen that most of the spiral antennas developed, can be used for operation in multiple narrow bands or for wideband operation. Spiral antennas offer the advantages of circular polarization and compact designs and several structures have been developed that exploit these features.

Two spiral antenna designs which can be used for multiband operation including UWB applications are proposed in this chapter. The first antenna is suitable for operation in global system for mobile (GSM) and ultrawideband (UWB) bands. By using shorting strips between the arms of the spiral, the lower frequency of operation can be reduced without increase in the overall size of the antenna. This makes the design compact and the antenna is suitable for wireless medical telemetry service (WMTS) and UWB applications.

5.1 DUAL-BAND SPIRAL MONOPOLE ANTENNA (TYPE-I)

5.1.1 Antenna Geometry

The spiral is asymmetrically oriented with respect to the feed line such that its outermost turn mimics the outer edge of a circular monopole. This results in wideband operation and the lower limit of the band is determined by outer diameter, D. The spiral orientation is such that, the axis from outer end of the spiral to the center is at an angle $\alpha = 90^0$ with respect to the feed line. This ensures wideband operation over the UWB band. The longer arm of the spiral has a length, SL_1 and behaves as a ring resonator while the shorter arm has a length, SL_2. This orientation also results in a lower operating

band with resonance frequency determined by length SL_1 of the ring resonator. The schematic of the proposed CPW-fed spiral multiband antenna Type-I is shown in Fig. 5.1.
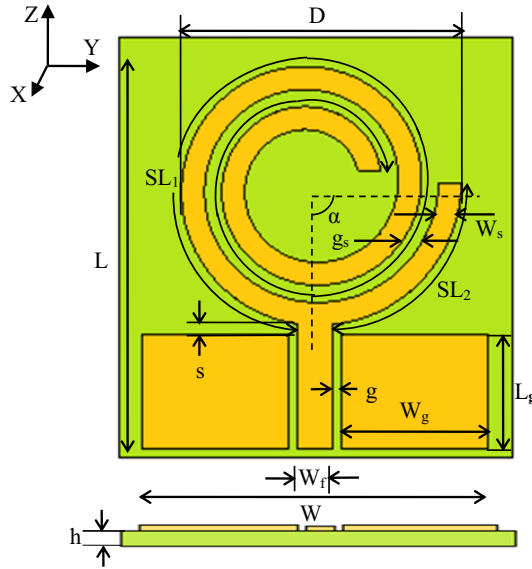
Fig. 5.1 Geometry of dual-band spiral monopole antenna (Type-I)
with optimized dimensions W = 27.6 mm, L = 28.3 mm,
SL_1 = 97 mm, SL_2 = 18.2 mm, L_g = 10 mm, W_g = 12 mm,
W_f = 3 mm, g = 0.3 mm, s = 0.3 mm, D = 21 mm, α = 90°,
g_s = 1.5 mm and W_s = 2 mm for ϵ_r = 4.4, h = 1.6 mm

The substrate used is of relative permittivity ϵ_r = 4.4, loss tangent tan δ = 0.02 and thickness h = 1.6 mm. The spiral consists of two complete turns of metal strips of width, W_s with uniform spacing, g_s between the turns. The 50 Ω CPW-feed line has a width, W_f and is spaced at a distance, g from the ground plane of length, L_g and width, W_g on both sides. The monopole is spaced at a distance, s from the ground plane and the overall size of the antenna is 27.6×28.3 mm².

5.1.2 Parametric Analysis of Dual-band Spiral Monopole Antenna (Type-I)

For a circular monopole, the diameter approximately corresponds to quarter wavelength at the fundamental resonant frequency (Si and Lv, 2008). Since the proposed spiral is designed to mimic the outer edge of a circular monopole, the outermost turn of the spiral is set to a diameter of 21 mm which is approximately a quarter wavelength of 2.45 GHz. The width, W_s of the spiral strip and spacing, g_s between the turns of the spiral are set to 2 mm and 1 mm respectively (Chiu and Chuang, 2009). With these dimensions of the spiral monopole, the orientation of the spiral is first varied.

Effect of spiral monopole orientation, α

The spiral monopole antenna is intended to operate in GSM band and UWB range and its orientation with respect to the feed line determines operating characteristics. To study its effect, the spiral is rotated and results are shown in Fig. 5.2.
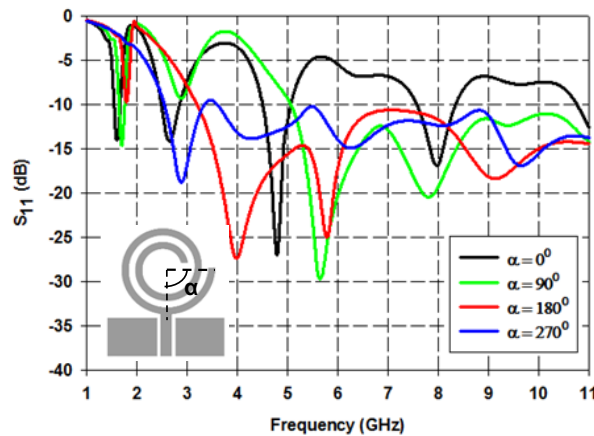
Fig. 5.2   Simulated S_{11} vs frequency for varying spiral resonator orientation α with $\epsilon_r = 4.4$, h = 1.6 mm, $L_g = 9$ mm, $W_g = 13$ mm, $W_f = 3$ mm, g = 0.3 mm, s = 0.3 mm, D = 21 mm, $W_s = 2$ mm and $g_s = 1$ mm

128

For the orientation with $\alpha = 0^{\circ}$, the feed line meets the outer end of the spiral and quad-band impedance characteristics are seen. The spiral arm has a length of 114 mm which corresponds to one wavelength of the first resonance at 1.6 GHz. When $\alpha = 90^{\circ}$, the lower portion of the spiral near the feed line is similar to that of a CPW-fed circular monopole and this results in UWB operation. The portion of the monopole that resembles a spiral ring resonator has a length 97 mm and corresponds to one wavelength of 1.8 GHz. At $\alpha = 180^{\circ}$, two resonances can be achieved in addition to ultrawideband characteristics but UWB band is not completely covered. When $\alpha = 270^{\circ}$, the lower resonance occurs at 1.7 GHz and sufficient matching is obtained throughout UWB range.

From the orientation study, the geometry with $\alpha = 90^{\circ}$ is chosen as it provides impedance matching in the desired GSM and UWB bands.

Effect of ground plane length, L_g

Since the ground plane plays a crucial role in the wideband response of the antenna, the parametric analysis for the dimensions of the ground plane are carried out and reflection coefficient plots for varying ground plane length are shown in Fig. 5.3.

The spiral arm is designed to have a length SL_1 that corresponds to one complete wavelength λ_1 at 1.8 GHz. As ground length L_g is increased, impedance matching in the UWB range improves and the lower limit of the UWB band shifts to lower frequencies. To maintain a compact size for the antenna, $L_g = 10$ mm is chosen as the optimum value. This is equivalent to $0.332\lambda_c$ where λ_c is the guide wavelength corresponding to the center of the UWB band.

129
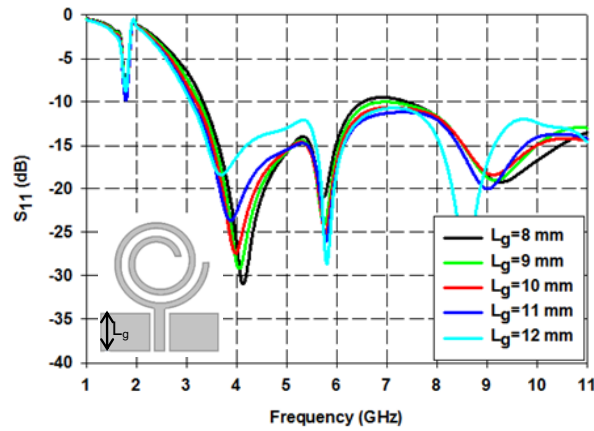
Fig. 5.3   Simulated S_{11} vs frequency of dual-band spiral monopole antenna (Type-I) for varying L_g with $\epsilon_r = 4.4$, h = 1.6 mm, $SL_1 = 97$ mm, $SL_2 = 18.2$ mm, $W_g = 12.5$ mm, $W_f = 3$ mm, g = 0.3 mm, s = 0.3 mm, D = 21 mm, $W_s = 2$ mm and $g_s = 1$ mm

Effect of ground plane width, W_g

The parametric analysis for width of ground plane is shown in Fig. 5.4.
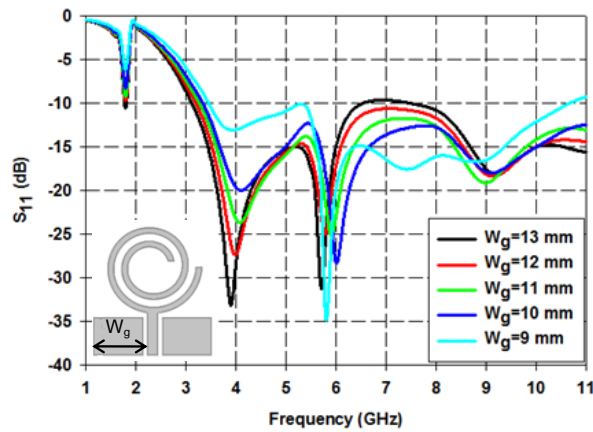
Fig. 5.4   Simulated S_{11} vs frequency of dual-band spiral monopole antenna (Type-I) for varying W_g with $\epsilon_r = 4.4$, h = 1.6 mm, $SL_1 = 97$ mm, $SL_2 = 18.2$ mm, $L_g = 10$ mm, $W_f = 3$ mm, g = 0.3 mm, s = 0.3 mm, D = 21 mm, $W_s = 2$ mm and $g_s = 1$ mm

130

When W_g is varied, it is seen that as width reduces, impedance matching in the UWB band improves but lower limit of the band increases. From the exhaustive analysis, W_g = 12 mm which is $0.399\lambda_c$ is chosen as the optimum value.

Effect of spiral resonator arm length, SL_1

The parametric analysis for length of the spiral resonator arm SL_1 is shown in Fig. 5.5 and it is seen that as length increases the lower band resonance shifts to lower frequencies. This confirms that the spiral resonator arm length predominantly controls the first resonance.
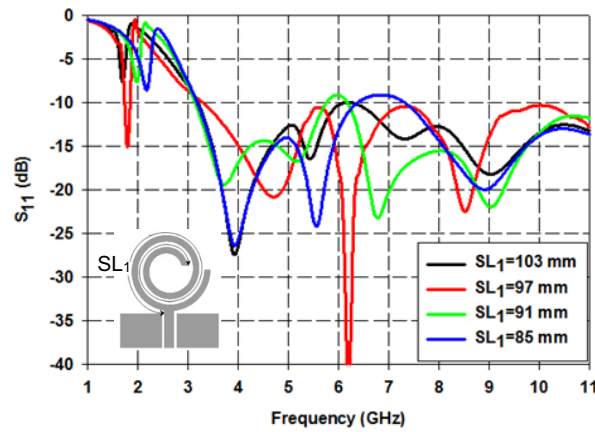
Fig. 5.5   Simulated S_{11} vs frequency of dual-band spiral monopole antenna (Type-I) for varying spiral resonator length SL_1 with ϵ_r = 4.4, h = 1.6 mm, SL_2 = 18.2 mm, L_g = 10 mm, W_g = 12 mm, W_f = 3 mm, g = 0.3 mm, s = 0.3 mm, D = 21 mm, W_s = 2 mm and g_s = 1 mm

For SL_1 = 97 mm, the inner turn of the spiral has a length 57 mm. This length of the inner turn corresponds to a half wavelength of 1.8 GHz and so a resonance is achieved at the intended GSM band with impedance matching throughout the UWB band. While

the outer turn of the spiral contributes to UWB band, the inner turn creates the lower resonance.

Effect of spiral resonator width, W_s

Next, the parametric analysis for the width of the spiral resonator is carried out and the variation of reflection coefficient of the antenna is shown in Fig. 5.6.
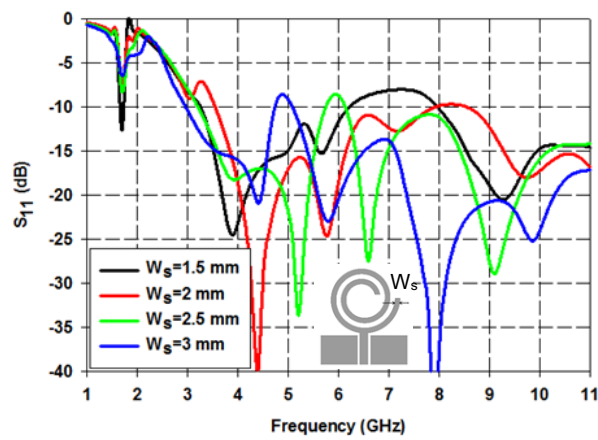
Fig. 5.6   Simulated S_{11} vs frequency of dual-band spiral monopole antenna (Type-I) for varying spiral resonator strip width W_s with $\epsilon_r = 4.4$, h = 1.6 mm, $SL_1 = 97$ mm, $SL_2 = 18.2$ mm, $L_g = 10$ mm, $W_g = 12$ mm, $W_f = 3$ mm, g = 0.3 mm, s = 0.3 mm, D = 21 mm, and $g_s = 1$ mm

The antenna is intended to operate in UWB band as well as GSM band and from the figure it is clear that for $W_s = 1.5$ mm, the antenna resonates in both these intended bands but matching in the UWB band is poor. Increasing W_s improves impedance matching in the UWB range as it is more inductive in nature.

From the analysis, $W_s = 2$ mm is chosen as the optimum value and this dimension equates to $0.066\lambda_c$ as validated in Table 5.1 of Section 5.1.4.

132

Effect of spacing between spiral resonator turns, g_s

Setting W_s = 2 mm, the spacing between the turns of the spiral strip is varied and corresponding variation in reflection coefficient is shown in Fig. 5.7.
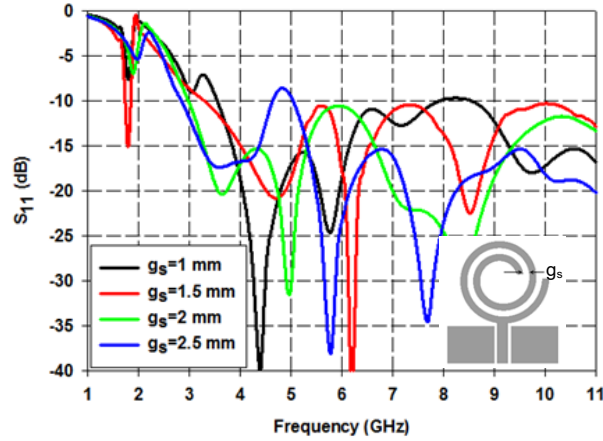
Fig. 5.7   Simulated S_{11} vs frequency of dual-band spiral monopole antenna (Type-I) for varying spiral resonator strip gap g_s with ϵ_r = 4.4, h = 1.6 mm, SL_1 = 97 mm, SL_2 = 18.2 mm, L_g = 10 mm, W_g = 12 mm, W_f = 3 mm, g = 0.3 mm, s = 0.3 mm, D = 21 mm and W_s = 2 mm

As gap increases, capacitive reactance at higher frequencies increases and the real part of the impedance is around 50 Ω while imaginary part is close to 0 Ω. At g_s = 1.5 mm, which is 0.013λ_{g1}, sufficient matching is obtained in GSM band as well as throughout the UWB band. So, this value is chosen as optimum.

5.1.3 Surface Current Distribution of Dual-band Spiral Monopole Antenna (Type-I)

The resonance mechanism of the antenna can be analyzed by examining the surface current distribution of the Type-I antenna as shown in Fig. 5.8.

133
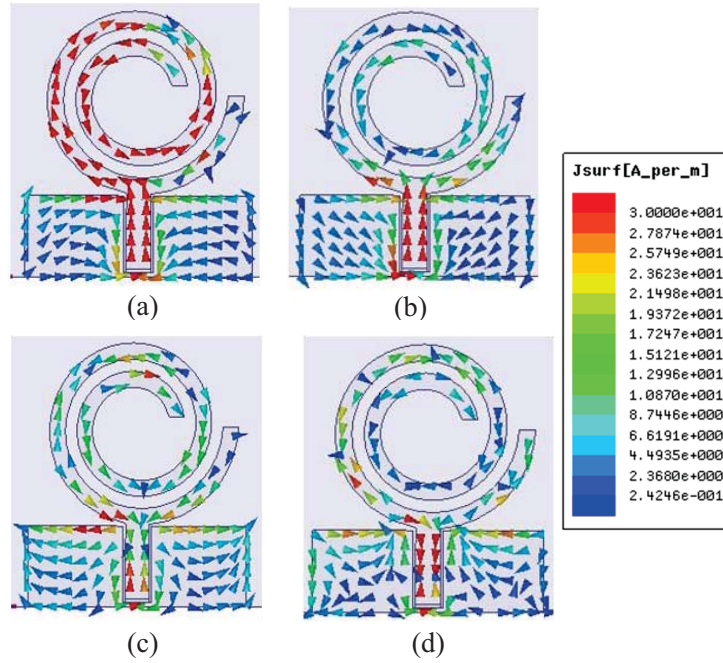
Fig. 5.8   Surface current distribution of dual-band spiral monopole antenna (Type-I) at (a) 1.8 GHz (b) 3.3 GHz (c) 6.2 GHz (d) 10.6 GHz with ϵ_r = 4.4, h = 1.6 mm, SL_1 = 97 mm, SL_2 = 18.2 mm, L_g = 10 mm, W_g = 12 mm, W_f = 3 mm, g = 0.3 mm, s = 0.3 mm, g_s = 1.5 mm, D = 21 mm and W_s = 2 mm

At 1.8 GHz, one half wave variation is seen along the inner turn of the spiral ring resonator SL_1. This shows that the longer arm of the spiral ring resonator is responsible for the first resonance frequency. At 3.1 GHz, current is mainly concentrated on the lower part of the spiral similar to the distribution on a UWB circular monopole (Ray, 2008).

At higher frequencies, the distribution on the spiral and ground plane shows the excitation of higher order modes but it is mainly the outermost turn of the spiral that contributes to UWB operation.

134

5.1.4 Design Equations of Dual-band Spiral Monopole Antenna (Type-I)

From the parametric analysis carried out in Section 5.1.2, the design equations are formulated and the procedure for the design of the antenna is as listed:

1) Design a CPW-feed line of 50 Ω impedance with width, W_f and gap, g from the ground plane. Calculate ϵ_{reff} using $\epsilon_{reff} = (\epsilon_r + 2) / 3$ where ϵ_{reff} is the effective permittivity of the substrate.

2) The length of the ground plane on either side of the feed line is calculated using

$$L_g = 0.332\lambda_c \qquad (5.1)$$

where λ_c is the guide wavelength corresponding to the center of the UWB band.

3) The width of the ground plane is calculated as

$$W_g = 0.399\lambda_c \qquad (5.2)$$

4) Design a spiral resonator with outer diameter

$$D = 0.25\lambda_m \qquad (5.3)$$

where λ_m is the guide wavelength corresponding to average frequency, f_m of desired lower resonance and UWB lower limit.

5) The gap, s between monopole and ground is set to a value equal to gap between feed line and ground plane, g.

5) The spiral resonator width is designed as

$$W_s = 0.066\lambda_c \qquad (5.4)$$

6) Gap between the turns of the spiral is designed as

$$g_s = 0.013\lambda_{g1} \qquad (5.5)$$

where λ_{g1} is the guide wavelength corresponding to the lower band resonance.

7) The spiral resonator's orientation with respect to the feed line is such that the arm of length SL_2 resembles a quarter of the outer edge of a circular monopole. The longer arm is designed using the regression equation

$$SL_1 \approx -28.12f_1 - 6.02\epsilon_r - 1.91h + 178.43 \qquad (5.6)$$

where f_1 is the resonance frequency of the lower band. This equation is valid for substrates with $2.2 < \epsilon_r < 6.15$ and 0.8 mm $< h <$ 2 mm for the frequency range 1.6 GHz $< f_1 <$ 2.5 GHz.

The reflection characteristics obtained from the simulation in HFSS™ using the design values listed in Table 5.1 are plotted in Fig. 5.9.

Table 5.1   Dual-band spiral monopole antenna (Type-I) parameters for different substrates obtained from design equations

Parameter (mm)	Substrate			
	1	2	3	4
	Rogers 5880 $\epsilon_r = 2.2$	Rogers RO4003 $\epsilon_r = 3.55$	FR-4 Epoxy $\epsilon_r = 4.4$	Rogers RO3006 $\epsilon_r = 6.15$
h	1.57	0.8	1.6	1.28
W_f	4	6	3	2.58
g	0.17	0.3	0.3	0.45
L_g	12.3	10.7	9.96	8.82
W_g	14.7	12.8	11.99	10.6
s	0.17	0.3	0.3	0.45
W_s	2.44	2.13	1.98	1.76
g_s	1.83	1.59	1.48	1.32
SL_1	111.6	104.9	98.3	88.34
SL_2	20.62	19.15	18	15.5
D	25.9	22.5	20.9	18.6

Fig. 5.9   Simulated reflection characteristics of dual-band spiral monopole antenna (Type-I) on different substrates

136

The simulated frequencies are compared with the desired frequencies of 1.8 GHz and 3.1 GHz as shown in Table. 5.2.

Table 5.2   % Error in simulated frequency of dual-band spiral monopole antenna (Type-I) for different dielectric substrates at $f_l = 1.8$ GHz and $f_L = 3.1$ GHz

Substrate	Simulated Frequency (GHz)		Error (%)	
	f_l	f_L	f_l	f_L
Rogers 5880 ($\epsilon_r = 2.2$, h = 1.57 mm)	1.77	2.95	1.66	4.8
Rogers RO4003 ($\epsilon_r = 3.55$, h = 0.8 mm)	1.89	3.25	5	4.8
FR-4 Epoxy ($\epsilon_r = 4.4$, h = 1.6 mm)	1.81	3.25	0.55	4.8
Rogers RO3006 ($\epsilon_r = 6.15$, h = 1.28 mm)	1.82	3.2	1.11	3.2

5.1.5 Reflection Characteristics of Dual-band Spiral Monopole Antenna (Type-I)

The antenna is fabricated on a substrate of permittivity 4.4 and thickness 1.6 mm as shown in Fig. 5.10 (a). Testing is done using Agilent programmable network analyzer (PNA) E8362B and results are shown in Fig. 5.10 (b).

(a)   (b)
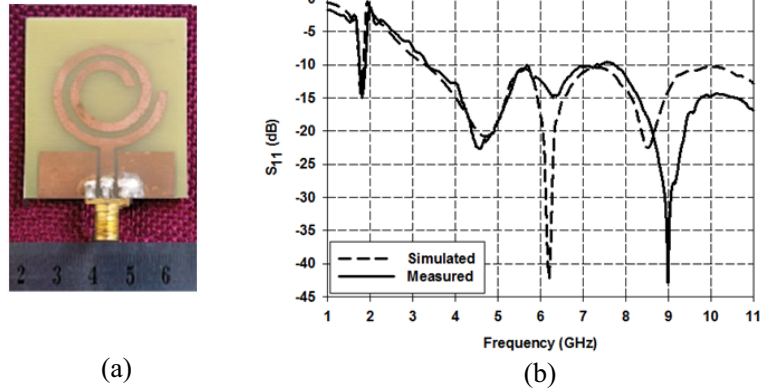
Fig. 5.10   Fabricated prototype (b) Simulated and measured reflection characteristics of dual-band spiral monopole antenna (Type-I) with $\epsilon_r = 4.4$, h = 1.6 mm, $SL_1 = 97$ mm, $SL_2 = 18.2$ mm, $L_g = 10$ mm, $W_g = 12$ mm, $W_f = 3$ mm, g = 0.3 mm, s = 0.3 mm, $g_s = 1.5$ mm, $r_s = 9$ mm and $W_s = 2$ mm

The readings show very good agreement till 6 GHz and beyond this there is some mismatch in readings. This could be due to the inherent losses of the FR-4 substrate and SMA connector. However, the measured readings show reasonable matching from 1.75-1.92 GHz and 3.3-11 GHz which makes the antenna suitable for GSM and UWB applications.

5.1.6 Radiation Pattern of Dual-band Spiral Monopole Antenna (Type-I)

Simulated three dimensional radiation patterns at various operating frequencies are plotted in Fig. 5.11.
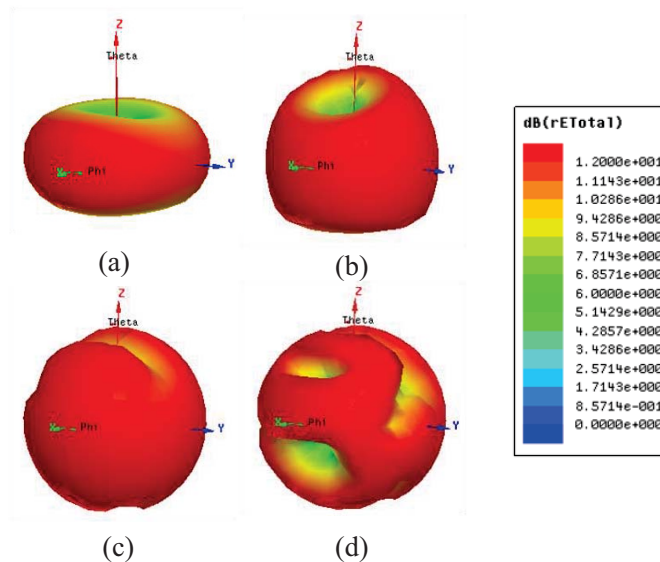
Fig. 5.11   Simulated 3D radiation patterns of the dual-band spiral monopole antenna (Type-I) at the resonance frequencies (a) 1.8 GHz (b) 3.3 GHz (c) 6.2 GHz (d) 10.6 GHz with $\epsilon_r = 4.4$, h = 1.6 mm, $SL_1 = 97$ mm, $SL_2 = 18.2$ mm, $L_g = 10$ mm, $W_g = 12$ mm, $W_f = 3$ mm, g = 0.3 mm, s = 0.3 mm, $g_s = 1.5$ mm, D = 21 mm and $W_s = 2$ mm

modes. The two dimensional patterns in the E-plane (X-Z) and H-plane (X-Y) are shown in Fig. 5.12.
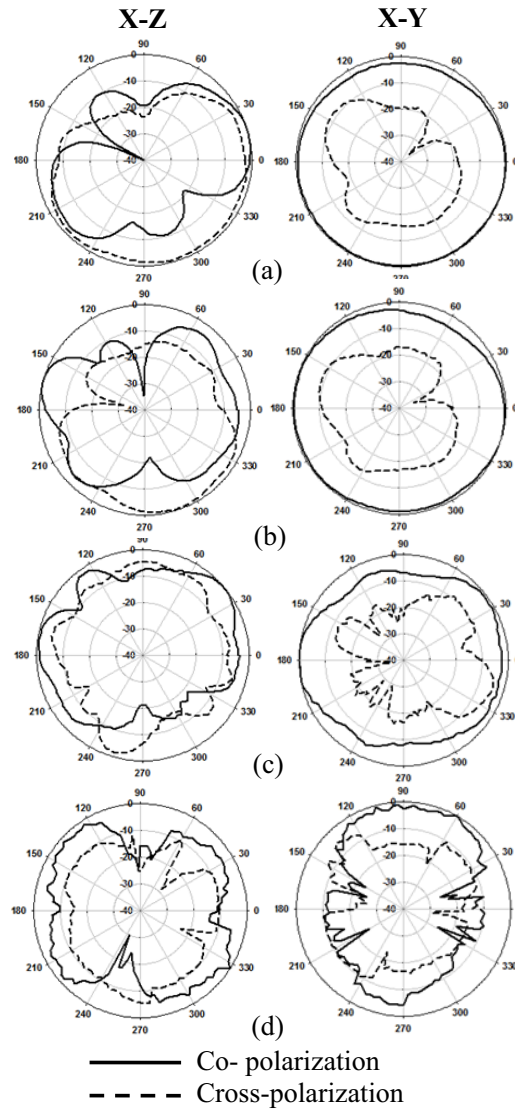
Fig. 5.12   Normalized 2D radiation pattern of dual-band spiral monopole antenna (Type-I) measured at the resonance frequencies (a) 1.8 GHz (b) 3.3 GHz (c) 6.2 GHz (d) 10.6 GHz with $\epsilon_r = 4.4$, h = 1.6 mm, $SL_1 = 97$ mm, $SL_2 = 18.2$ mm, $L_g = 10$ mm, $W_g = 12$ mm, $W_f = 3$ mm, g = 0.3 mm, s = 0.3 mm, $g_s = 1.5$ mm, D = 21 mm and $W_s = 2$ mm

In the 2D patterns also, the antenna has stable radiation patterns throughout the bands of interest with non-directional pattern in the X-Y plane. At higher frequencies, the shape is somewhat distorted due to the excitation of higher modes as seen in the surface current distribution of Fig.5.8 (d). The cross polarization levels are good throughout the operating bands and show better levels than that of the antennas presented in earlier chapters.

5.1.7 Gain and Efficiency of Dual-band Spiral Monopole Antenna (Type-I)

The peak gain and efficiency of the antenna are measured using the Two Antenna and Wheeler Cap methods outlined in Chapter 2 and their variation with frequency is plotted in Fig. 5.13.

(a)   (b)
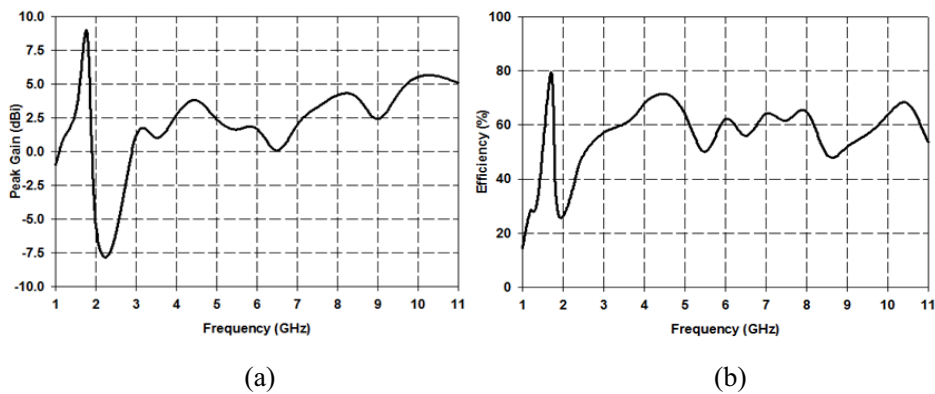
Fig. 5.13   (a) Peak gain and (b) Efficiency of dual-band spiral monopole antenna (Type-I) with $\epsilon_r = 4.4$, h = 1.6 mm, SL_1 = 97 mm, SL_2 = 18.2 mm, L_g = 10 mm, W_g = 12 mm, W_f = 3 mm, g = 0.3 mm, s = 0.3 mm, g_s = 1.5 mm, D = 21 mm and W_s = 2 mm

The antenna has a peak gain of 8.36 dBi at 1.8 GHz and 5.85 dBi in the UWB range. The efficiency plot shows a similar variation with a maximum of 78 % and 72 % in the GSM and UWB bands respectively.

The operating frequency of the antenna can be lowered without increasing the overall size of the antenna by the use of shorting strips between the spiral arms. The strips alter the current path on the antenna so as to extend the resonator length which in turn, lowers the frequency of operation. A second dual band monopole antenna with lower frequency of operation is proposed and details are presented next.

5.2 DUAL-BAND SPIRAL MONOPOLE ANTENNA WITH SHORTING STRIPS (TYPE-II)

The geometry of CPW-fed spiral multiband antenna Type-I suitable for GSM is modified to lower the operation frequency to 1.4 GHz without increase in overall size of the antenna. This Type-II antenna is suited for WMTS and UWB applications.

5.2.1 Antenna Geometry

A dual-band antenna suitable for WMTS (1.395-1.4 GHz) and UWB applications is proposed and the geometry is shown in Fig. 5.14.

Two short circuit strips are used between the arms of the spiral in the modified structure. One strip is placed at a distance, P_1 along the length of the spiral monopole and it has a thickness, t. The position of this shorting strip determines the resonance frequency of the lower band. To improve the matching in the UWB band, a second shorting strip of same thickness is placed at a distance, P_2 from the first shorting strip. All other dimensions of the antenna are the same as that of Type-I geometry.
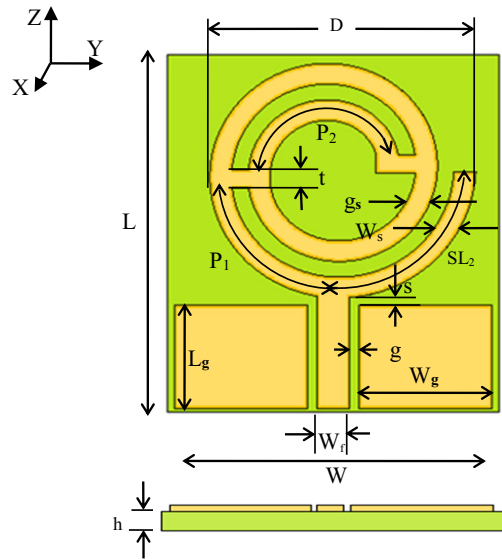
Fig. 5.14 Geometry of dual-band spiral monopole antenna with shorting strips (Type-II) with W = 27.6 mm, L = 28.3 mm, SL_1 = 97 mm, SL_2 = 18.2 mm, L_g = 10 mm, W_g = 12 mm, W_f = 3 mm, g = 0.3 mm, s = 0.3 mm, g_s = 1.5 mm, W_s = 2 mm, D = 21 mm, P_1 = 17 mm, P_2 = 18 mm and t = 2 mm for ϵ_r = 4.4, h = 1.6 mm

5.2.2 Parametric Analysis of Dual-band Spiral Monopole Antenna with Shorting Strips (Type-II)

In the parametric analysis carried out in Section 5.1.2, the spiral monopole and ground plane dimensions are optimized for UWB operation. Since the main modification in Type-II design is the introduction of the shorting strips, a parametric analysis on the position and width of the strips is carried out to study their effect on antenna performance.

Effect of distance of first shorting strip, P_1

First, only one short circuit strip is placed between the arms of the spiral and the reflection characteristics for varying positions of the strip are shown in Fig. 5.15.

For varying positions of the shorting strip, there is significant mismatch in the UWB range. This is because the strip alters the current on the outermost turn of the spiral that is responsible for UWB band. As the shorting strip is placed higher, the resonance frequency of the lower band shifts to the lower frequency side. The shorting strip creates a current path such that an extended resonator length is obtained compared to the resonator length of Type-I antenna. This is seen in the surface current distributions presented in Fig. 5.8 (a) and Fig. 5.18 (a).
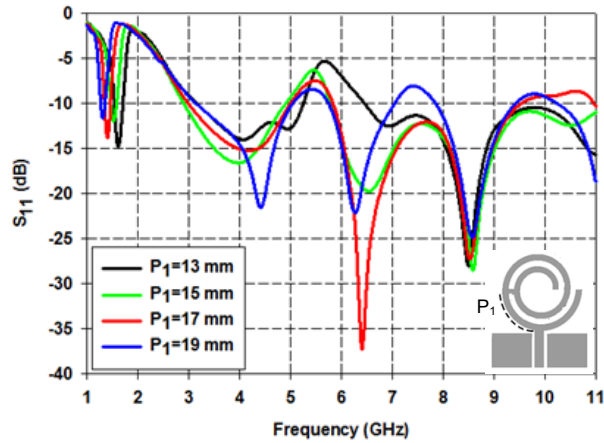
Fig. 5.15   Simulated S_{11} vs frequency of dual-band spiral monopole antenna with shorting strips (Type-II) for varying P_1 with $\epsilon_r = 4.4$, h = 1.6 mm, $SL_1 = 97$ mm, $SL_2 = 18.2$ mm, $L_g = 10$ mm, $W_g = 12$ mm, $W_f = 3$ mm, g = 0.3 mm, s = 0.3 mm, $g_s = 1.5$ mm, $W_s = 2$ mm, D = 21 mm and t = 2 mm

At $P_1 = 17$ mm, $S_{11} \leq$ -10 dB for most of the UWB range and a lower resonance frequency at 1.4 GHz is obtained which is suitable for WMTS applications. This position of the shorting strip corresponds to $0.115\lambda_{g1}$, where λ_{g1} is the guide wavelength at the desired lower resonance frequency.

Effect of distance of second shorting strip, P₂

For the above position of the first shorting strip, there is considerable mismatch in the UWB range 5-6 GHz. To further improve the matching in this range, a second shorting strip is also placed at the inner end of the spiral such that the first resonance remains undisturbed. The variation in reflection characteristics for different positions of the second shorting strip is shown in Fig. 5.16.
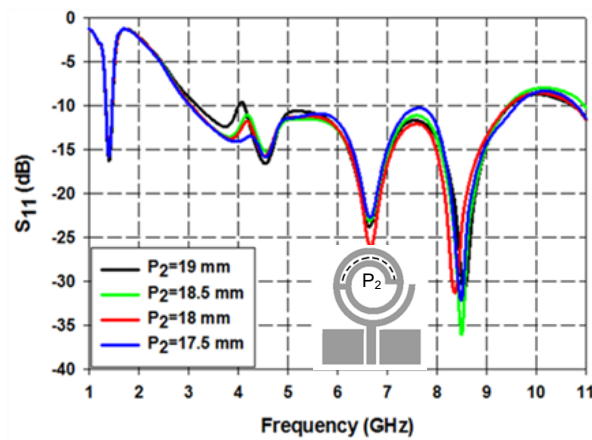
Fig. 5.16   Simulated S_{11} vs frequency of dual-band spiral monopole antenna with shorting strips (Type-II) for varying P_2 with $\epsilon_r = 4.4$, h = 1.6 mm, $SL_1 = 97$ mm, $SL_2 = 18.2$ mm, $L_g = 10$ mm, $W_g = 12$ mm, $W_f = 3$ mm, g = 0.3 mm, s = 0.3 mm, $g_s = 1.5$ mm, $W_s = 2$ mm, $P_1 = 17$ mm, D = 21 mm and t = 2 mm

From the surface current distribution discussed in Section 5.2.3, it can be seen that the second shorting strip creates an inner closed loop resonator with perimeter corresponding to λ_g at 5.5 GH. Hence improved matching is obtained at this frequency. As distance P_2 varies, the first resonance remains undisturbed. However, impedance matching in the UWB range varies. For distance $P_2 = 18$ mm, optimum matching is

achieved in the UWB range. This is equivalent to $0.59\lambda_c$ where λ_c is the guide wavelength at center of the UWB band.

Effect of thickness of shorting strip, t

The two short circuit strips have the same thickness and the variation of S_{11} with frequency as thickness is varied is shown in Fig. 5.17.
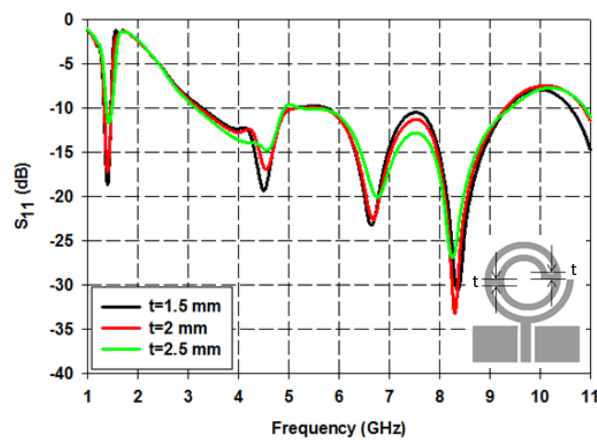
Fig. 5.17   Simulated S_{11} vs frequency of dual-band spiral monopole antenna with shorting strips (Type-II) for varying t with ϵ_r = 4.4, h = 1.6 mm, SL_1 = 97 mm, SL_2 = 18.2 mm, L_g = 10 mm, W_g = 12 mm, W_f = 3 mm, g = 0.3 mm, s = 0.3 mm, g_s = 1.5 mm, W_s = 2 mm, D = 21 mm, P_1 = 17 mm and P_2 = 18 mm

As thickness increases, impedance matching improves in the UWB band but degrades in the WMTS band. At t = 2 mm, optimum results are obtained. The optimum thickness is 2 mm and is of the same value as W_s which ensures a smooth flow of current between the spiral arms.

5.2.3 Surface Current Distribution of Dual-band Spiral Monopole Antenna with Shorting Strips (Type-II)

To gain further insight on how the antenna dimensions affect the various operating frequencies, the surface current distribution at different frequencies is shown in   Fig. 5.18.
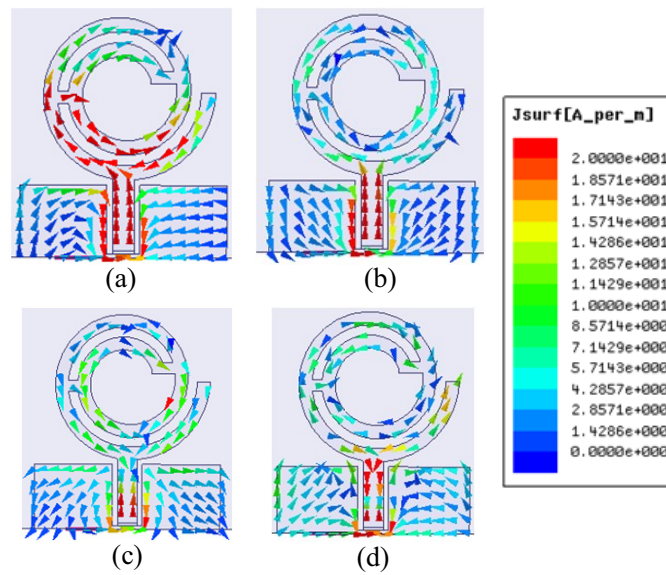
Fig. 5.18   Surface current distribution of dual-band spiral monopole antenna with shorting strips (Type-II) at (a) 1.4 GHz (b) 3.3 GHz (c) 6.5 GHz (d) 10.6 GHz with ϵ_r = 4.4, h = 1.6 mm, SL_1 = 97 mm, SL_2 = 18.2 mm, L_g = 10 mm, W_g = 12 mm, W_f = 3 mm, g = 0.3 mm, s = 0.3 mm, g_s = 1.5 mm, W_s = 2 mm, P_1 = 17 mm, P_2 = 18 mm, D = 21 mm and t = 2 mm

At 1.4 GHz, the current distribution shows that the first shorting strip alters the flow of current on the inner turn of the spiral. This can be compared to the current distribution seen at the first resonance in Fig. 5.8 (a) for the structure without shorting strip. Fig. 5.18 (a) shows quarter wave distribution on the lower portion of the inner turn. Current flow is in the opposite direction on the upper portion of the inner turn but it is of very

146

low intensity. At 3.3 GHz, current distribution is mainly seen on the outermost turn of the spiral. At 5.5 GHz, an inner closed loop with one full wave variation is formed by the second shorting strip which results in the improved impedance matching at this frequency. At 9 GHz, the distribution shows the excitation of higher order modes similar to that seen in an ultrawideband circular monopole.

5.2.4 Design Equations of Dual-band Spiral Monopole Antenna with Shorting Strips (Type-II)

From the optimized dimensions obtained by parametric analysis, design equations are formulated. The procedure to design the antenna on a different substrate is the same as that adopted for Type-I antenna. Equations (5.1)-(5.6) as outlined in steps (1) to (7) of Section 5.1.4 are repeated. To lower the operating frequency, the following steps are carried out:

1) Place a shorting strip at

$$P_1 = 0.115\lambda_{g1} \hspace{4cm} (5.7)$$

where λ_{g1} is the guide wavelength corresponding to the lower resonance.

2) Place a second shorting strip at

$$P_2 = 0.59\lambda_c \hspace{4cm} (5.8)$$

where λ_c is the guide wavelength corresponding to the center of the UWB band.

3) Set the thickness, t of both shorting strips to be equal to spiral strip width, W_s.

The design equations are used to design the antenna on different substrates for operation in UWB band and a lower resonance at 1.4 GHz. Evaluated dimensions are listed in Table 5.3.

Table. 5.3   Dual-band spiral monopole antenna with shorting strips
(Type-II) parameters for different substrates obtained
from design equations

Parameter (mm)	Substrate			
	1	**2**	**3**	**4**
	Rogers 5880 ϵ_r =2.2	**Rogers RO4003** ϵ_r =3.55	**FR-4 Epoxy** ϵ_r =4.4	**Rogers RO3006** ϵ_r =6.15
h	1.57	0.8	1.6	1.28
W$_f$	4	6	3	2.58
g	0.17	0.3	0.3	0.45
L$_g$	12.3	10.7	9.96	8.84
W$_g$	14.7	12.8	11.99	10.6
s	0.17	0.3	0.3	0.45
W$_s$	2.44	2.13	1.98	1.76
g$_s$	1.83	1.59	1.48	1.32
SL$_1$	111.6	104.9	98.3	88.34
SL$_2$	20.62	19.15	18	15.5
D	25.9	22.5	20.9	18.6
P$_1$	20.8	18.1	16.9	14.9
P$_2$	22.2	19.31	18	15.96
t	2.44	2.13	1.98	1.76

Using these dimensions, the antenna is simulated of the different substrates and reflection characteristics obtained after simulation are shown in Fig. 5.19. On all substrates, dual band operation suitable for WMTS and UWB operation are obtained.
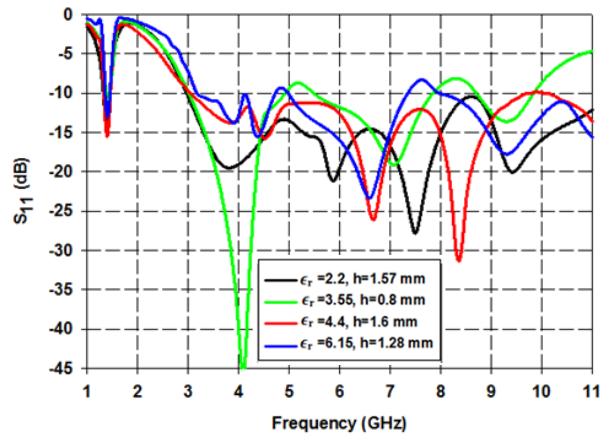
Fig. 5.19   Simulated reflection characteristics of proposed dual-band spiral monopole antenna with shorting strips (Type-II) on different substrates

The lower band resonance and lower limit of the UWB band obtained from simulation for each substrate are compared with desired values of 1.4 GHz and 3.1 GHz and percentage error is shown in Table 5.4.

Table 5.4   % Error in simulated frequency of dual-band spiral monopole antenna with shorting strips (Type-II) for different dielectric substrates at f_l = 1.4 GHz and f_L= 3.1 GHz

Substrate	Simulated Frequency (GHz)		Error (%)	
	f_l	f_L	f_l	f_L
Rogers 5880 (ϵ_r = 2.2, h = 1.57 mm)	1.37	2.96	2.14	4.5
Rogers RO4003 (ϵ_r = 3.55, h = 0.8 mm)	1.43	3	2.14	3.2
FR-4 Epoxy (ϵ_r = 4.4, h = 1.6 mm)	1.39	3.02	0.71	2.5
Rogers RO3006 (ϵ_r = 6.15, h = 1.28 mm)	1.45	3.16	3.57	1.9

On all substrates, the error is very low which shows that the design equations are valid. The design equations are also validated by fabricating the antenna on Rogers

149

RT/Duroid 5880 substrate and experimental results of reflection characteristics are shown next. Complete characterization of this antenna is presented in Appendix-B.

5.2.5 Reflection Characteristics of Dual-band Spiral Monopole Antenna with Shorting Strips (Type-II)

Using the optimized design values the antenna is fabricated for a substrate of thickness 1.6 mm and relative permittivity 4.4 as well as for a different substrate of thickness 0.79 mm and relative permittivity 2.2 as shown in Fig. 5.20 (a) and Fig. 5.21 (a) respectively. The antennas are tested using Agilent PNA E8362B. The experimental results of reflection characteristics are compared with simulation results in Fig. 5.20 (b) and 5.21 (b).

(a)   (b)
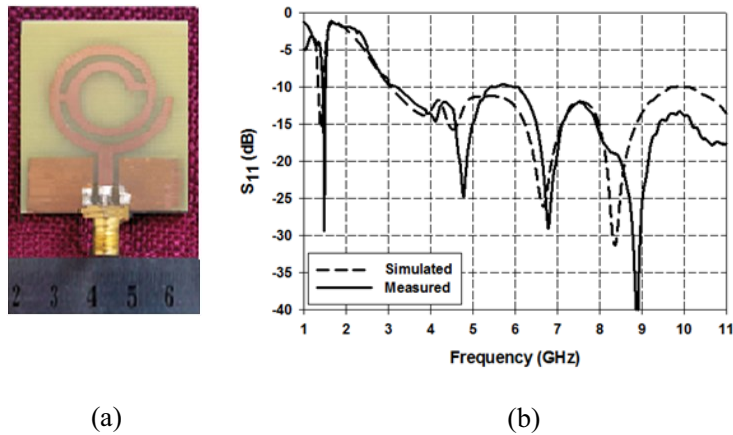
Fig. 5.20   (a) Fabricated prototype (b) Simulated and measured reflection characteristics of dual-band spiral monopole antenna with shorting strips (Type-II) on FR-4 substrate of $\epsilon_r = 4.4$ and thickness h = 1.6 mm with $SL_1 = 97$ mm, $SL_2 = 18.2$ mm, $L_g = 10$ mm, $W_g = 12$ mm, $W_f = 3$ mm, g = 0.3 mm, s = 0.3 mm, $g_s = 1.5$ mm, $W_s = 2$ mm, D = 21 mm, $P_1 = 17$ mm, $P_2 = 18$ mm and t = 2 mm

(a)	(b)
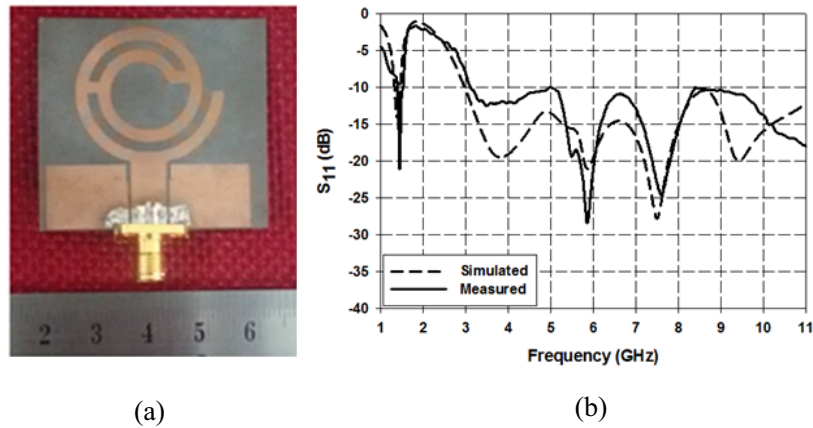
Fig. 5.21   (a) Fabricated prototype (b) Simulated and measured reflection characteristics of dual-band spiral monopole antenna with shorting strips (Type-II) on Rogers RT/Duroid 5880 substrate of $\epsilon_r = 2.2$ and thickness h = 0.79 mm with $SL_1 = 113.1$ mm, $SL_2 = 20.1$ mm, $L_g = 12.3$ mm, $W_g = 15.4$ mm, $W_f = 6.9$ mm, g = 0.48 mm, s = 0.48 mm, $g_s = 1.83$ mm, $W_s = 2.44$ mm, D = 25.9 mm, $P_1 = 18$ mm, $P_2 = 19.1$ mm and t = 2.44 mm

The simulated and measured values show good agreement in their variation. As is seen in all the antennas proposed, there is a mismatch in readings at higher frequencies. However, the antenna shows good impedance matching throughout the UWB band.

Operating frequency ranges are 1.38-1.43 GHz and 3.2-11 GHz on FR-4 substrate and 1.35-1.52 GHz and 3.1-11 GHz on Rogers RT/Duroid 5880 substrate for $S_{11} \leq -10$ dB. Hence the design equations are validated and the antenna is suitable for WMTS and UWB applications.

5.2.6 Radiation Pattern of Dual-band Spiral Monopole Antenna with Shorting Strips (Type-II)

The antenna structure with the optimized dimensions obtained from the parametric analysis is simulated in HFSS™ software and the three-dimensional radiation patterns are plotted in Fig. 5.22.
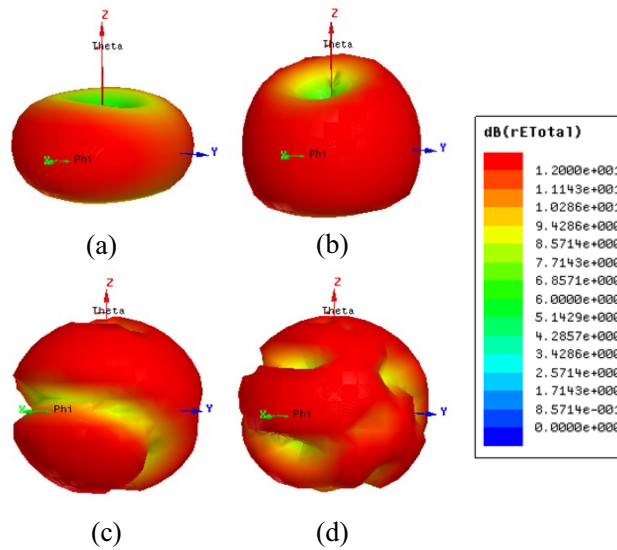
Fig. 5.22   Simulated 3D radiation patterns of the dual-band spiral monopole antenna with shorting strips (Type-II) at the resonance frequencies (a) 1.4 GHz (b) 3.3 GHz (c) 6.5 GHz (d) 10.6 GHz with $\epsilon_r = 4.4$, h = 1.6 mm, $SL_1 = 97$ mm, $SL_2 = 18.2$ mm, $L_g = 10$ mm, $W_g = 12$ mm, $W_f = 3$ mm, g = 0.3 mm, s = 0.3 mm, $g_s = 1.5$ mm, $W_s = 2$ mm, D = 21 mm, $P_1 = 17$ mm, $P_2 = 18$ mm and t = 2 mm

At first resonance and lower frequency of the UWB band a doughnut pattern is observed. At 6.5 GHz, the pattern shape changes but is almost non-directional in the horizontal plane. At 10.6 GHz, the pattern becomes quite distorted due to the excitation of higher order modes in the monopole. The two dimensional patterns are shown in Fig. 5.23.

X-Z   **X-Y**

(a)

(b)

(c)

(d)

———— Co- polarization

– – – – Cross-polarization
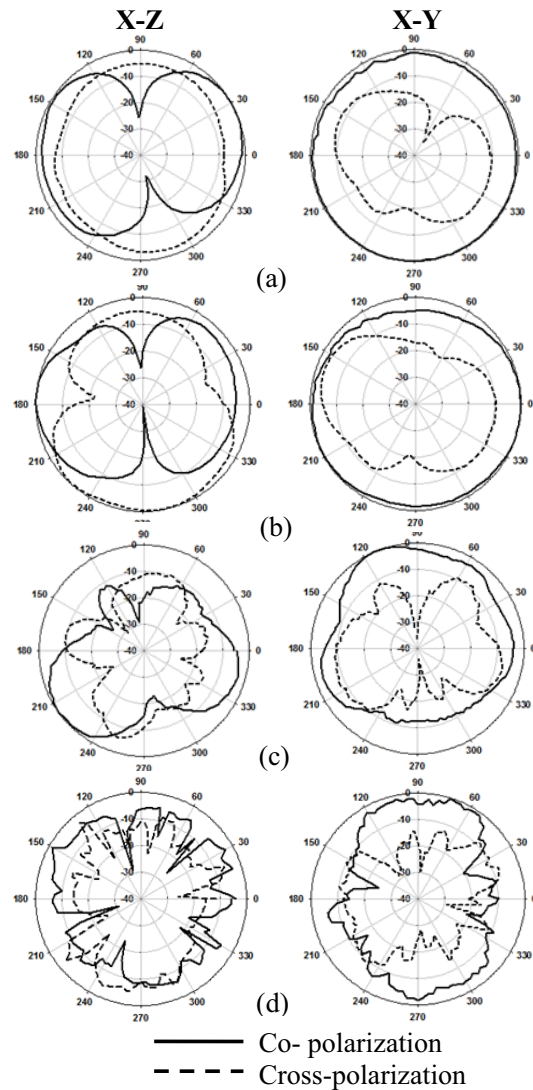
Fig. 5.23   Normalized 2D radiation pattern of dual-band spiral monopole antenna with shorting strips (Type-II) measured at the resonance frequencies (a) 1.4 GHz (b) 3.3 GHz (c) 6.5 GHz (d) 10.6 GHz with ϵ_r = 4.4, h = 1.6 mm, SL_1 = 97 mm, SL_2 = 18.2 mm, L_g = 10 mm, W_g = 12 mm, W_f = 3 mm, g = 0.3 mm, s = 0.3 mm, g_s = 1.5 mm, W_s = 2 mm, D = 21 mm, P_1 = 17 mm, P_2 = 18 mm and t = 2 mm

The E-plane (X-Z) patterns have figure-8 shape at lower frequencies but get distorted

at higher frequencies due to higher order mode excitation. It is seen that on average the

153

cross polarization levels are good over all operating bands. However, at lower frequencies of the UWB band, poor cross polarization is seen towards 150° in the X-Y plane.

5.2.7 Gain and Efficiency of Dual Band Spiral Monopole Antenna with Shorting Strips (Type-II)

The peak gain and efficiency are measured and their plots are shown in Fig. 5.24.

<div align="center">(a)   (b)</div>
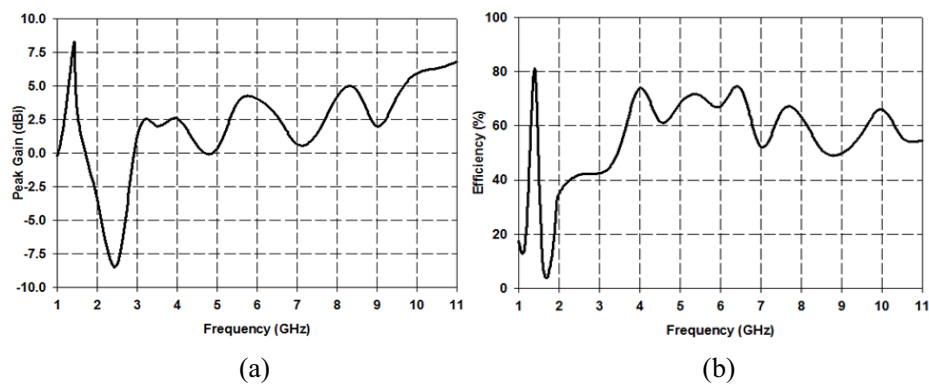
Fig. 5.24   (a) Peak gain and (b) Efficiency of dual-band spiral monopole antenna with shorting strips (Type-II) with $\epsilon_r = 4.4$, h = 1.6 mm, SL_1 = 97 mm, SL_2 = 18.2 mm, L_g = 10 mm, W_g = 12 mm, W_f = 3 mm, g = 0.3 mm, s = 0.3 mm, g_s = 1.5 mm, W_s = 2 mm, D = 21 mm, P_1 = 17 mm, P_2 = 18 mm and t = 2 mm

The peak gain and efficiency plots show similar variation. At the lower resonance of 1.4 GHz, peak gain is 8.3 dBi and efficiency is 79 %. In the UWB range, peak gain is 6.3 dBi while a maximum of 74 % efficiency is achieved.

5.3 TIME DOMAIN ANALYSIS OF CPW-FED SPIRAL MULTIBAND ANTENNAS

In the previous sections the frequency domain parameters of CPW-fed spiral multiband antennas Type-I and Type-II are evaluated. Since time domain analysis is as important

154

as frequency domain analysis for UWB antennas, the following section describes the time domain analysis of the proposed antennas.

5.3.1 Group Delay

Group delay is evaluated keeping two similar antennas 15 cm apart and measured values for three different orientations are shown in Fig. 5.25.
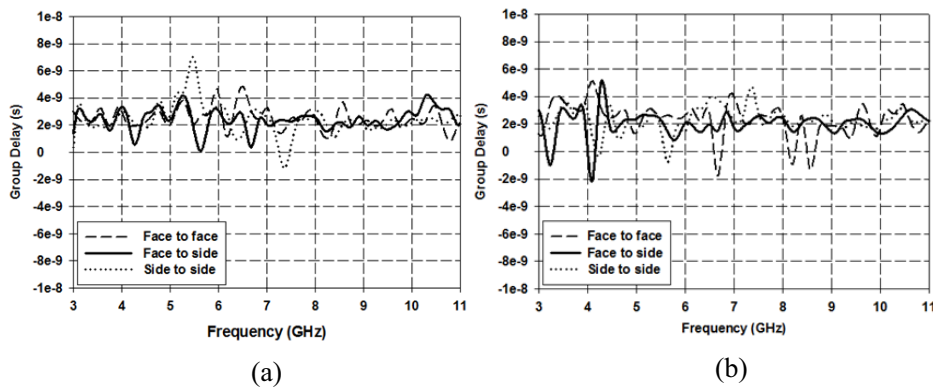
Fig. 5.25   Measured group delay of CPW-fed spiral multiband antenna (a) Type-I (b) Type-II for different orientations

For Type-I antenna, face to side orientation shows least group delay variation while in Type-II antenna, side to side orientation has the least variation. The variation is high occasionally but the antennas are suitable for multi band orthogonal frequency division multiplexing (MB-OFDM) UWB systems. For all orientations, Type-I antenna shows higher variation than Type-II antenna. Type-II antenna is electrically smaller than Type-I antenna and as antenna size decreases, phase difference between the surface currents at different parts of the antenna is minimum. Hence lower average group delay is seen for Type-II antenna.

155

5.3.2 Transfer Function and Impulse Response

The S_{21} characteristics of the antenna are measured at 45° intervals over the azimuth

(X-Y) plane and using these values, the transfer functions are plotted in Fig. 5.26.
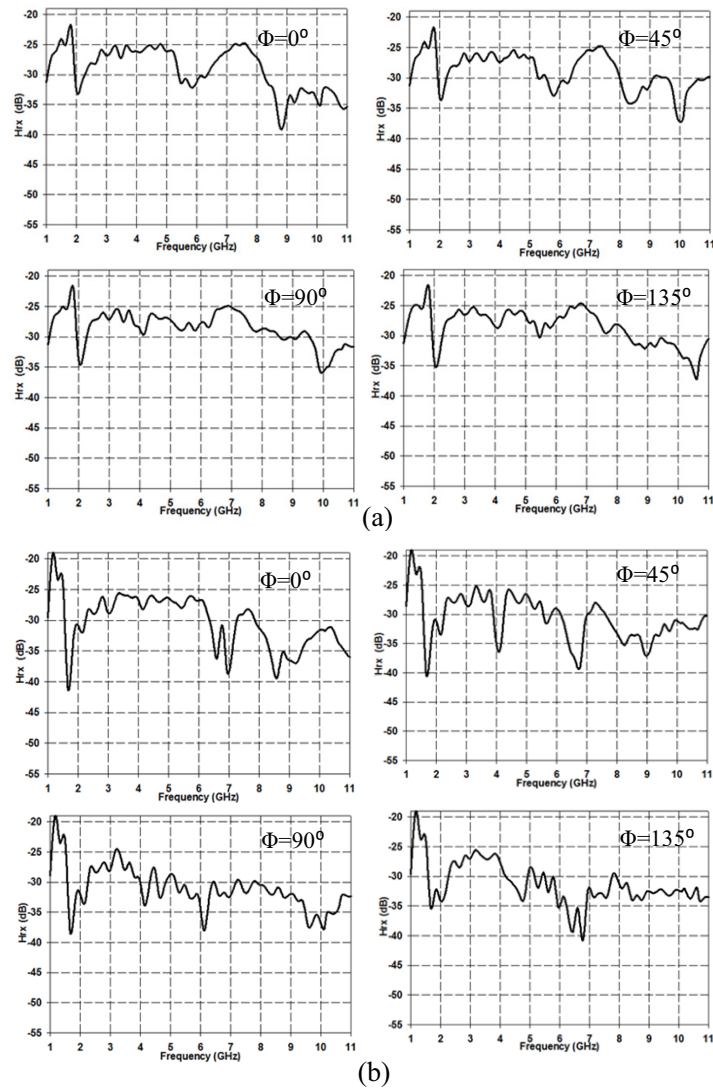
Fig. 5.26   Computed transfer function of CPW-fed spiral multiband antenna (a) Type-I (b) Type-II for different angles in azimuth plane

A sharp decrease in values is observed at unintended frequencies between the lower resonance and the UWB band in both types of antennas. By taking inverse Fourier transform of the obtained transfer functions, impulse response is obtained and the corresponding plots in azimuth plane are shown in Fig. 5.27.

(a)

(b)
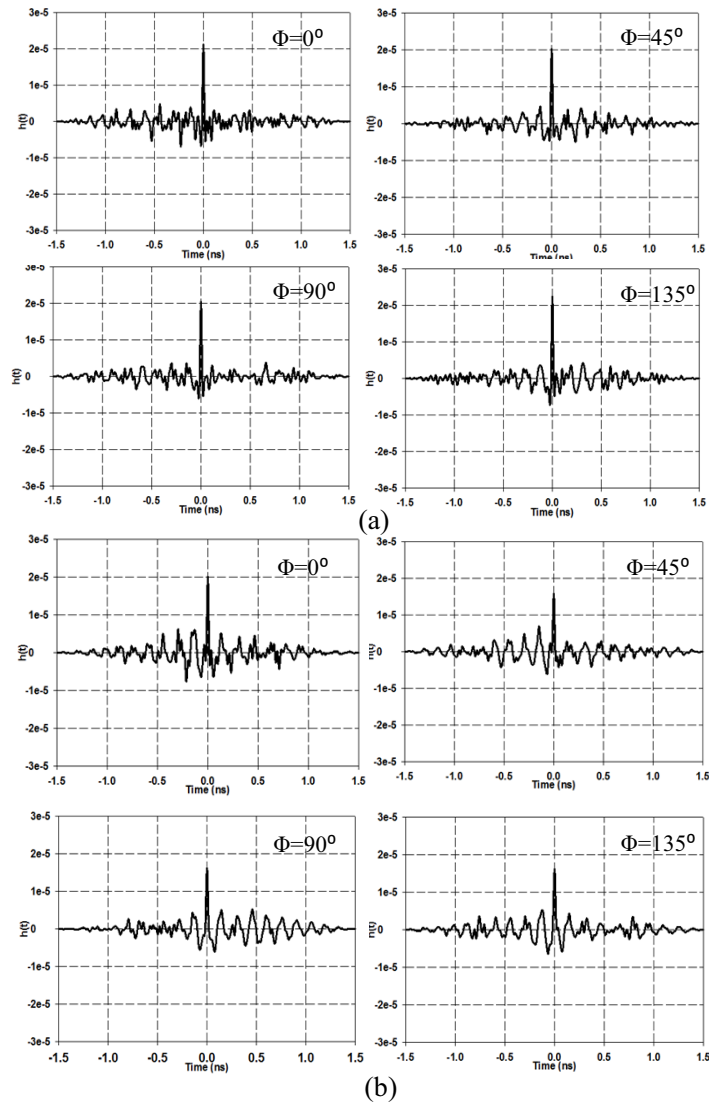
Fig. 5.27   Computed impulse response of CPW-fed spiral   multiband antenna (a) Type-I (b) Type-II for different angles in azimuth plane

The variation in amplitude of the impulse response indicates ringing and the duration of the ringing is defined as the time period over which the envelope has fallen from the peak value to a fraction of the peak. This duration is a measure of the dispersion introduced by the antenna. Measured values of full width half maxima (FWHM) and ringing of the proposed antennas for different azimuth angles are shown in Table. 5.5.

Table 5.5   Computed values of FWHM and ringing of CPW- fed
spiral multiband antennas for different azimuth angles

Azimuth Angle	Type-I antenna		Type-II antenna	
	FWHM (ps)	Ringing (ps)	FWHM (ps)	Ringing (ps)
$\Phi=0^\circ$	206	231	217	181
$\Phi=45^\circ$	194	150	175	199
$\Phi=90^\circ$	202	158	169	125
$\Phi=135^\circ$	226	346	153	237

From the measured results, Type-I design shows higher ringing and dispersion compared to Type-II antenna. This is expected due to the higher group delay seen in Fig. 5.24.

5.3.3 Fidelity Factor

For a UWB system, the received signal is required to match the input pulse with minimum distortions because the signal is the carrier of useful information. Assuming a fourth order Gaussian pulse is fed as input to the antenna, the normalized received pulses for three different orientations are shown in Fig. 5.28 for both types of antennas.
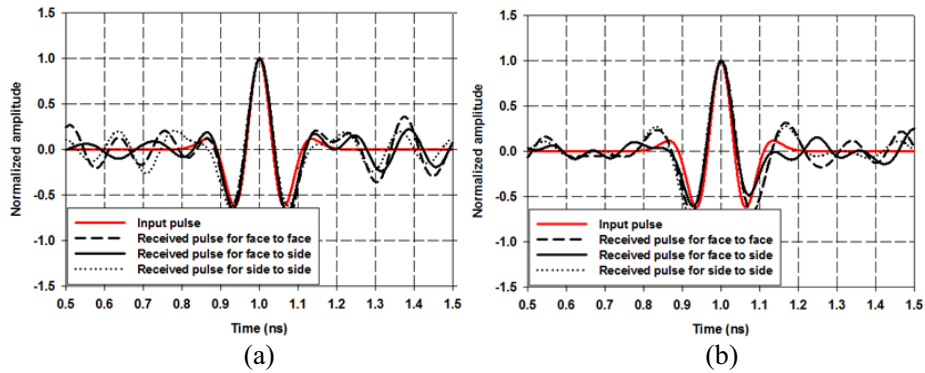
Fig. 5.28   Comparison of input and received pulses in CPW-fed spiral multiband antenna (a) Type-I (b) Type-II for different orientations

For Type-I antenna, received pulse closely follows the input pulse in all orientations but with some ringing. In Type-II antenna the received pulse for face to side orientation shows good matching with input pulse while the remaining two orientations show some mismatch.

The degree of correlation between the input and received pulses is evaluated using the fidelity factor shown in Fig. 5.29.
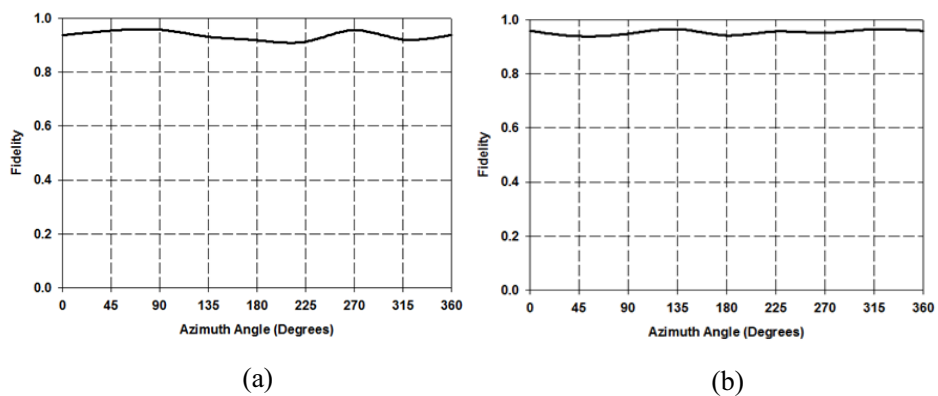
Fig. 5.29   Fidelity factor of CPW-fed spiral multiband antenna (a) Type-I (b) Type-II in azimuth plane

159

Fidelity factor is above 90 % for both types of antennas over all angles which shows

that the input and received pulses are in close agreement with each other.

5.3.4 Radiated Power Spectral Density

It is important that UWB systems conform to the limits imposed by the FCC. To check

whether the proposed antennas are suitable for UWB communication, radiated power

spectral density (PSD) is evaluated as shown in Fig. 5.30.

Within the frequency range from 3.1 to 10.6 GHz the radiated power of both proposed

antennas is compliant with the limit of -41.3 dBm/MHz which confirms their suitability

for UWB applications.

(a)   (b)
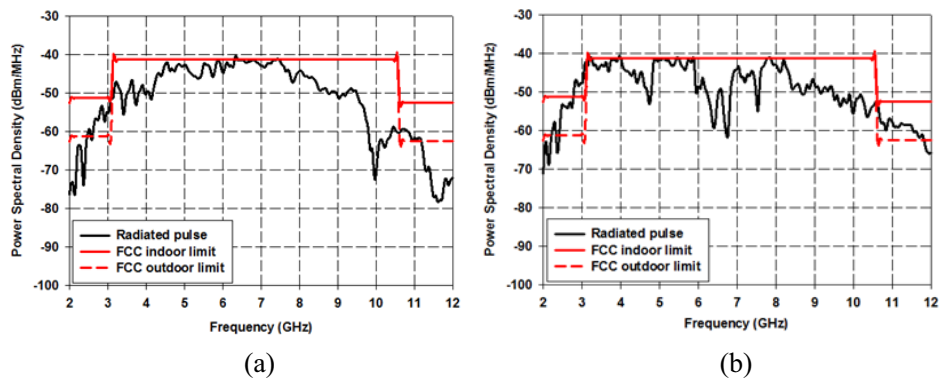
Fig. 5.30   Power spectral density of the radiated pulse for CPW-fed
spiral multiband antenna (a) Type-I (b) Type-II against
the FCC emission mask

5.4 CHAPTER SUMMARY

Two multiband antennas using a spiral monopole are proposed in this chapter. In Type-

I design the orientation of the spiral with respect to feed line is such that the outermost

turn of the spiral monopole is similar to the outer edge of a wideband circular monopole and results in UWB operation. The spiral arm acts as a ring resonator for operation in the GSM band. The operating frequencies of the antenna are 1.75-1.92 GHz and 3.38-11 GHz and the antenna size is 27.6×28.3 mm^2 on a substrate of relative permittivity 4.4 and thickness 1.6 mm.

In Type-II design, a shorting strip is introduced between the arms of the spiral in Type-I design by which the first resonance is lowered to a band suitable for WMTS application. However, this degrades impedance matching in the UWB range and so a second shorting strip is also used to improve matching in the UWB range without disturbing the first resonance. The frequency of operation is lowered without increase in the overall dimensions of the antenna and the operating frequencies of the antenna are 1.38-1.43 GHz and 3.2-11 GHz suitable for operation in WMTS and UWB bands respectively.

The antennas are compared in terms of lowest operating frequency, size and peak gain with some of the wideband and multiband spiral antennas proposed in literature and the features are summarized in Table. 5.6.

In the antenna proposed by Chiu and Chuang (2009), the frequency range of operation is lower than the proposed antenna Type-I. But the antenna is larger in size. A CPW-fed Archimedean spiral antenna is proposed by Dahalan *et al*. (2013) in which frequency of operation can be switched between wideband and narrow band mode. Here also the antenna size is larger. In the antenna by Zhang *et al*. (2013), multiband operation is achieved and the antenna is very compact. The antenna by Wan *et al*.

(2013) is a modification of the geometry proposed by Zhang *et al*. (2013) and has the advantage of CPW-feed as in the proposed antennas. But in both antennas, operation is suitable for multiple narrow bands and does not cover the UWB band. Huang and Lv (2014), developed a wideband spiral antenna which covers almost the same frequency range as the proposed antenna Type-I. However, the spiral has two arms and requires a balun for proper impedance matching.

Table 5.6   Comparison of proposed antennas with existing spiral multiband antennas

Antenna	No. of operating bands	Lowest operating frequency	Size(mm³)	ϵ_r	Peak Gain
Chiu and Chuang (2009)	2	1.7 GHz	52×47×1.6	4.4	2.5-3.8 dBi
Dahalan *et al*. (2013)	1	2 GHz	60×69×1.6	4.6	1-2.5 dBi
Zhang *et al*. (2013)	4	2.4 GHz	28×20×1	2.65	1.77-2.45 dBi
Wan *et al*. (2013)	3	2.4 GHz	27.5×20×1	2.55	1.95-2.71 dBi
Huang and Lv (2014)	1	1.8 GHz	38×38×0.8	2.2	3.8-6.3 dBi
Proposed antenna Type-I	2	1.75 GHz	27.6×28.3×1.6	4.4	1-8.36 dBi
Proposed antenna Type-II	2	1.38 GHz	27.6×28.3×1.6	4.4	1-8.3 dBi

Good impedance matching, non-directional radiation patterns and stable gain across the operating bands show that the antennas are good candidates for wireless

communication devices. Frequency and time domain characteristics ensure their suitability for UWB applications. The antennas are also of smaller size than the other antennas proposed in the thesis.

Chapter 6

CONCLUSION AND FUTURE WORK

A summary of all the proposed antennas and conclusions drawn from the study are presented. This is followed by some suggestions for future work.

6.1 THESIS SUMMARY AND CONCLUSION

The aim of this thesis is to develop compact CPW-fed multiband antennas incorporating the UWB band. A comprehensive study on the design, simulation, testing and characterization of the proposed antennas is presented taking into account the constraints of pulse based operations. Three designs of CPW-fed multiband antennas are presented. The first design consists of a CPW-fed circular monopole with a hexagonal slot. A fractal pattern is introduced in the monopole for multiband operation. In the second design, the hexagonal slot is modified to obtain multiband operation suitable for UWB applications. In the third design of antennas a CPW-fed spiral monopole is used to obtain multiband operation with UWB applications. Different techniques are used to lower the frequency of operation of the designed antennas without increase in overall size. The evolutions of the designed antennas are investigated in detail for better insight into their multiband behavior.

From the parametric studies on antenna dimensions carried out using the simulation tool and surface current distributions investigated at different resonances, design guidelines are formulated for the various antennas. This can help the antenna designer to design the antenna on any substrate for the desired frequency range of operation. The deduced geometry can act as a precursor to the final optimized design. The antennas with optimized dimensions are fabricated and tested and experimental results

are compared with simulation values. Characterization in frequency domain is carried out for all the antennas in frequency domain. For the antennas operating in UWB band, time domain characterization is also carried out. A comparison of the characteristics of all the proposed antennas is shown in Table 6.1. The proposed antennas are summarized as:

CPW-fed fractal multiband antenna- In this design, a hexagonal slot is inserted in a circular monopole and then the structure is scaled down to create a fractal pattern. The antenna is suitable for GSM, IMT advanced system for 4G mobile communication systems and upper WLAN applications. The results are presented in Chapter 3 and have been reported in *Publication 1*. However, since the second and third resonance bands are already covered by the wideband circular monopole from which the design has evolved, a better design which extends the frequency range of operation is developed next.

CPW-fed slotted multiband antennas- Three types of antennas are presented in Chapter 4 using slotted design approach and all the antennas operate over the UWB range as well as at lower frequency bands. In these antennas, the slot shape of the CPW-fed fractal multiband antenna developed in Chapter 3 is modified to obtain dual-band operation which covers the entire UWB band. The Type-I antenna is suitable for GSM and UWB applications. In Type-II antenna, a fractal pattern is introduced. The fractal pattern is created by scaling down the slotted monopole structure and arranging it in the space created by the slot. The antenna operates over similar frequency ranges as Type-I antenna but has improved matching in the UWB range. In Type-III antenna a bent monopole is introduced in the structure. The perimeter of the bent monopole

increases the perimeter of the slot and this lowers the first resonance frequency. The bent monopole also contributes to a second resonance band which makes the antenna suitable for triple-band operation. The antenna is suitable for WMTS, UMTS and UWB applications. The results of these designs are reported in *Publications 2* and *4*. To make the antennas more compact, a spiral monopole is used and this is discussed next.

CPW-fed spiral multiband UWB antennas- Two types of multiband antenna are proposed using a spiral design approach in Chapter 5. Type-I antenna consists of a spiral that is oriented such that it operates over the UWB band with the spiral arm resulting in a lower frequency band. The operating frequencies of the antenna are suitable for GSM and UWB applications. In Type-II antenna, a shorting strip is introduced between the arms of the spiral by which the first resonance is lowered to a frequency which makes the antenna suitable for WMTS and UWB applications. Results of the two antennas are reported in *Publication 3*. The antennas are very compact with respect to all the other antennas proposed in this thesis.

On comparing time domain characteristics of the CPW-fed slotted multiband antennas presented in Chapter 4, it is seen that Type-II antenna has highest ringing and lowest fidelity. This is due to the complicated current path created by the fractal pattern. This suggests that simple designs are preferable for antennas intended to work in the UWB range. For the antennas developed using CPW-fed spiral monopole presented in Chapter 5, Type-II design exhibits low FWHM and ringing with high fidelity.

Table 6.1　Comparison of performance characteristics of the proposed antennas

Proposed Antenna	Size (mm²)	Operating bands (GHz)	Peak Gain (dBi)	FWHM (ps)		Ringing (ps)		Fidelity (%)	
				Min	Max	Min	Max	Min	Max
CPW-fed fractal multiband antenna									
	34× 51.3	1.63-2.07	2.51	*					
		3.63-4.22	2.45						
		5.08-6.48	2.67						
CPW- fed slotted multiband antennas									
I	34× 51.3	1.68-2.06	2.82	*					
		3.27-11	7.35	165	175	112	373	95	97
II	34× 51.3	1.5-2	2.82	*					
		3.4-11	6.5	163	171	112	450	78	97
III	34× 51.3	1.35-1.48	6.9	*					
		2-2.27	0.2	*					
		3.14-10.8	8.17	160	176	126	420	90	97
CPW-fed spiral multiband antennas									
I	27.6× 28.3	1.75-1.92	8.36	*					
		3.3-11	5.85	194	226	150	346	90	98
II	27.6× 28.3	1.38-1.43	8.3	*					
		3.2-11	6.3	153	217	125	237	92	97

* Not applicable for narrow resonance band

6.2 SUGGESTIONS FOR FUTURE WORK

The designs proposed in this thesis can be further enhanced and some suggestions for future work are outlined here.

All antenna measurements presented in this thesis have been carried out in an anechoic chamber. However, UWB systems are used in WPANs and the antenna might be embedded in a laptop or other portable devices. Hence the effect of human body on antenna performance as well as the possibility of electromagnetic absorption by the human body needs to be investigated.

Direct time domain measurements may be performed for all the proposed antennas using a nano-second pulse generator and a high speed digital storage oscilloscope.

Lower bands suitable for GSM 800/900 applications can be incorporated. Also, biomedical sensors operating at still lower frequencies can be integrated in a similar manner wherein the UWB band serves as the indoor communication channel.

Due to the low power level operation of UWB systems, a typical UWB receiver requires a low-noise amplifier. Antenna integration with low-noise amplifier may be investigated in future.

APPENDIX-A

COMPACT CPW-FED UWB ANTENNA WITH DUAL NOTCH BANDS

In some European and Asian countries, there exist narrowband wireless services such as worldwide interoperability for microwave access (WiMAX) operating from 3.3-3.7 GHz and wireless local area network (WLAN) operating from 5.15-5.825 GHz within the UWB spectrum. The narrowband devices operating at these frequencies can pose interference to UWB devices. To address this problem, additional filters may be used in the UWB system to notch out the interfering bands. But this will increase the complexity of the UWB system. A simpler band notching technique is to insert a thin slot in the patch antenna with a length that is an integral multiple of $\lambda_n/4$ where λ_n is the guide wavelength of the notched frequency (Yu and Wang, 2009). Other reported techniques include using a parasitic strip or stub, an electric LC resonator and using a transmission line with band stop characteristic to feed the antenna (Kelly *et al*., 2011; Li *et al*., 2013; Mansouri *et al*., 2016; Sayidmarie and Najm, 2013). Recently, hybrid techniques have been adopted to attain two notched bands (Vyas *et al*., 2014; Wu and Guan, 2013; Li and Ye, 2011). But all these methods introduce a slot in the radiating patch which reduces the gain. Here, a CPW-fed UWB antenna with dual notch bands is presented by inserting L and U-shaped slots in the ground plane and feed line respectively.

A.1 ANTENNA GEOMETRY

The geometry of the proposed antenna is shown in Fig. A.1. The substrate used is of thickness h=1.6 mm, relative permittivity $\epsilon_r = 4.4$ and loss tangent tan $\delta = 0.02$. A semicircular disc monopole of diameter D is used as the radiating patch. The antenna

of size W×L is fed using a 50 Ω CPW feed of width W_f. The feed line is spaced by a gap g from the ground plane of width W_g and length L_g (Liang, 2005b).
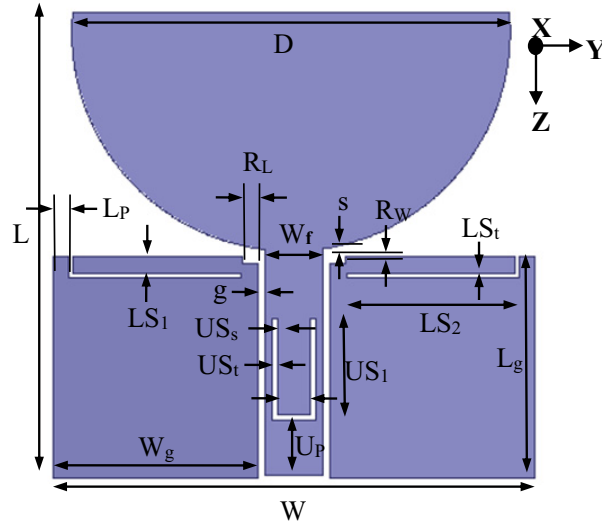
Fig. A.1   Geometry of the antenna with optimized dimensions L = 32 mm, W = 31.6 mm, D = 30 mm, L_g = 15 mm, W_g = 14 mm, R_L = 1 mm, R_W = 0.5 mm, W_f = 3 mm, g = 0.3 mm, s = 0.3 mm, LS_1 = 1.5 mm, LS_2 = 11.5 mm, LS_t = 0.3 mm, L_p = 1.5 mm, US_1 = 7 mm, US_2 = 2.4 mm, US_t = 0.3 mm, US_s = 0.5 mm and U_p = 4 mm

The monopole is fed with a spacing s from the ground plane. The L-shaped slot is inserted in the ground plane and has two arms of length LS_1 and LS_2 and width LS_t. Both L-shaped slots have the same dimensions and are positioned at a distance L_p from the outer edge of the ground plane. The overall length of each slot is approximately a quarter wavelength of the notched frequency.

The U-shaped slot inserted in the CPW feed line has two vertical arms each of length US_1, one horizontal arm of length US_2 and the slot width is US_t. The slot is spaced at a

distance US_s from the edge of the feed line and U_p from the end of the feed line. The overall length of this slot is approximately a half wavelength of the notched frequency.

A.2 PARAMETRIC ANALYSIS

Optimized parameters for band notch performance in the WiMAX and WLAN range are obtained by conducting a parametric analysis on the slot dimension position.

A.2.1 Optimization of L-slot Parameters

First, only the L-slot is introduced in the ground plane and its effects are studied.

Effect of length 'LS_1+LS_2' of L-slot

The lengths of the two segments are optimized by a parametric analysis in which the overall length is kept constant and simulated S_{11} results are shown in Fig. A.2.

Fig. A.2   Simulated S_{11} vs frequency of the antenna for different lengths of L-slot segments with $\epsilon_r = 4.4$, h = 1.6 mm, L = 32 mm, W = 31.6 mm, D = 30 mm, L_g = 15 mm, W_g = 14 mm, R_L = 1 mm, R_W = 0.5 mm, W_f = 3 mm, g = 0.3 mm, s = 0.3 mm, LS_t = 0.3 mm, L_p = 2 mm, US_1 = 7 mm, US_2 = 2.4 mm, US_t = 0.3 mm, US_s = 0.5 mm and U_p = 4 mm

The L-shaped slot is made up of two segments and the overall length of each slot is approximately a quarter wavelength of the WiMAX frequency.

$$LS_1 + LS_2 \approx \frac{\lambda_g}{4} \qquad (A.1)$$

where λ_g is $\frac{\lambda}{\sqrt{\epsilon_{reff}}}$ and ϵ_{reff} is the effective dielectric constant. All combinations of the segment lengths result in a rejection of the WiMAX band. However, for $LS_1 = 1.5$ mm and $LS_2 = 11.5$ mm, maximum rejection over the required band is obtained and so this combination is chosen as the optimum value.

Effect of position of L-slot, L_p

For the chosen length of the two segments of the L-slot, the position is varied and simulated S_{11} results are shown in Fig. A.3.

Fig. A.3   Simulated S_{11} vs frequency of the antenna for different positions of L-slot with $\epsilon_r = 4.4$, h = 1.6 mm, L = 32 mm, W = 31.6 mm, D = 30 mm, $L_g = 15$ mm, $W_g = 14$ mm, $R_L = 1$ mm, $R_W = 0.5$ mm, $W_f = 3$ mm, g = 0.3 mm, s = 0.3 mm, $LS_1 = 1.5$ mm, $LS_2 = 11.5$ mm, $LS_t = 0.3$ mm, $US_1 = 7$ mm, $US_2 = 2.4$ mm, $US_t = 0.3$ mm, $US_s = 0.5$ mm and $U_p = 4$ mm

172

As the distance L_p of the slot from the edge of the ground plane increases, the rejection capability at WiMAX band is lost. This is seen in the case of $L_p = 2.5$ mm and is because for this position, the top portion of the ground plane gets separated by the slot. For $L_p = 1.5$ mm, optimum results are obtained as seen in the figure.

A.2.2 Optimization of U-slot Parameters

A second notched band is realized by embedding a U-shaped slot in the coplanar waveguide (CPW) feed line. Since the two types of slots are implemented on different elements of the antenna, the notched bands can be controlled independently.

Effect of length of U-slot, $US_1 + US_2 + US_1$

Keeping the overall length of the slot at a fixed length corresponding to WLAN frequency, the segment lengths are varied and results are shown in Fig. A.4.
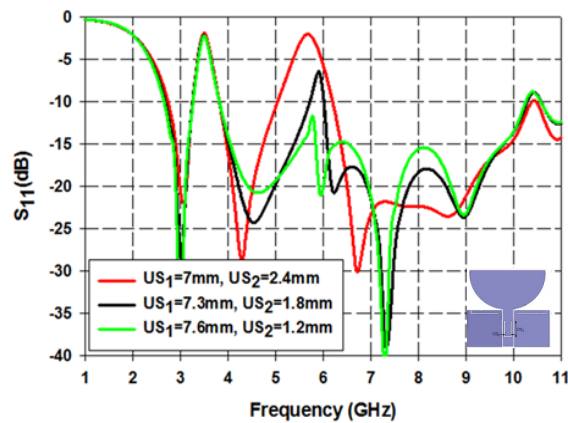
Fig. A.4   Simulated S_{11} vs frequency of the antenna for different lengths of U-slot segments with $\epsilon_r = 4.4$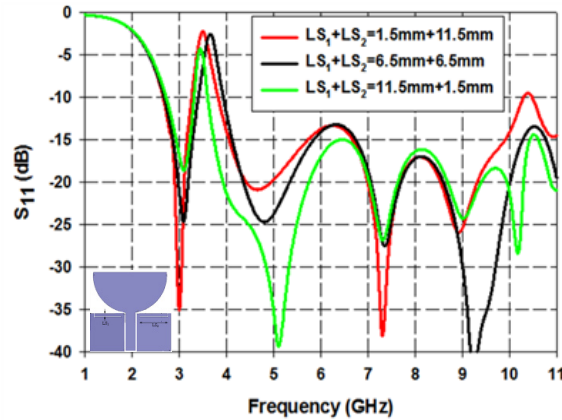, h = 1.6 mm, L = 32 mm, W = 31.6 mm, D = 30 mm, $L_g = 15$ mm, $W_g = 14$ mm, $R_L = 1$ mm, $R_W = 0.5$ mm, $W_f = 3$ mm, g = 0.3 mm, s = 0.3 mm, $LS_1 = 1.5$ mm, $LS_2 = 11.5$ mm, $LS_t = 0.3$ mm, $L_p = 2$ mm, $US_t = 0.3$ mm, $US_s = 0.5$ mm and $U_p = 4.5$ mm

173

The U-shaped slot inserted in the CPW feed line has two vertical segments each of length US_1 and one horizontal segment of length US_2. The overall length of this slot is approximately a half wavelength of the notched frequency.

$$US_1 + US_2 + US_1 \approx \lambda_g/2 \qquad\qquad (A.2)$$

As US_2 is increased, the bandwidth of the notched band increases and impedance matching decreases. Due to the limited space, available in the CPW-feed line, the horizontal segment length US_2 cannot be increased beyond 2.4 mm. For $US_1 = 7$ mm and $US_2 = 2.4$ mm, high rejection is obtained throughout the WLAN band. For all combinations of segment lengths, the first notched band remains unaffected.

Effect of position of U-slot, U_p

By varying the position of the U-slot the bandwidth can be controlled as shown in Fig. A.5.

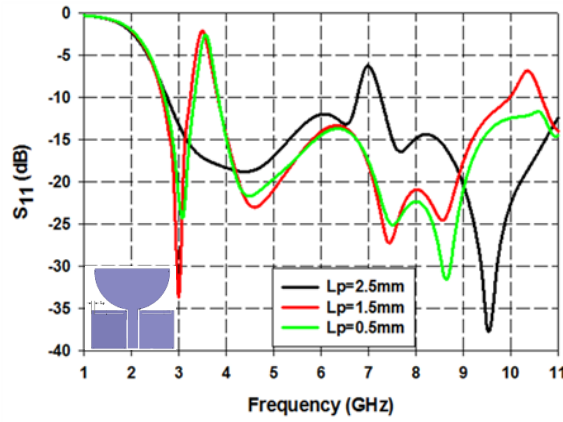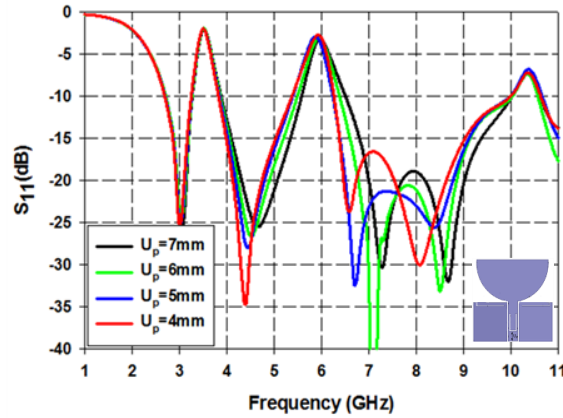Fig. A.5   Simulated S_{11} vs frequency of the antenna for different positions of U-slot with $\epsilon_r = 4.4$, h = 1.6 mm, L = 32 mm, W = 31.6 mm, D = 30 mm, $L_g = 15$ mm, $W_g = 14$ mm, $R_L = 1$ mm, $R_W = 0.5$ mm, $W_f = 3$ mm, g = 0.3 mm, s = 0.3 mm, $LS_1 = 1.5$ mm, $LS_2 = 11.5$ mm, $LS_t = 0.3$ mm, $L_p = 2$ mm, $US_1 = 7$ mm, $US_2 = 2.4$ mm, $US_t = 0.3$ mm and $US_s = 0.5$ mm

174

While it is necessary that the antenna has very poor impedance matching in the intended rejection band, the bandwidth of the notched band is also an important parameter that needs to be controlled. As position of the U-slot is lowered, the notched band shifts to the lower frequency side. At Up = 4 mm, the intended WLAN band is properly notched out and so this dimension is chosen as the optimum value.

A.3 SURFACE CURRENT DISTRIBUTION

The antenna with optimized dimensions is simulated in HFSS™ and surface current distributions at the notched frequencies are shown in Fig. A.6.

At the notch frequency corresponding to WiMAX band, the current is mainly concentrated around the L-shaped slots while at WLAN frequency the current distribution on the U-shaped slot is very high.
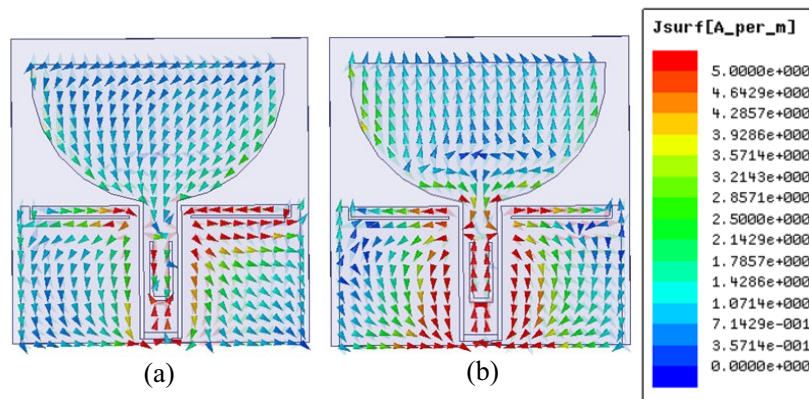
Fig. A.6   Surface current distribution of the antenna at notched frequencies (a) 3.5 GHz (b) 5.7 GHz with ϵ_r = 4.4, h = 1.6 mm, L = 32 mm, W = 31.6 mm, D = 30 mm, L_g = 15 mm, W_g = 14 mm, R_L = 1 mm, R_W = 0.5 mm, W_f = 3 mm, g = 0.3 mm, s = 0.3 mm, LS_1 = 1.5 mm, LS_2 = 11.5 mm, LS_t = 0.3 mm, L_p = 1.5 mm, US_1 = 7 mm, US_2 = 2.4 mm, US_t = 0.3 mm, US_s = 0.5 mm and U_p = 4 mm

At both the notched frequencies, the currents on the corresponding slots flow in opposing directions which leads to the band rejection.

A.4 REFLECTION CHARACTERISTICS

The antenna prototype is printed on a substrate with relative permittivity 4.4, loss tangent 0.02 and thickness 1.6 mm and tested using Agilent PNA E8362B. Simulated and measured reflection characteristics are compared in Fig. A.7.

The peak rejected level is -1.69 dB in the first notch band corresponding to WiMAX and -2.37 dB in the second notched band for WLAN. Measured results are found to be in good agreement with simulated results in the second notch band. The bandwidth of the first notch band is however slightly higher than simulated results.
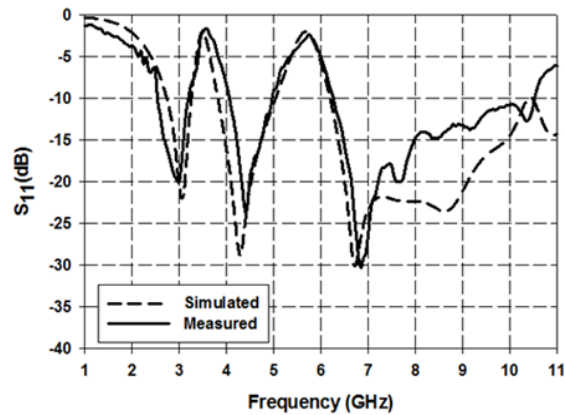
Fig. A.7 Simulated and measured reflection characteristics of the antenna with ϵ_r = 4.4, h = 1.6 mm, L = 32 mm, W = 31.6 mm, D = 30 mm, L_g = 15 mm, W_g = 14 mm, R_L = 1 mm, R_W = 0.5 mm, W_f = 3 mm, g = 0.3 mm, s = 0.3 mm, LS_1 = 1.5 mm, LS_2 = 11.5 mm, LS_t = 0.3 mm, L_p = 1.5 mm, US_1 = 7 mm, US_2 = 2.4 mm, US_t = 0.3 mm, US_s = 0.5 mm and U_p = 4 mm

There is a mismatch in readings at higher frequencies but this can be attributed to soldering effects that have not been accounted for in simulation studies.

A.5 RADIATION PATTERN

The simulated 3D radiation patterns are shown in Fig. A.8.
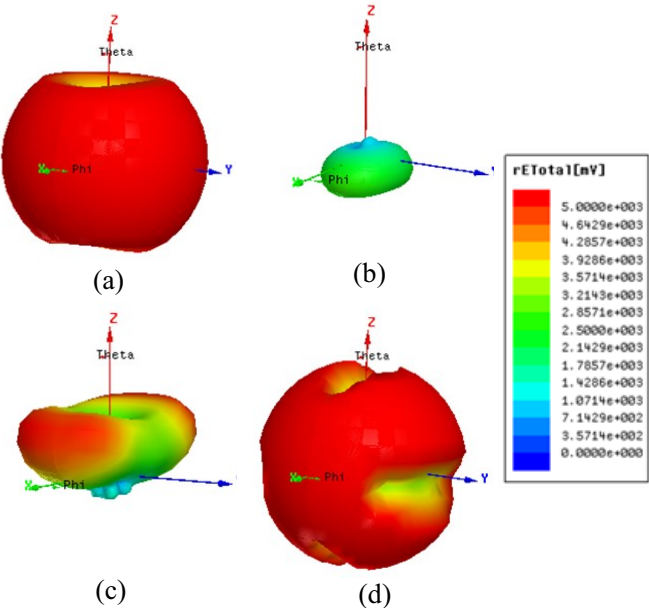
Fig. A.8   Simulated 3D radiation patterns of the antenna at (a) 3.1 GHz (b) 3.5 GHz (c) 5.7 GHz (d) 6.8 GHz with ϵ_r = 4.4, h = 1.6 mm, L = 32 mm, W = 31.6 mm, D = 30 mm, L_g = 15 mm, W_g = 14 mm, R_L = 1 mm, R_W = 0.5 mm, W_f = 3 mm, g = 0.3 mm, s = 0.3 mm, LS_1 = 1.5 mm, LS_2 = 11.5 mm, LS_t = 0.3 mm, L_p = 1.5 mm, US_1 = 7 mm, US_2 = 2.4 mm, US_t = 0.3 mm, US_s = 0.5 mm and U_p = 4 mm

The patterns are shown at two radiated frequencies in the UWB operating range as well as at two notched frequencies. At the notched frequencies of 3.5 GHz and 5.7 GHz, the

radiation patterns show a significant decrease in strength of the radiated field compared to strength at other frequencies.

The normalized measured radiation patterns of the antenna at various radiated frequencies are plotted in two principle planes and shown in Fig. A.9.

Fig. A.9   Normalized measured radiation patterns of the antenna at (a) 3.1 GHz (b) 6.8 GHz (c) 10 GHz with $\epsilon_r = 4.4$, h = 1.6 mm, L = 32 mm, W = 31.6 mm, D = 30 mm, L_g = 15 mm, W_g = 14 mm, R_L = 1 mm, R_W = 0.5 mm, W_f = 3 mm, g = 0.3 mm, s = 0.3 mm, LS_1 = 1.5 mm, LS_2 = 11.5 mm, LS_t = 0.3 mm, L_p = 1.5 mm, US_1 = 7 mm, US_2 = 2.4 mm, US_t = 0.3 mm, US_s = 0.5 mm and U_p = 4 mm

Measurements in each principle plane are taken for two orthogonal orientations of the horn antenna to obtain co-polarization and cross-polarization readings. Throughout the operating range, the antenna has non-directional pattern in the H (X-Y) plane.

A.6 PEAK GAIN

The measured peak gain of the antenna is shown in Fig. A.10.
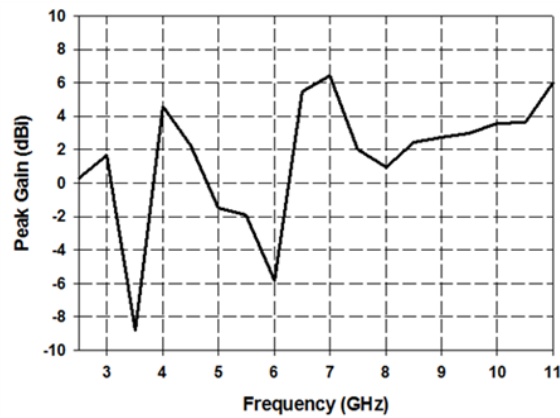
Fig. A.10   Measured peak gain of the antenna with $\epsilon_r = 4.4$, h = 1.6 mm, L = 32 mm, W = 31.6 mm, D = 30 mm, $L_g = 15$ mm, $W_g = 14$ mm, $R_L = 1$ mm, $R_W = 0.5$ mm, $W_f = 3$ mm, g = 0.3 mm, s = 0.3 mm, $LS_1 = 1.5$ mm, $LS_2 = 11.5$ mm, LS_t = 0.3 mm, $L_p = 1.5$ mm, $US_1 = 7$ mm, $US_2 = 2.4$ mm, US_t = 0.3 mm, $US_s = 0.5$ mm and $U_p = 4$ mm

Gain is low in the notch bands and decreases sharply at 3.5 GHz and 6 GHz. In the rest of the UWB range gain is positive with a peak gain of 6.44 dBi at 7 GHz.

A.7 CONCLUSION

A compact CPW-fed UWB antenna with dual notched characteristic is presented. Slots are inserted in the ground plane and feed line to notch out the frequency bands

corresponding to WiMAX and WLAN applications which can cause possible interference to UWB applications. The design allows independent control of the two notch bands with strong rejection. Since the radiating patch is left undisturbed, omni-directional radiation pattern is obtained throughout the UWB range.

APPENDIX-B

FREQUENCY AND TIME DOMAIN CHARACTERIZATION OF CPW-FED DUAL BAND SPIRAL ANTENNA WITH UWB APPLICATION

The complete characterization of the CPW-fed spiral multiband antenna (Type-II) presented in Chapter 5 on Rogers RT/Duroid 5880 substrate is presented here.

B.1 ANTENNA GEOMETRY

The geometry of the proposed antenna is shown in Fig. B. 1. The substrate used is of relative permittivity ϵ_r = 2.2 and thickness h = 0.79 mm. The spiral consists of two complete turns of metal strips of width W_s with uniform spacing g_s between the turns.
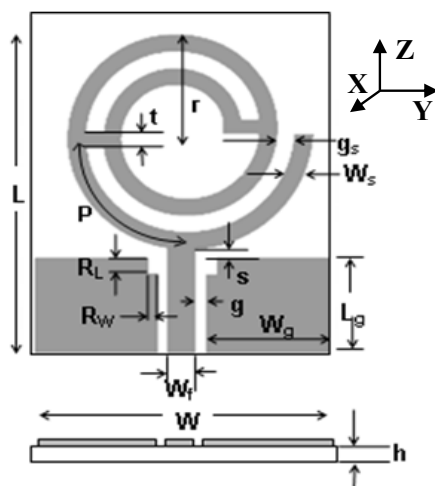
Fig. B.1   Geometry of the antenna with optimized dimensions W = 38.6 mm, L = 38 mm, L_g = 12.3 mm, W_g = 15.4 mm, R_L = 2.6 mm, R_W = 1 mm, W_f = 6.9 mm, g = 0.48 mm, s = 0.48 mm, g_s = 1.83 mm, W_s = 2.44 mm, r = 13 mm, P = 92.36 mm and t = 2.44 mm

The 50 Ω CPW-feed line has a width, W_f and is spaced at a distance, g from the ground plane of length, L_g and width, W_g on both sides. The monopole is spaced at a distance *s* from the ground plane and the overall size of the antenna is 38.6×38 mm^2. A small section of the ground plane of size $R_W \times R_L$ is cut away near the feed line to improve matching at higher frequencies. The spiral is asymmetrically oriented with respect to the feed line such that its outermost turn with radius r mimics the outer edge of a simple circular monopole (Liang, 2005a) and this results in UWB operation. The spiral monopole with two shorting strips between its turns results in a lower band suitable for WMTS application. One strip is placed at a distance, P along the length of the spiral monopole from feed line and it has a width, t. The position of this shorting strip determines the resonance frequency of the lower band. By placing a second shorting strip of same width at the inner end of the spiral, improved impedance matching is obtained in the UWB band without disturbing the first resonance. The design equations and parametric analysis are presented and validated in Chapter 5.

B.2 FREQUENCY DOMAIN CHARACTERISTICS

B.2.1 Reflection Characteristics

A prototype of the antenna is fabricated on Rogers RT/Duroid 5880 substrate and tested using Agilent PNA E8362B. Measured reflection characteristics are compared with simulation results and shown in Fig. 5.2.7 (b).

Simulated and measured values are in good agreement. There is a mismatch in readings at higher frequencies but this can be attributed to soldering effects that have not been accounted for in simulation studies. The antenna operating frequency ranges are 1.35-1.52 GHz and 3.1-11 GHz for $S_{11} \leq$ -10 dB.

B.2.2 Radiation Pattern

The normalized measured radiation patterns of the antenna at various radiated frequencies are plotted in two principle planes and shown in Fig. B. 2.
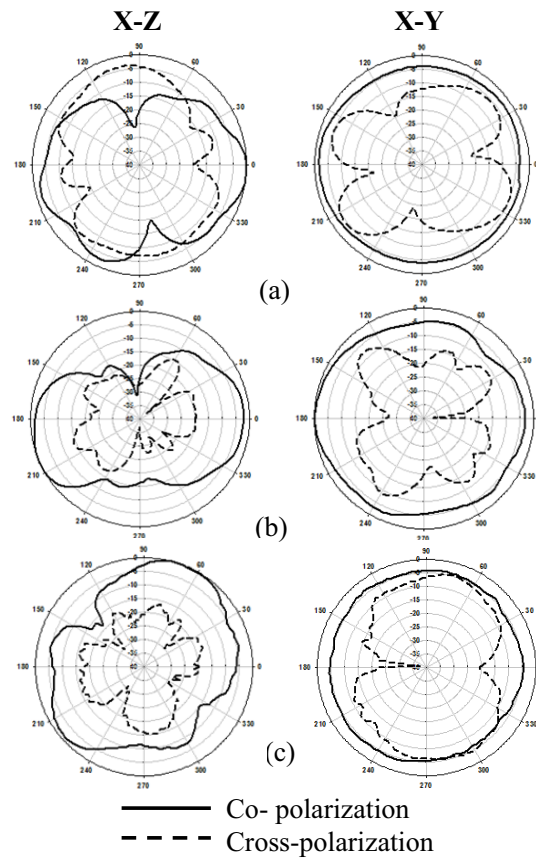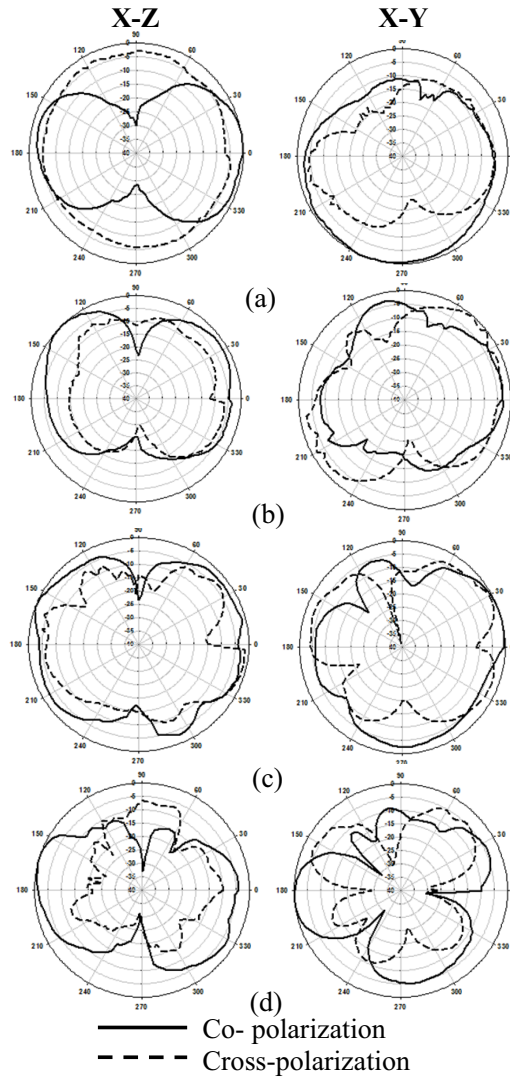

Fig. B.2   Normalized measured radiation patterns of the antenna at (a) 1.4 GHz (b) 4 GHz (c) 7 GHz (d) 10 GHz with $\epsilon_r = 2.2$, h = 0.79 mm, W = 38.6 mm, L = 38 mm, L_g = 12.3 mm, W_g = 15.4 mm, R_L = 2.6 mm, R_W = 1 mm, W_f = 6.9 mm, g = 0.48 mm, s = 0.48 mm, g_s = 1.83 mm, W_s = 2.44 mm, r = 13 mm, P = 92.36 mm and t = 2.44 mm

Measurements in each principle plane are taken for two orthogonal orientations of the horn antenna to obtain co-polarization and cross-polarization readings. At first resonance and lower frequencies of the UWB band, a doughnut pattern is observed in the X-Z plane and almost non-directional pattern in the X-Y plane. At upper end of the UWB band, the pattern is slightly distorted due to the excitation of higher order modes in the monopole. But the antenna exhibits nearly non-directional characteristics in the X-Y plane throughout the operating range.

B.2.3 Peak Gain

The peak gain measured using two-antenna method (Balanis, 2007) is shown in Fig. B. 3.
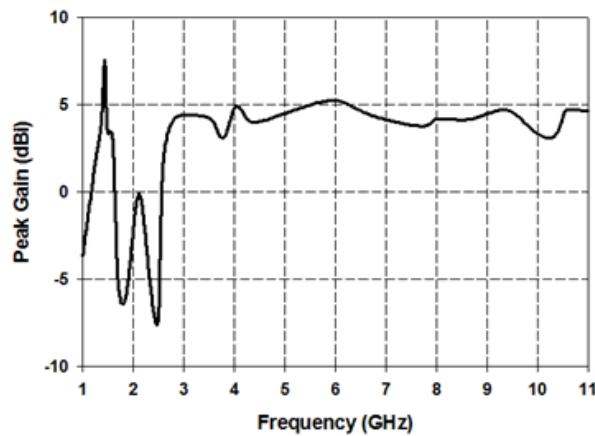
Fig. B.3   Measured peak gain of the antenna with $\epsilon_r = 2.2$, $h = 0.79$ mm, $W = 38.6$ mm, $L = 38$ mm, $L_g = 12.3$ mm, $W_g = 15.4$ mm, $R_L = 2.6$ mm, $R_W = 1$ mm, $W_f = 6.9$ mm, $g = 0.48$ mm, $s = 0.48$ mm, $g_s = 1.83$ mm, $W_s = 2.44$ mm, $r = 13$ mm, $P = 92.36$ mm and $t = 2.44$ mm

The antenna has a peak gain of 7.5 dBi at 1.4 GHz. Within the UWB range, gain is steady with a peak value of 5.2 dBi.

184

B.3 TIME DOMAIN CHARACTERISTICS

B.3.1 Group Delay

To evaluate the group delay, two antennas with identical radiation characteristics are placed 15 cm apart in three different orientations: face to face, face to side and side to side and measured results are shown in Fig. B. 4.
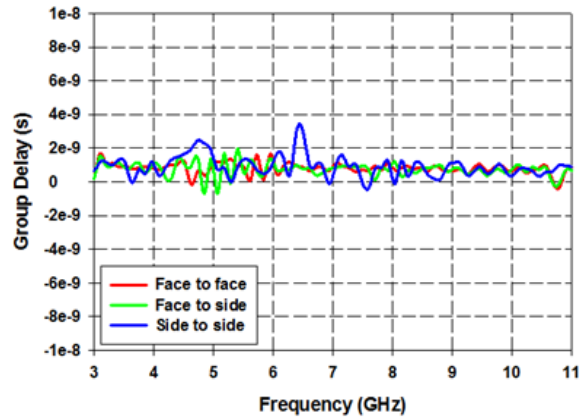
Fig. B.4   Measured group delay of the antenna for different orientations with $\epsilon_r = 2.2$, h = 0.79 mm, W = 38.6 mm, L = 38 mm, L_g = 12.3 mm, W_g = 15.4 mm, R_L = 2.6 mm, R_W = 1 mm, W_f = 6.9 mm, g = 0.48 mm, s = 0.48 mm, g_s = 1.83 mm, W_s = 2.44 mm, r = 13 mm, P = 92.36 mm and t = 2.44 mm

Group delay variation for face to face and face to side orientations is within an acceptable limit of 1 ns. In side to side orientation the group delay variation occasionally exceeds 2 ns.

B.3.2 FWHM and Ringing

Frequency domain measurements are done by modeling the antennas as a linear time invariant (LTI) system. Measurement is performed for different spatial orientations of

the two antennas in azimuth plane. The impulse response of the antenna is obtained by taking the inverse Fourier transform of the transfer function.

The envelope of the impulse response localizes the distribution of energy versus time and hence is a direct measure for the dispersion of an antenna. Measured values of FWHM and ringing of the proposed antenna for different azimuth angles are quite low as shown in Table.1.

Table B.1 Computed FWHM and ringing of antenna impulse response for different azimuth angles

Azimuth Angle	FWHM (ps)	Ringing (ps)
$\Phi=0^{\circ}$	202	274
$\Phi=45^{\circ}$	190	267
$\Phi=90^{\circ}$	166	115
$\Phi=135^{\circ}$	220	474

B.3.3 Fidelity Factor

For a UWB system, the received pulse is required to match the input pulse with minimum distortions because the pulse carries useful information. To examine the time-domain characteristic of the antenna, the incident pulse spectrum is multiplied by the normalized antenna transfer function. Then an inverse Fourier transform is performed to obtain time domain response of the output waveform at the receiving antenna terminal. The normalized received pulses for three different orientations are shown in Fig. B. 5.
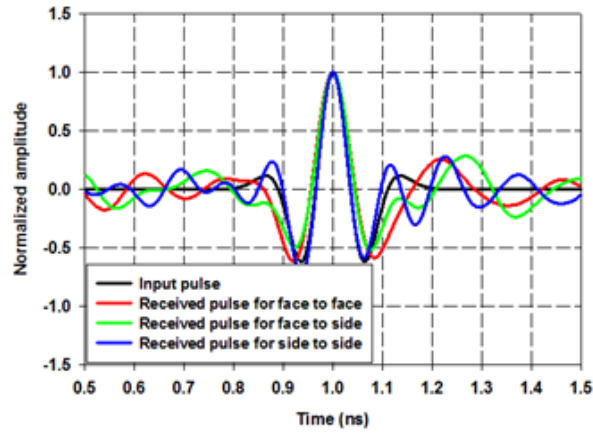
Fig. B.5   Comparison of input and received pulses of the antenna for
different orientations

The degree of correlation between the input and received pulses is evaluated using the

fidelity factor and is shown in Fig. B. 6.

Fidelity factor values are consistently above 0.9 which shows very good matching

between input and received pulses.
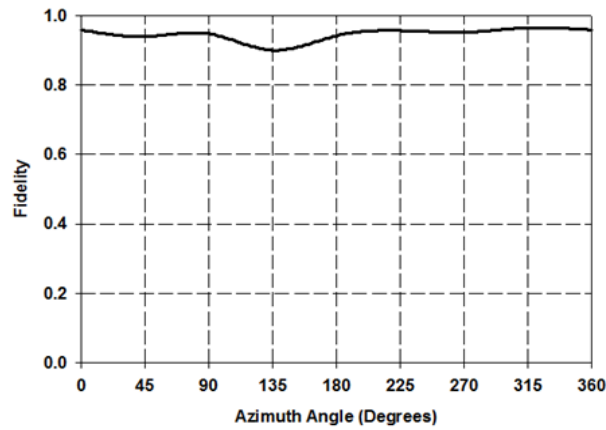
Fig. B.6   Fidelity factor of the antenna in azimuth plane

B.3.4 Radiated Power Spectral Density

According to FCC regulations, UWB systems must comply with stringent emission limits in the frequency band of operation. Radiated power spectral density of the antenna is plotted in Fig. B. 7.
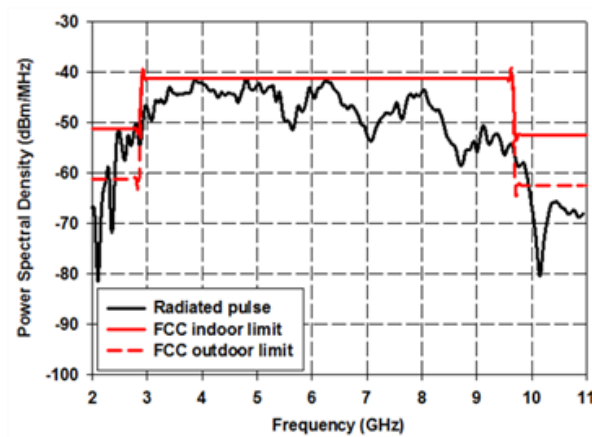
Fig. B.7   Power spectral density of the radiated pulse for the antenna
against the FCC emission mask

Within the frequency range from 3.1 to 10.6 GHz the radiated power of the proposed antenna is compliant with both the indoor and outdoor limits imposed by the FCC which confirms their suitability for UWB applications.

B.4 CONCLUSION

A compact CPW-fed spiral antenna for dual-band applications is presented. The antenna is designed on Rogers RT/Duroid 5880 substrate as per equations given in Chapter 5. The operating bands are suitable for WMTS and UWB applications. Good impedance matching and stable gain across the operating bands make the antenna a good candidate for wireless communication devices. To check the suitability of the

antenna for pulsed communication in UWB systems, time domain characterization is also performed. Measured results show that the antenna has low pulse distortion with a fidelity factor consistently above 0.9 in the azimuth plane. The antenna radiated power spectral density is also within the limits specified by FCC.

REFERENCES

1. **Agrawall, N. P., G. Kumar, and K. P. Ray** (1998) Wide band planar monopole antennas. *IEEE Transactions on Antennas and Propagation*, **46**, 292-295.

2. **Angelopoulos, E. S., A. Z. Anastopoulos, D. I Kaklamani, A. A. Alexandridis, F. Lazarakis, and K. Dangakis** (2006) Circular and elliptical CPW-fed slot and microstrip-fed antennas for ultrawideband applications, IEEE *Antennas and Wireless Propagation Letters*, **5**, 294-297.

3. **Awad, N. M. and M. K. Abdelazeez** (2013) Bluetooth/UWB circular patch antenna with dual band notches. *2013 IEEE Conference on Applied Electrical Engineering and Computing Technologies (AEECT)*, Jordan, 1-4.

4. **Azim, R., M. T. Islam, and N. Misran** (2010) Compact planar antenna for UWB applications. *World Academy of Science, Engineering and Technology*, **67**, 917-920.

5. **Aziz, R. S., M. A. S. Alkanhal, and A. F. A. Sheta** (2011) Multiband fractal-like antennas. *Progress in Electromagnetic Research B*, **29**, 339-354.

6. **Baek, S. and Y. Jee** (2011) Compact integrated monopole antenna with CPW-fed meander resonator. *Electronics Letters*, **47**(2), 79-80.

7. **Balanis, C. A**. *Handbook of Microstrip Antennas*. John Wiley and Sons New York, 1982.

8. **Balanis, C. A.** *Antenna Theory: Analysis and Design*, 2nd Edition, Wiley India Pvt. Ltd., 2007

9. **Bataller, M. F., M. C. Fabrés, E. A. Daviu, and A. V. Nogueira** (2006) Overview of planar monopole antennas for UWB application. Proceedings of *European Conference on Antennas and Propagation (EuCAP 2006)*, France, November.

10. **Bazaz, R., S. K. Koul, M. Kumar, and A. Basu** (2011) An ultrawideband antenna with band reject capability and its characterization in time domain. *Progress in Electromagnetics Research C*, **19**, 223-234.

11. **Bindu, C. J.** *Design and development of compact planar filters for ultrawideband applications*. Thesis, 2015.

12. **Bod, M., H. R. Hassani, and M. M. Samadi Taheri** (2012) Compact UWB printed slot antenna with extra Bluetooth, GSM, and GPS Bands. *IEEE Antennas and Wireless Propagation Letters*, **11**, 531-534.

13. **Chen**, **S.-W., D.-Y. Wang, and W.-H. Tu** (2014) Dual-band/tri-band/broadband CPW-fed stepped-impedance slot dipole antennas. *IEEE Transactions on Antennas and Propagation*, **62**(1), 485-490.

14. **Chen**, **T.-K. and G. H. Huff** (2011) Stripline-fed Archimedean spiral antenna. *IEEE Antennas and Wireless Propagation Letters*, **10**, 346-349.

15. **Chen**, **X. and S. Kiaei** (2002) Monocycles shapes for ultrawideband system. *IEEE Conference on Ultra Wideband Systems and Technologies*, **48**(6), 597–600.

16. **Chen, Z. N. and K. -M. Luk** *Antennas for Base Stations in Wireless Communications.* McGraw-Hill Professional, AccessEngineering, 2009.

17. **Chen, Z. N., T. S. P. See, and X. Qing** (2007) Small printed ultrawideband antenna with reduced ground plane effect. *IEEE Transactions on Antennas and Propagation*, **55**(2), 383-388.

18. **Chiang, M.-J., S. Wang, and C.-C. Hsu** (2012) Compact multi-frequency slot antenna design incorporating embedded arc-strip. IEEE Antennas and Wireless Propagation Letters, 11, 834-837.

19. **Chiu**, **C.-N. and W.-H. Chuang** (2009) A novel dual-band spiral antenna for a satellite and terrestrial communication system. *IEEE Antennas and Wireless Propagation Letters*, **8,** 624-626.

20. **Choi**, **S. H., J. K. Park, S. K. Kim, and J. Y. Park** (2004) A new ultrawideband antenna for UWB applications. *Microwave and Optical Technology Letters*, **40**(5), 399-401.

21. **Choi**, **S., K. Hamaguchi and R. Kohno (2009)** Small printed CPW-fed triangular monopole antenna for ultrawideband applications. *Microwave and Optical Technology Letters*, **51**(5), 1180-1182.

22. **Dahalan**, **F. D., S. K. A. Rahim, M. R. Hamid, M. A. Rahman, M. Z. M. Nor, M. S. A. Rani, and P. S. Hall** (2013) Frequency-reconfigurable Archimedean spiral antenna. *IEEE Antennas and Wireless Propagation Letters*, **12**, 1504-1507.

23. **Darvish**, **M. and H. R. Hassani** (2012) Multiband uniplanar monopole antenna for MIMO applications. *20th Iranian Conference on Electrical Engineering, (ICEE)*, Iran, May, 1125-1128.

24. **Deng**, **C., L. Li, Q. Gong, D. Zhan, and Y. Zou** (2011) Planar printed monopole antennas for ultrawideband/multi-band wireless systems. *IEEE 4th International Symposium on Microwave, Antenna, Propagation and EMC Technologies for Wireless Communications (MAPE)*, Beijing, November, 1-4.

25. **Ding**, **Y., Y. C. Jiao, P. Fei, B. Li, and Q. T. Zhang** (2011) Design of a multiband quasi-Yagi-type antenna with CPW-to-CPS Transition. *IEEE Antennas and Wireless Propagation Letters*, **10,** 1120-1123.

26. **Dong**, **D., S. Chen, Z. Liao, and G. Liu** (2014) A CPW-fed dual-band-notched antenna with sharp skirt selectivity for UWB applications. *International Journal of Antennas and Propagation*, **2014**.

27. **Eldek**, **A. A., A. Z. Elsherbeni, and C. E. Smith** (2005) Rectangular slot antenna with patch stub for ultrawideband applications and phased array systems. *Progress in Electromagnetics Research*, PIER 53, 227–237.

28. **Elmansouri**, **M. A. and D. S. Filipovic** (2011) Pulse distortion and mitigation thereof in spiral antenna-based UWB communication systems. *IEEE Transactions on Antennas and Propagation*, **59**(10), 3863-3871.

29. **Elsheakh, D. M. and E. A. Abdallah** (2012) Compact multiband multifolded-slot antenna loaded with printed-IFA. *IEEE Antennas and Wireless Propagation Letters*, **11**, 1478-1481.

30. FCC online table of frequency allocations (2012), *Federal communications commission office of engineering and technology policy and rules division*.

31. **Foudazi**, **A., H. R. Hassani, and S. M. Ali Nezhad** (2012) Small UWB planar monopole antenna with added GPS/GSM/WLAN bands. *IEEE Transactions on Antennas and Propagation*, **60**(6), 2987-2992.

32. **Gao**, **W., R. Venkatesan, and C. Li** (2007) A pulse shape design method for ultrawideband communications. *Wireless Communications and Networking Conference*, **6**(7), 2800-2805.

33. **Garg**, **R., P. Bhartia, I. Bahl, and A. Ittipiboon** *Microstrip Antenna Design Handbook*, Norwood, MA Artech House, 2001.

34. **Gautam, A., S. Yadav, and B. Kananjia,** (2013) A CPW-fed compact UWB microstrip antenna. *IEEE Antennas and Wireless Propagation Letters*, **12**, 151-154.

35. **Ghassemi**, **N., K. Wu, S. Claude, X. Zhang, and J. Bornemann** (2011) Compact coplanar waveguide spiral antenna with circular polarization for wideband applications. *IEEE Antennas and Wireless Propagation Letters*, **10**, 666-669.

36. **Gianvittorio**, **J. P. and Y. Rahmat-Samii** (2002) Fractal antennas: A novel antenna miniaturization technique and applications. *IEEE Antenna's and Propagation Magazine*, **44**(1), 20-36.

37. **Gong**, **L., K. Y. Chan, and R. Ramer** (2013) A Reconfigurable spiral Antenna with wide beam coverage. *IEEE Antennas and Propagation Society International Symposium (APSURSI)*, July.

38. **Gorai, A., A. Karmakar, M. Pal, and R. Ghatak** (2013) A CPW-fed propeller shaped monopole antenna with super wideband characteristics. *Progress In Electromagnetics Research C*, **45**, 125–135.

39. **HFSS user's manual** (2005) version 10, Ansoft Corporation.

40. **Hongnara, T., C. Mahattanajatuphat, P. Akkaraekthalin, and M. Krairisksh,** (2012) A multiband CPW-fed slot antenna with fractal stub and parasitic line. *Radioengineering,* **21**(2), 597-605.

41. **Huang**, **H. and Z. Lv** (2014) A new spiral antenna with improved axial ratio and shorted arm length. *Progress in Electromagnetics Research C*, **46**, 83-89.

42. **Ifeachor**, **E. C. and B.W. Jervis**, *Digital Signal Processing, A practical Approach*, Addison-Wesley, 1993.

43. **Jacob**, **S., S. Mridula, V. A. Shemeena, and P. Mohanan** (2010) Planar UWB antenna. Proceedings of *Antenna and Propagation Symposium (APSYM)*, Cochin, December.

44. **Jahromi, M. N., A. Falahati, and R. M. Edwards** (2011) Bandwidth and impedance-matching enhancement of fractal monopole antennas using compact grounded coplanar waveguide. *IEEE Transactions on Antennas and Propagation*, **59**(7), 2480-2487.

45. **Jegadeesan, S. and Z. Mansouri** (2015) Ultrawideband PIFA antenna with supporting GSM and WiMAX for mobile phone applications. Proceedings of 5th *International Conference on Advanced Computing & Communication Technologies*, 15-20.

46. **Karimabadi**, **S. S. and A. R. Attari** (2010) Miniaturized ultrawideband elliptical monopole antenna with wireless local area network band rejection characteristic. *Electromagnetics*, **30**(4), 347 -355.

47. **Kaur**, **A., N. Saluja, and J. S. Ubhi** (2012) Design of Sierpinski gasket multiband fractal antenna for wireless applications. *IOSR Journal of Electronics and Communication Engineering (IOSRJECE)*, **2**(3), 5-6.

48. **Kelly**, **J. R., P. S. Hall, and P. Gardner** (2011) Band-notched UWB antenna incorporating a microstrip open-loop resonator. *IEEE Transactions on Antennas and Propagation*, **59**(8), 3045-3048.

49. **Kim**, **J. I. and Y. Jee** (2007) Design of ultrawideband coplanar waveguide-fed LI-shape planar monopole antennas. *IEEE Antennas and Wireless Propagation Letters*, **6**, 383-387.

50. **Kim, J. -M. and J. -G. Yook** (2005) Miniaturized CPW-fed variable width meander slot antenna. *Microwave and Optical Technology Letters*, **46**(2), 188-191.

51. **Koohestani**, **M., N. Pires, A. K. Skrivervik, and A. A. Moreira** (2013) Time-domain performance of a patch-loaded band-reject UWB antenna. *Electronic Letters*, **49**(6), 384-385.

52. **Kumar**, **M., A. Basu, and S. K. Koul** (2011) UWB printed slot antenna with improved performance in time and frequency domains. *Progress In Electromagnetics Research C*, **18**, 197–210.

53. **Kumar**, **R., D. Magar, and K. K. Sawant** (2012) On the design of inscribed triangle circular fractal antenna for UWB applications. *International Journal of Electronics and Communication (AEÜ),* **66**, 68-75.

54. **Kumar, S., D. Gangwar, and R. L. Yadava** (2014) Miniaturized inverted multiband stacked triangular fractal patch antenna for wireless communication. Proceedings of *International Conference on Signal Processing and Integrated Networks (SPIN)*, 667-670.

55. **Kushwaha, N. and R. Kumar** (2013) An UWB fractal antenna with defected ground structure and swastika shape electromagnetic band gap. *Progress In Electromagnetics Research B*, **52**, 383-403.

56. **Lam, H.-J. and J. Bornemann** (2007) Ultrawideband printed-circuit antenna in coplanar technology. *IEEE International Symposium on Electromagnetic Compatibility*, 1-4.

57. **Lee**, **C.-H., Y.-H. Chang, and C.-E. Chiou** (2012) Design of multi-band CPW-fed antenna for triple-frequency operation. *Electronics Letters*, **48**(10), 543-545.

58. **Lee, G.-S., S. Baek, K. Lee, and Y. Jee** (2011) Multi-band CPW-fed antennas with metamaterial structures. *The 6th International Conference on Telecommunication Systems, Service and Applications*, 73-76.

59. **Li**, **C. M. and L. H. Ye** (2011) Improved dual band-notched UWB slot antenna with controllable notched bandwidths *Progress in Electromagnetics Research*, **115**, 477-493.

60. **Li**, **X., L. Yan, W. Pan, and B. Luo** (2013) A compact printed quadruple band-notched UWB antenna. *International Journal of Antennas and Propagation*, Article ID 956898.

61. **Liang**, **J.** *Antenna Study and Design for Ultra Wideband Communication Applications*. Thesis, 2006.

62. **Liang**, **J., C. C. Chiau, X. Chen, and C. G. Parini** (2005a) Study of a printed circular disc monopole antenna for UWB systems. *IEEE Transactions on Antennas and Propagation,* **53**(11), 3500-3504.

63. **Liang, J., L. Guo, C. C. Chiau, and X. Chen** (2005b) CPW-fed circular disc monopole for UWB applications, Antenna Technology: Small Antennas and Novel Metamaterials. *IWAT 2005*, 505-508.

64. **Liao, W.-J., S.-H. Chang, and L.-K. Li** (2010) A compact planar multiband antenna for integrated mobile devices. *Progress in Electromagnetics Research*, **109**, 1-16.

65. **Lim, K.-S., M. Nagalingam, and C.-P. Tan** (2008) Design and construction of microstrip UWB antenna with time domain analysis. *Progress in Electromagnetics Research M*, **3**, 153-164.

66. **Lin, C. C. and H. R. Chuang** (2008) A 3–12 GHz UWB planar triangular monopole antenna with ridged ground-plane. *Progress in Electromagnetics Research*, PIER 83, 307–321.

67. **Lin, C. C., Y. C. Kan, L. C. Kuo and H. R Chuang** (2005) A planar triangular monopole antenna for UWB Communication. *IEEE Microwave and Wireless Components Letters*, **15**(10), 624-626.

68. **Lin, C.-C. and R. W. Ziolkowski** (2010) Tri-band notched ultrawideband antenna using capacitively loaded loops (CLLs). *IEEE Antennas and Propagation Society International Symposium,* Toronto, July*, 1-4.

69. **Liu, L., Y. Z. Yin, C. Jie, J. P. Xiong, and Z. Cu** (2008) A compact printed antenna using slot-type CSRR for 5.2 GHz/5.8 GHz band-notched UWB application. *Microwave and Optical Technology Letters*, **50**(12), 3239-3242.

70. **Liu, W.-C., C.-M. Wu and N.-C Chu** (2010) A compact CPW-fed slotted patch antenna for dual-band operation. *IEEE Antennas and Wireless Propagation Letters*, **9**, 110-113.

71. **Liu, Y.-F., P. Wang, and H. Qin** (2014) Compact ACS-fed UWB monopole antenna with extra Bluetooth band. *Electronics Letters*, 50(18), 1263–1264.

72. **Mandelbrot,** *The Fractal Geometry of Nature*, W. H. Freeman, New York, 1983.

73. **Mansouri, Z., A. S. Arezomand, S. Heydari, and F. B. Zarrabi** (2016) Dual notch UWB fork monopole antenna with CRLH metamaterial load. *Progress in Electromagnetics Research*, 65, 111-119.

74. **Mao, S.–G. and S.-L. Chen** (2007) Frequency- and time-domain characterizations of ultrawideband tapered loop antennas. *IEEE Transactions on Antennas and Propagation*, **55**(12), 3698-3701.

75. **Mashaal, O. A., S. K. A. Rahim, A. Y. Abdulrahman, M. I. Sabran M. S. A. Rani, and P. S Hall** (2013) A coplanar fed two-arm Archimedean spiral slot antenna with improved bandwidth. IEEE Transactions on Antennas and Propagation, **61**(2), 939-943.

76. **McDonald, K. T.** (2003) Small fractal antennas. *Journal for Science and Engineering*, Princeton University, Princeton.

77. **Milanovic**, **V., M. Gaitan, E. D. Bowen, and M. E. Zaghloul** (1997) Micromachined microwave transmission lines in CMOS technology. *IEEE Transactions on Microwave Theory Techniques*, **45**(5), 630-635.

78. **Mirkamali, A., L.-Asl Akhoondzadeh, P. S. Hall, and K. Moussakhani** (2010) Modified multiband multiple ring monopole antenna. *Progress in Electromagnetic Research C*, **14**, 173 – 183.

79. **Mishra, S. K., R. Gupta, A. Vaidya and J. Mukherjee** (2011) Printed fork shaped dual-band monopole antenna for Bluetooth and UWB applications with 5.5 GHz WLAN band notched characteristics. *Progress in Electromagnetics Research C*, **22**, 195-210.

80. **Mobashsher, A. T., M. T. Islam, and N. Misran** (2011) RFID technology: Perspectives and technical considerations of microstrip antennas for multi-band RFID reader operation, current trends and challenges in RFID, InTech.

81. **Nakano**, **H., R. Satake, and J. Yamauchi** (2010) Extremely low-profile, single-arm, wideband spiral antenna radiating a circularly polarized wave. IEEE *Transactions on Antennas and Propagation*, **58**(5), 1511-1520.

82. **Naser, S. and N. Dib** (2016) Spanner-shaped ultrawideband monopole antenna with Bluetooth and GSM coverage. *Jordan Journal of Electrical Engineering*, **2**(2), 94-106.

83. **Natarajamani**, **S., S. K. Behera, and S. K. Patra** (2011) Planar UWB fractal antenna with band-notched characteristics. *International Conference on Electronic Systems (ICES-2011)*, Rourkela, January.

84. **Nazlı, H., E. Bıçak, B. Türetken, and M. Sezgin**, (2010) An improved design of planar elliptical dipole antenna for UWB applications. *IEEE Antennas and Wireless Propagation Letters*, **9**, 264-267.

85. **Norman, H. B. and C. Beaulieu** (2005) Pulse shapes for ultrawideband communication systems. *IEEE Transactions on Antennas and Propagation*, **6**(7), 1789-1797.

86. **Nur**, **T. E., S. K. Ray, D. Paul, and T. Mollick** (2011) Design of fractal antenna for ultrawideband applications. *International Journal of Research and Reviews in Wireless, Communications (IJRRWC),* **1**(3).

87. **Oraizi**, **H. and S. Hedayati** (2014) Microstrip slot antenna using the novel application of Giuseppe Peano fractal and CPW feed. *The 8th European Conference on Antennas and Propagation (EuCAP 2014)*, 2063-2066.

88. **Pell**, **B., E. Sulic, W. Rowe, K. Ghorbani, S. John, R. Gupta, and Kefei** (2008) The design and realization of uniplanar CPW fed PICA slot antennas. *IEEE Asia Pacific Microwave Conference,* December, 1-4.

89. **Powell, J. and A. Chandrakasan** (2004) Differential and single ended elliptical antennas for 3.1-10.6 GHz ultrawideband communication. In Proceedings of *IEEE Antennas and Propagation Society International Symposium*, **3**, 2935-2938.

90. **Porcino, D.** (2003) Ultra-wideband radio technology: potential and challenges ahead. *IEEE Communications Magazine,* 2-11.

91. **Pozar, D. M.** *Microwave engineering*, 3rd Edition, Wiley India Pvt. Ltd., 2011.

92. **Puente, C., J. Romeu, R. Pous, and A. Cardama** (1998) On the behavior of the Sierpinski multiband fractal antenna. *IEEE Transactions on Antennas and Propagation*, **46**(4), 517-524.

93. **Rambabu**, **K., H. Thiart, J. Bornemann, and S. Yu** (2006) Ultrawide band printed circuit antenna. *IEEE Transactions on Antennas and Propagation*, **54**(12), 3908-3911.

94. **Ray**, **K. P.** (2008) Design aspects of printed monopole antennas for ultrawide band applications. *International Journal of Antennas and Propagation*, **2008**.

95. **Reddy, G. S., A. Chittora, S. Kharche, S. Mishra, and J. Mukherjee** (2013) Bluetooth/UWB dual-band planar diversity antenna with WiMAX and WLAN band-notch characteristics. *Progress in Electromagnetics Research B*, **54**, 303–319.

96. **Remenyi, D., G. Onofrei, and J. English** (2011) An introduction to statistics using Microsoft excel. *Academic Conferences Limited.*

97. **Saidatul**, **N. A., A. A. H. Azremi, R. B. Ahmad, P. J. Soh, and F. Malek** (2009) Multiband fractal planar inverted f antenna (F-PIFA) for mobile phone application. *Progress in Electromagnetics Research B*, **14**, 127-148.

98. **Sayidmarie**, **K. H. and T. A. Najm** (2013) Performance evaluation of band-notch techniques for printed dual-band monopole antennas. *Journal of Electromagnetics and Applications*, **3**(4), 70-80.

99. **Schantz**, **H. G.** (2002) Radiation efficiency of UWB antennas. Proceedings of the *2002 IEEE UWBST Conference*, USA, May, 351-355.

100. **Schantz, H. G.** (2003) A brief history of UWB antennas. Proceedings of *The IEEE UWBST Conference*.

101. **Seong**, **C. M. and D. C. Park** (2012) Design of cavity-backed spiral antennas. *Global Symposium on Millimeter Waves (GSMM)*, China, May, 186-190.

102. **Shahu B. L., N. Chattoraj, and S. Pal** (2013) A novel CPW fed Sierpinski carpet fractal UWB slot antenna. *IEEE International Conference on Microwave and Photonics (ICMAP2013)*, Dhanbad, December, 1-4.

103. **Shaker, A., S. H. Zainud-Deen, K. R. Mahmoud, and S. M. Ibrahem** (2011) Compact Bluetooth/UWB antenna with multi-band notched characteristics. *Journal of Electromagnetic Analysis and Applications*, **3**, 512-518.

104. **Shameena, V. A.** *Design and development of compact printed ultra wideband antennas*, Thesis, 2012.

105. **Shameena, V. A., S. Mridula, S. Jacob, C. K. Aanandan, K. Vasudevan, and P. Mohanan** (2011) A compact modified ground CPW fed antenna for UWB applications. *Microwave review*, 13-19.

106. **Shih, T.-Y. and N. Behdad** (2014) Miniaturization of a circularly-polarized, uni-directional, ultrawideband spiral antenna. *IEEE Antennas and Propagation Society International Symposium (APSURSI)*, Memphis, July, 285-286.

107. **Si, L.-M. and X. Lv** (2008) CPW-fed multi-band omni-directional planar microstrip antenna using composite Metamaterial resonators for wireless communications. *Progress in Electromagnetics Research*, PIER **83**, 133-146.

108. **Soni, Y. K., N. K. Agrawal, and S. Joshi,** (2013) Design and analysis of compact printed coplanar waveguide-fed integrated Bluetooth and UWB antenna. *Annual IEEE India Conference (INDICON)*, 1-4.

109. **Sorgel, W., S. Knorzer, and W. Wiesbeck** (2003) Measurement and evaluation of ultrawideband antennas for communications. *International ITG Conference on Antennas – INICA2003*, **19**(24), 377-380.

110. **Sujith, R., V. Deepu, S. Mridula, B. Paul, D. Laila, and P. Mohanan** (2011) Compact CPW-fed uniplanar antenna for multiband wireless applications. *International Journal of Electronics and Communications*, **65**, 553-559.

111. **Tan, A. E.-C., M. Y.-W. Chia, K. K.-M. Chan, and K. Rambabu** (2013) Modeling the transient radiated and received pulses of ultrawideband antennas. *IEEE Transactions on Antennas and Propagation,* **61**(1), 338-345.

112. **Tanyer-Tigrek F. M., A. Hizar, I. E. Lager and L. P. Ligthart** (2010) On the operating principles of UWB CPW-fed printed antennas. *IEEE Antennas and Propagation Magazine*, **52**(3), 46-50.

113. **Taylor, J. D.** *Introduction to ultrawideband radar systems*, CRC Press, 1995.

114. **Touhami, N. A., Y. Yahyaoui, A. Zakriti, K. Bargach, M. Boussouis, M. Lamsalli, and A. Tribek** (2014) A compact CPW-fed planar pentagon antenna for UWB applications. *Progress in Electromagnetics Research C*, **46**, 153-161.

115. **Trang**, **N. D., D. H. Lee, and H. C.Park** (2011) Small planar coplanar waveguide-fed dual band-notched monopole ultrawideband antenna. *Microwave and Optical Technology Letters*, **53**(4), 920-924.

116. **Valleau**, **J., H. Aubert, O. Ripoche, and A Bellion** (2014) Pre-fractal resonant rings for compact spiral antennas. *16th International Symposium on Antenna Technology and Applied Electromagnetics (ANTEM)*, July, 1-2.

117. **Vyas**, **K., A. K. Sharma, and P. K. Singhal** (2014) Design and analysis of two novel CPW-fed dual band-notched UWB antennas with modified ground structures. *Progress in Electromagnetics Research*, **49**, 159-170.

118. **Wan**, **Y.-T., D. Yu, F.-S. Zhang, and F. Zhang** (2013) Miniature multi-band monopole antenna using spiral ring resonators for radiation pattern characteristics improvement. *Electronics Letters*, **49**(6), 382-384.

119. **Wang, J. and L. Yang** (2014) A compact four bands microstrip patch antenna with coplanar waveguide feed. Proceedings of *IEEE Asia Pacific Conference on Antennas and Propagation (APCAP)*, 33-36.

120. **Wang, L.-N., L. Shu, C. Run-nan, H. Guan-long and Z. Wen-bin** (2011) Multiband printed monopole antenna with square nested fractal. *6th International ICST Conference on Communications and Networking in China (CHINACOM)*, 929-932.

121. **Wang, Y. –W, G. –M. Wang and Z. –W Yu** (2010) Design of a highly miniaturized compound spiral antenna. *Proceedings of International Symposium on Signals, Systems and Electronics (ISSSE)*,

122. **Weisbeck**, **W., G. Adamiuk and C. Sturm** (2009) Basic properties and design principles of UWB antennas. Proceedings of the *IEEE*, **97**(2), 372-385.

123. **Weller**, **T. M., L. P. B. Katehi, and G. M. Rebeiz** (1995) High performance microshield line components. *IEEE Transactions on Microwave Theory Techniques*, **43**(3), 534-543.

124. **William**, **J. and R. Nakkeeran** (2010) A compact CPW-fed UWB slot antenna with cross tuning stub. *Progress in Electromagnetics Research C*, **13**, 159-170.

125. **Wu**, **A. and B. Guan** (2013) A compact CPW-fed UWB antenna with dual band notched characteristics. *International Journal of Antennas and Propagation*, **2013**, Article ID 594378.

126. **Xiong**, **L. and P. Gao** (2012) Dual-band planar for Bluetooth and UWB monopole antenna applications with WiMAX and WLAN band-notched. *Progress in Electromagnetics Research Letters*, **28**, 183–194.

127. **Yang**, **G. M., R. H. Jin, G. B. Xiao, C. Vittoria, V. G. Harris, and N. X. Sun** (2009) Ultrawideband (UWB) antennas with multiresonant split-ring loops. *IEEE Transactions on Antennas and Propagation*, **57**(1), 256-260.

128. **Yildirim, B. S., B. A. Cetiner, G. Roqueta, and L. Jofre** (2009) Integrated Bluetooth and UWB antenna. *IEEE Antennas and Wireless Propagation Letters*, **8,** 149-152.

129. **Yu**, **F. and C. Wang** (2009) A CPW-fed novel planar ultrawideband antenna with a band notch characteristic. *Radioengineering*, **18**(4), 551-555.

130. **Zhang F.-S., Y.-T. Wan, D. Yu, and B. Ye** (2013) A microstrip-fed multiband spiral ring monopole antenna with improved radiation characteristics at higher resonant frequencies. *Progress in Electromagnetics Research C*, **41**, 97-109.

131. **Zhang S.-M., F.-S. Zhang, W.-M. Li, W.-Z. Li, and H.-Y. Wu** (2012a) A multi-band monopole antenna with two different slots for WLAN and WiMAX applications. *Progress in Electromagnetics Research Letters*, **28**, 173–181.

132. **Zhang**, **H., H.-Y. Xu, B. Tian, and X.-F. Zeng** (2012b) CPW-fed fractal slot antenna for UWB application. *International Journal of Antennas and Propagation*, **2012**.

133. **Zhang**, **Q., Y. Li, Z. Liang, H.-Z. Tan, and Y. Long** (2014) A multiband monopole antenna with the inverted-trapezoidal CPW feeding. *International Journal of Antennas and Propagation*, **2014**, Article ID 692465.

134. **Zhang**, **X., T.-L. Zhang, Y.-Y. Xia, Z.-H. Yan, and X.-M. Wang** (2009) Planar monopole antenna with band-notch characterization for UWB applications. *Progress in Electromagnetics Research Letters*, **6**, 149–156.

135. **Zhong, S.-S., X. Yan, and X. Liang,** (2008**)** UWB planar antenna technology. *Frontiers of Electrical and Electronic Engineering* China, **3**(2), 136-144.

LIST OF PUBLICATIONS

International Journals

1. **S Joseph, B Paul, S Mridula, P Mohanan** (2013) A novel planar fractal antenna with CPW-feed for multiband applications. *Radioengineering*, **22** (4), 1262-1266.

2. **S Joseph, B Paul, S Mridula, P Mohanan** (2015) CPW-fed UWB compact antenna for multiband applications. *Progress in Electromagnetic Research C*, **56**, 29-38.
   doi:10.2528. /PIERC14112401

3. **S Joseph, B Paul, S Mridula, P Mohanan** (2015) CPW-fed compact UWB spiral antenna for multiband applications. *International Journal for Ultra Wideband Communications and Systems*, **3**(2), 85-93.
   doi:10.1504/IJUWBCS.2015.077111

International Conferences

4. **Saira Joseph, Binu Paul, Mridula S and P Mohanan**. CPW-fed fractal antenna with improved UWB response. *IEEE Asia Pacific conference on Antennas and Propagation (APCAP)*, Bali, Jun, 2015.
   doi:10.1109/APCAP.2015.7374277

5. **Aravind S, Saira Joseph, S Mridula, B Paul and P Mohanan**. Compact dual-band antenna for GSM 1800/1900/UMTS/LTE/UWB. *International Conference on Information and Communication technologies (ICICT)*, Cochin**,** Dec, 2014.
   doi:10.1016/j.procs.2015.02.051

6. **Saira Joseph, Binu Paul, Mridula S and P Mohanan**. Compact CPW-fed UWB antenna with dual notch bands. *International symposium on Antennas and Propagation (APSYM)*, Cochin, Dec, 2014.

7. **Saira Joseph, Binu Paul, Mridula S and P Mohanan.** CPW-fed compact multiband antennas using circular monopole with hexagonal slot. *International Conference on Advances in Computing and Communication (ICACC 2015),* Cochin, Sept, 2015.
   doi:10.1109/ICACC.2015.87

CURRICULUM VITAE

EDUCATION

Doctoral degree

Registration date: 11/10/2010, Division of Electronics Engineering, School of Engineering, CUSAT, Cochin, Kerala

MTech degree in Electronics,

2004-2006, Department of Electronics, CUSAT, Cochin, Kerala

CGPA: 9.19 (GATE score: 93.6)

Recipient of the K G Nair Endowment medal on securing 1st rank in the M-Tech, 2006 University examinations

BTech degree in Electronics

1997-2001, College of Engineering, Chengannur, Kerala

Percentage: 78.6

Pre degree in Group 2 with optional mathematics

1995-1997, Sree Narayana Women's College, Kollam

Percentage: 81

EXPERIENCE

SCMS School of Engineering and Technology

Assistant Professor (Jan 2008 onwards)

SR Engineering College, Warangal, Andhra Pradesh

Assistant Professor (July 2006- March 2007)

College of Engineering, Perumon, Kerala

Lecturer (October 2002- March 2004)

PROFICIENCY IN COMPUTERS

Languages: MATLAB$^®$, C++

Operating Systems: Windows XP, Linux

Tools: Sigmaplot, Coreldraw, CCStudio, Pspice, HFSS$^{™}$, CST

PERSONAL DETAILS

Nationality: Indian

Religion: Christian

Date of Birth: 10/08/1979

Languages: English, Hindi, Malayalam

Place of residence: Angamaly, Ernakulam, Kerala

Email: saira_joseph@scmsgroup.org

Mobile: 9846519453